Development of Micro- and Nano- Scanning Electrochemical Microscopy Probes for Prospective Applications in Lithium Ion Batteries

Laurence Danis, B.Sc.

McGill University, Montreal

June 2016

A thesis submitted to McGill University in partial fulfillment of the requirements of the degree of Doctor of Philosophy

ACKNOWLEDGMENTS

I would like to use this occasion to express my gratitude to my supervisor Prof. Janine Mauzeroll. I am truly thankful for her guidance, encouragement, knowledge and devotion to her student's success. I am especially thankful to Janine for always goings so far out of her way to provide for her group a pleasant research atmosphere. In fact, I could simply not have wish for a better supervisor.

I would like to express my sincere appreciation to all the staff at Heka Elektronik in Germany and in Nova Scotia who welcomed and helped me during both my internships in the beginning of my Ph.D. I am also grateful to Prof. Schougaard and Dr. Hallalay for their advice and suggestions during the course of my project.

I am grateful to all present, past and honorary members of the Mauzeroll group for their support, help and friendship throughout the years. I am very appreciative of everyone in the upstairs office: Stephani Mazurkiewick, Isabelle Beaulieu, David Polcari, Dr. Daupin-Ducharme, Nicholas Payne and my lab brother Andrew Danis for all the good talks and laughs over the years. I am especially thankful to Samantha M. Gateman for her support and assistance on my project and for helping me to get back in shape by dragging me to the gym, and to Lisa for all the cookies that sent me to gym. I am also thankful to Drs. Snowden, Kuss, Kuss, Perry and Noyhouzer for their help and for all the fun we have been having working together. I also want to acknowledge all the guys from the Schougaard group at UQAM, which I consider like my second lab.

On a more personal note, I would like thank all my family and friends who supported me all the way through my Ph.D. I would like to thank both of my sisters Catherine and Carole-Anne, and my two nieces Zia and Calli for always being there to celebrate all the small victories and to cheer me up during the academic woes. I will forever be grateful for the support of my Mom and Dad who made all of this possible. I would like to express my gratitude towards the Danis foundation for the special Danis tuition fee waiver scholarship. To conclude, I would like to thank my best friend and life partner Dr. Ngoc Duc Trinh for being so supportive and understanding over the years.

ACKNOWLEDGMENTS BY CHAPTERS

Acknowledgments Chapter 1

This work was financially supported by General Motors and the Natural Sciences and Engineering Research Council of Canada (CRSNG). S.M. Gateman, Dr. Kuss, and Prof. Schougaard are acknowledged for their help and useful discussions.

Acknowledgments Chapter 2

This work was financially supported by the Natural Sciences and Engineering Research Council of Canada (CRSNG) and by le Fonds Québécois de la Recherche sur la Nature et les Technologies (FQRNT). We appreciate the help and contribution to this manuscript of D.Polcari, A.Kwan, and S.M.Gateman.

Acknowledgments Chapter 3

This work was supported by the Natural Sciences and Engineering Research Council of Canada (NSERC), The Fonds de recherche du Québec Nature et Technologie (FRQNT) and HEKA Elektronik through the Industrial Innovation Scholarships (IIS) BMP Innovation FRQNT - NSERC. Dr. M.E. Snowden, Dr. U.M. Tefashe and Dr. C.N. Heinemann are acknowledged for their help and advice on the shear force experiments.

Acknowledgments Chapter 4

This work was financially supported by General Motors and the Natural Sciences and Engineering Research Council of Canada (CRSNG). S.M. Gateman, Dr. M.E. Snowden, Dr. I.C. Halalay and Dr. J.Y. Howe are acknowledged for their help and useful discussions.

Acknowledgments Chapter 5

This work was financially supported by General Motors and the Natural Sciences and Engineering Research Council of Canada (CRSNG). S.M. Gateman, is acknowledged for performing some of the experimental data and the conceptualisation of some experiments.

Table of Contents

LIST OF FIGURES

LIST OF TABLES

LIST OF ABBREVIATIONS AND NOMENCLATURES

AFM	Atomic Force Microscopy
AFM-SECM	Atomic Force Microscopy - Scanning Electrochemical Microscopy
Ag/AgCl	Silver-Silver Chloride reference electrode (saturated KCl, +0.222V *vs*. NHE)
AgQRE	Silver Quasi-Reference Electrode
ALD	Atomic Layer Deposition
ASV	Anodic Stripping Voltammetry
c-AFM	Conductive AFM
CD-R	Rewritable Compact Disk
CTFE	Chlorotrifluoroethylene
CV	Cyclic Voltammogram
DMC	Dimethyl Carbonate
EC	Ethylene Carbonate
EC-STM	Electrochemical Scanning Tunneling Microscopy
EDS	Energy Dispersive X-ray Spectroscopy
EDX	Energy Dispersive X-ray Spectroscopy
EFM	Electrostatic Force Microscopy
ELP	ElProScan
ESC	ElProScan Controller
ESEM	Environmental Scanning Electron Microscopy
ESM	Electrochemical Strain Microscopy
FB	Feedback Mode
Fc/Fc$^+$	Ferrocene / Ferrocenium
FcMeOH	Ferrocenemethanol or FcCH$_2$OH
FEM	Finite Element Method
Fig	Figure
HAR	Hemisphere area ratio
Hg/Hg$_2$SO$_4$	Mercury-Mercurous Sulfate reference electrode (saturated K$_2$SO$_4$, +0.654V *vs.* NHE)
HOPG	Highly Oriented Pyrolytic Graphite
IC	Intermittent-Contact Mode
ICP-AES	Inductively Coupled Plasma Atomic Emission Spectroscopy
KPM	Kelvin Probe Microscopy
Li/Li$^+$	Lithium-Lithium$^+$ reference electrode (-3.045 V *vs*. NHE)
LIBs	Lithium Ion Batteries
2MeF	2-methylfuran
2MeTHF	2-methyltetrahydrofuran
2MeTp	2-methylthiophene
NHE	Normal hydrogen electrode
OCV	Open Circuit Voltage
PC	Propylene Carbonate
PVDF	Polyvinylidene Fluoride
QRE	Quasi-Reference Electrode
REF	Reference Electrode

RMS	Root Mean Square
RTILs	Room Temperature Ionic Liquids
Ruhex	Ruthenium hexamine
SCE	Standard calomel electrode (saturated KCl, +0.241V *vs.* NHE)
SSD	Solid State Detector
SECCM	Scanning Electrochemical Cell Microscopy
SECM	Scanning Electrochemical Microscopy
SEI	Solid Electrolyte Interphase
S.E.M.	Standard Error of the Mean
SEM	Scanning Electron Microscopy
SF	Shear Force
SF-SECM	Shear Force Scanning Electrochemical Microscopy
SFU	Shear Force Unit
SI	Supplementary Information
SICM	Scanning Ion-Conductance Microscopy
SPM	Scanning Probe Microscopy
SPT	Scanning Probe Techniques
SSRM	Scanning Spreading Resistance Microscopy
STM	Scanning Tunneling Microscopy
SVET	Scanning Vibrating Electrode Technique
TFPC	Trifluoropropylene Carbonate
TPM	Tip-Position Modulation
UME	Ultramicroelectrode
VC	Vinylene Carbonate
VPSEM	Variable Pressure Scanning Electron Microscopy
VSM	Voltage switching mode
XANES	X-ray Absorption Near-Edge Spectroscopy
XPS	X-ray Photo Electron Spectroscopy
XRD	X-ray Diffraction

LIST OF SYMBOLS

A_1	Maximum response amplitude taking in account for experimental noise (V)
A_2	Minimum response amplitude taking in account for experimental noise (V)
A_H	Maximum response amplitude (V)
A_L	Minimum response amplitude (V)
A_S	Surface area of the spherical cap (cm^2)
A_SD	Amplitude standard deviation (V)
β	Microelectrode geometry factor, analytical expression considering the R_g
C^*	Concentration of the electroactive species in the bulk solution (mol cm^{-3})
d	Tip-to-substrate distances (μm)
D	Diffusion coefficient (cm s^{-2})
E^0	Standard reduction potential (V)
F	Faraday constant (96 485 C mol^{-1})
h	Height of the segment (cm)
I	Current (A)
I_{ss}	Steady state current (A)
k	Geometric constant
$\mathbf{l}$	Vector from the origin to the center of the spherical cap
n	Number of electrons involved in the electrochemical reaction
$\mathbf{n}$	Normal unit vector
$\mathbf{N}$	Flux vector
Q_F	Quality of the probe with respect to the signal to noise ratio
R_g	Ratio between the r_T and the radius of the Pt tip of the UME
r_T	Radius of the electroactive area (cm)
r_s	Spherical cap radius (cm)
θ	Phase shift (°)
Z_L	Absolute value where the tip is on the substrate surface (μm)
Z_S	SF sense length regime (μm)
Z_H	Tip-to-substrate separation (μm)

DEVELOPMENT OF MICRO- AND NANO- SCANNING ELECTROCHEMICAL MICROSCOPY PROBES FOR PROSPECTIVE APPLICATIONS IN LITHIUM ION BATTERIES

by Laurence Danis, B.Sc.

Doctor of Philosophy

Chemistry Department - McGill University

2016

ABSTRACT

Lithium ion batteries (LIBs) have become a common power source for most portable home electronic devices including cellular phones, computers, tablets, power tools, and, recently, electric vehicles. Despite their success, the commercial market demands portable energy storage which offers more charge/discharge cycles, shorter recharge times, and higher power densities. Therefore, LIB materials research aims to improve key electrochemical properties.

The cubic spinel lithium manganese oxide ($Li_xMn_2O_4$) is an alternative to $LiCoO_2$ and is one of the most investigated positive electrode materials for LIBs. $Li_xMn_2O_4$ is of particular interest due to its advantageous electrochemical performance at room temperature (i.e. high capacity and stable operating voltage), significant natural abundance, low cost, and low toxicity. Regardless of these advantages, $Li_xMn_2O_4$ experiences a fast capacity fade with charge/discharge cycling and poor storage performance, particularly at elevated temperatures. This hinders its widespread commercial use, especially for large-scale automotive applications. This capacity-fading phenomenon is believed to be due to numerous factors, such as the Jahn-Teller distortion, the decomposition of electrolyte solution on the negative electrode, and the dissolution of Mn^{2+} from the positive electrode into the electrolyte. Most research groups agree that dissolution of Mn^{2+} cations is the leading mechanisms for the decreased capacity and is primarily caused by the hydrogen fluoride (HF) contained in the electrolyte.

In-depth understanding of the mechanism of Mn dissolution could provide insights for new methods to inhibit the dissolution pathway. However, standard manganese detection techniques are performed *ex-situ*, post cell disassembly and have potential risk of data alterations due to air sensitivity of these materials, creating a need for *in-situ* analysis techniques of battery materials.

The presented dissertation investigates the use of scanning probe microscopy (SPM) analysis methods to provide localized information on the fundamental mechanisms, processes and degradation of LIBs. Herein, we present the step-by-step development of a high resolution scanning electrochemical microscopy (SECM) technique for the quantitative detection of Mn^{2+} cations.

More precisely, we describe the development and characterization of Hg/Pt hemispherical micro- and nano- SECM probes used with anodic stripping voltammetry (ASV), for the quantitative detection of Mn^{2+} cations.

We have successfully developed a simple, fast, and reproducible method for the fabrication of disk microelectrodes with controlled geometry. A second fabrication technique is presented for the production of well-defined Pt disk electrodes with the electroactive core in the nanometer scale. Both of these fabrication techniques produce electrodes that are are ideal backbones for the production of Hg-based hemispherical ASV sensors.

Also presented is a systematic study of the shear force (SF) characteristics of these nanoelectrodes and a new methodology to identify SF sensitive frequencies. SF is used in SECM to maintain a constant tip-to-substrate distance for the deconvolution of the kinetic and topographic information received in SECM.

The Hg/Pt hemispherical nanoelectrodes were used for the quantitative detection of manganese cations. The ASV technique has been used to evaluate the impact of using polymeric chelating macrocyles, such as crown ethers, as separator coatings. The coated separators would serve for the sequestration of Mn^{2+} cations, thus preventing their migration to negative electrodes, and therefore mitigating the undesirable consequences of manganese dissolution in LIBs. A transition from an aqueous environment to a more representative oxygen and water-free environment in propylene carbonate (PC) $LiClO_4$, a typical a non-aqueous electrolyte for LIBs, has also been performed.

ABRÉGÉ

Les batteries lithium-ion sont devenues une source d'énergie commune pour la plupart des appareils électroniques portables à la maison, comprenant les téléphones cellulaires, ordinateurs, tablettes, outils électriques et plus récemment, les véhicules électriques. Malgré leur succès, le marché exige des sources d’entreposage d'énergie portable qui offrent davantage de recharge/décharge, des temps de recharge réduits, et une haute densité énergétique. Par conséquent, la recherche sur les matériaux de batteries vise à améliorer les propriétés électrochimiques de celles-ci.

L'oxyde de manganèse lithié ($Li_xMn_2O_4$) est une alternative intéressante à la traditionnelle électrode positive $LiCoO_2$. Le $Li_xMn_2O_4$ est l’un des matériaux d'électrodes positives les plus étudiés, car il est d'un intérêt particulier en raison de ses performances électrochimiques avantageuses à température ambiante (à savoir une capacité élevée et un potentiel d’opération stable), de son abondance, de son coût modique, et de sa faible toxicité. Cependant, le $Li_xMn_2O_4$ subit une diminution de capacité substantielle pendant les cycles de décharge/recharge ainsi qu’au cours des périodes d’entreposage, particulièrement lorsque celles-ci sont effectuées à des températures élevées. Cela empêche son utilisation commerciale à grande échelle, en particulier dans le milieu automobile. La perte de capacité est liée à de nombreux facteurs tels que la distorsion Jahn-Teller, la décomposition de l’électrolyte sur l'électrode négative et la dissolution du Mn^{2+} à partir de l'électrode positive dans la solution électrolytique. De nombreux groupes de recherche conviennent que la dissolution du Mn^{2+}, provoquée par la présence d’acide fluorhydrique (HF) dans l’électrolyte, est le facteur principal conduisant à la diminution de capacité des batteries à base de $Li_xMn_2O_4$.

Une connaissance approfondie du mécanisme de dissolution du Mn pourrait fournir des indications afin de bloquer la voie de dissolution. Cependant, les techniques de détection de manganèse actuelles sont effectuées *ex situ* après avoir désassemblé la batterie. Par conséquent, ces méthodes présentent un risque potentiel d'altérations des résultats dues à la nature des matériaux étudiés et de leur sensibilité à l'air. Ceci crée ainsi un besoin pour le développement de techniques *in situ* et *in operando* pour caractériser les composants de batteries $Li_xMn_2O_4$.

La présente thèse porte sur l'utilisation de méthodes de microscopie à sonde locale (SPM) pour obtenir de l’information localisée sur les mécanismes fondamentaux et sur les processus de dégradation des batteries lithium-ion.

Dans cette thèse, nous présentons étape par étape le développement de méthodes électrochimiques et de microscopie électrochimique à balayage (SECM) pour la détection quantitative à haute résolution de Mn^{2+}. Plus précisément, nous décrivons le développement et la caractérisation de nanoélectrodes hémisphériques Hg/Pt utilisées en voltampérométrie inverse anodique (ASV) pour la détection quantitative des cations Mn^{2+}.

Nous avons développé une technique simple, rapide et reproductible pour la production d’ultramicroélectrodes (UMEs) disques avec un centre électroactif de taille micrométrique et une géométrie contrôlée. Une deuxième technique de fabrication est présentée pour la production d’ultramicroélectrodes disques avec un centre électroactif de taille nanométrique. Les deux tailles d’UMES forment des supports idéals pour la production d’électrode de mercure hémisphérique.

Une étude systématique de la force de cisaillement (SF) ainsi qu’une nouvelle méthode pour identifier les fréquences sensibles à la SF sont aussi présentées dans cette thèse. La SF est utilisée en SECM pour maintenir une distance constante entre l’électrode et le substrat pour la déconvolution des deux signaux reçus.

Des nanoélectrodes hémisphériques Hg/Pt ont été utilisées pour la détection quantificative de manganèse. La technique a été employée pour évaluer l'impact de l'utilisation de macrocyles chélateurs polymériques, tels que les éthers couronnes, lorsque déposés sur les séparateurs de batterie. En séquestrant les cations Mn^{2+}, leur migration vers l’électrode négative est écartée, atténuant ainsi les conséquences indésirables de la dissolution du manganèse dans les batteries Li-ion. Un transfert des mesures en milieux aqueux vers une mesure réalisée à l’intérieur d’une boîte à gants dans un électrolyte de LIBs non-aqueux (propylène carbonate (PC), $LiClO_4$) a aussi été effectué.

PREFACE & CONTRIBUTION OF AUTHORS

CONTRIBUTION TO ORIGINAL SCHOLARSHIP AND DISTINCT CONTRIBUTIONS TO KNOWLEDGE

CHAPTER 2. CONTRIBUTIONS TO ORIGINAL KNOWLEDGE

1. A new simple, fast, and reproducible method for the fabrication of carbon, gold, platinum, silver and mercury disk ultramicroelectrodes (UMEs) with controlled geometry was developed.

L. Danis, D. Polcari, A. Kwan, S.M. Gateman, J. Mauzeroll, Analytical Chemistry, 87 (2015) 2565-2569.

L. Danis, A.T. Noyhouzer, M.E. Snowden, U. M. Tefashe, J. Mauzeroll. 2016, International Patent Application No. PCT/CA2016/050314.

L. Danis, J. Mauzeroll. 2015, US patent application No. 62/200,156.

CHAPTER 3. CONTRIBUTIONS TO ORIGINAL KNOWLEDGE

2. A procedure for the fabrication of highly reproducible disc nanoelectrodes with an active electrode with radii between 3 nm to 190 nm was developed.

3. A systematic study of the shear force (SF) characteristics of these nanoelectrodes provided details on how to achieve the highest sensitivity and stability of SF signals, and maximize the number of SF sensitive frequencies. A new methodology to identify SF sensitive frequencies without needing to immerse the probes in solution or approach the surface was established.

L. Danis, M.E. Snowden, U.M. Tefashe, C.N. Heinemann, J. Mauzeroll, Electrochimica Acta, 136 (2014) 121-129.

CHAPTER 4. CONTRIBUTIONS TO ORIGINAL KNOWLEDGE

4. A fabrication technique of platinum-mercury hemispherical nanoelectrodes was developed. The fully characterized electrochemical probes were employed for the quantitative detection of Mn^{2+}. The technique has been used to evaluate the impact of a novel approach for mitigating the undesirable consequences of manganese dissolution in Lithium-ion batteries (LIB).

L. Danis, S.M. Gateman, M.E. Snowden, I. Halalay , J. Howe, J. Mauzeroll, Electrochimica Acta,162 (2015) 169-175.

CHAPTER 5. CONTRIBUTIONS TO ORIGINAL KNOWLEDGE

5. The methods involved in fabricating and characterizing mercury-capped nanoelectrodes to be employed in a glove box were developed. These characterized electrochemical UMEs were used as manganese amperometric probes for Mn^{2+} in battery electrolyte. This technique has been used to evaluate the ability of crown ethers to chelate Mn^{2+} cations for application in LIBs.

CONTRIBUTIONS OF ALL AUTHORS

All research, experimental work and writing reported in the thesis were performed under the supervision of Prof. Janine Mauzeroll of McGill University.

All research, experimental data analysis, significant technical procedures reported in this thesis were conceptualised and conducted by the lead investigator unless mentioned otherwise. The author was the major contributor to the preparation and submission of all published manuscripts and replied to questions from the reviewers.

CHAPTER 1. CONTRIBUTIONS OF ALL AUTHORS

The submitted manuscript presented in chapter 1 has been written in collaboration with S.M Gatemen (McGill University) who helped with the literature research and the writing of the positive electrode material section. Dr. Christian Kuss (University of Oxford) and Prof. Schougaard (Université du Québec à Montréal) helped with the preparation of the published manuscript. The frontispiece is a creation from the artist Maryse Maillette (Université du Québec à Montréal).

CHAPTER 2. CONTRIBUTIONS OF ALL AUTHORS

The published manuscript presented in Chapter 2 is a collaboration with another graduate student D. Polcari (McGill University) and two undergraduate students A. Kwan (McGill University) and S.M. Gateman. The author designed and developed the UME fabrication technique and collected all the electrochemical data. The two undergraduates students reproduced the procedure to build statistical data. S.M. Gateman also worked on the recessing of the Au UMEs to build the mercury disc UMEs. D. Polcari performed the data analysis and theoretical fit. The author and D.Polcari contributed equally to the preparation of the published manuscript, to the manuscript submission and replied to questions from the reviewers.

CHAPTER 3. CONTRIBUTIONS OF ALL AUTHORS

The author conducted all of the experimental work and collected all of the data, with the exception of the final shear force mapping presented in Figure 3.8., which was recorded in collaboration with Dr. U.M. Tefashe (McGill University). Dr. C.N. Heinemann (HEKA Elektronik) helped in the conceptualization of the experimental work. Dr. M.E. Snowden (McGill University) helped with the preparation of the published manuscript, the manuscript submission and the response to questions from the reviewers.

CHAPTER 4. CONTRIBUTIONS OF ALL AUTHORS

The author conducted all of the experimental work and collected all of the data. The simulated data of the hemisphere area ratio with respect to the normalised steady state current and simulated negative feedback approach curve were collected by Dr. M.E. Snowden (McGill University). The experiments presented in the Figure 4 of the published manuscript were part of a collabration with an undergraduate student S.M. Gateman (McGill University). The author designed the experiment and the undergraduate student conducted the experimental work under the supervision of the author. The eSEM image of the mercury hemisphere was collected by J.Y. Howe (Hitachi High-Technologies Canada Inc). The crown ethers were graciously donated by I.C. Halalay (The Chemical and Material Systems Laboratory, Global Research & Development, General Motors Company).

CHAPTER 5. CONTRIBUTIONS OF ALL AUTHORS

The manuscript presented in Chapter 5 is a collaboration with S.M. Gateman. The lead investigator designed and developed the procedure and collected all of the electrochemical data in collaboration with S.M. Gateman.

.

CHAPTER 1: INTRODUCTION - NANOSCALE MEASUREMENTS OF LITHIUM ION BATTERY MATERIALS USING SCANNING PROBE TECHNIQUES

The general purpose of this thesis is the investigation of SPM analysis methods as a means to gain localized information on the fundamental mechanisms, processes and degradation of LIBs at the nanoscale. More precisely, this thesis aims at developing analytical tools for the detection of manganese ions resulting from the dissolution of Mn^{2+} from $Li_xMn_2O_4$ positive electrodes. In-depth comprehension of the Mn dissolution mechanism would provide insights into novel approaches for inhibition of the dissolution or the migration pathway.

A technique was developed to detect manganese ions, which was then used to evaluate the use of polymeric chelating agents placed in the inter-electrode space of the LIB to reduce the migration of Mn^{2+} from the positive to the negative electrode. This was done by developing Hg-based nano-size manganese amperometric sensors to perform ASV for the quantitative detection of Mn^{2+} cations. This technique could be used in conjunction with SECM for the localized, quantitative detection of Mn^{2+} cations at the nano-scale, using the shear force enhancement strategies also developed in this thesis. The main goal has been divided into four smaller objectives, presented *vide infra*.

1. Development of micro- and nano- shear force scanning electrochemical microscopy probes

Chapters 2 and 3 describe the development of micro- and nano-size SECM UMEs with well controlled geometry. Pt UMEs are the backbone of the of the Hg-based manganese amperometric sensors. Controlling the geometry of the sensor is crucial as the geometry of the UME tip significantly affects the signal received in SECM. The work presented in Chapters 2 and 3 tackles the problem of reducing both the radius of the electroactive surface and the overall size of the UMEs in order to improve the resolution in SECM.

2. Enhancement and Characterization of the Shear Force Signal

The SF signal is used in SECM to maintain a constant tip-to-substrate distance. Maintaining a constant tip-to-substrate separation is a key solution to the deconvolution of the topographic data from the electrochemical measurement. Several factors influence the SF sensitivity, including the tip-to-substrate separation, experimental condition, and probe geometry. The probes presented in Chapters 2 and 3 are well suited for SF measurements. Chapter 3 provides a systematic study of the SF signal and gives insights into how to improve the sensitivity and stability of the SF signals.

3. Development of Hg-based ASV for the quantitative detection of Mn^{2+} cations and evaluation of the trapping efficiency of manganese chelating agents

Chapter 4 presents the development and calibration of Hg-based ASV using the probe developed in Chapter 2, on which an Hg hemisphere has been deposited for the quantitative determination of Mn^{2+}. Detecting Mn^{2+} is of particular interest for the LIBs community, as the dissolution of Mn^{2+} from manganese containing positive electrode such as $Li_xMn_2O_4$ is known to significantly reduce the retention of the capacity of these type of batteries. Several tactics have been proposed to alleviate the dissolution from the positive electrode and to mitigate the migration of the Mn^{2+} ions from the positive to the negative electrode. The migration of the Mn^{2+} is highly detrimental to the battery, as once at the negative electrode the manganese ions contribute to the formation of a passivation layer, which critically impacts the capacity loss. The ASV technique has been used to evaluate the possibility of using polymeric chelating crown ethers as separator coatings to trap Mn^{2+} and reduce its migration.

4. Development of Hg-based ASV for the quantitative detection of Mn^{2+} cations in a water and oxygen-free environment.

Due to the air-sensitive nature of LIB materials, the SPM community interested in the field started to implement their system in an argon filled glovebox. Chapter 5 describes the first steps to perform Hg-based ASV detection of Mn^{2+} in order to assess the efficiency of the crown ethers in a battery-like environment (*i.e.* O_2 and H_2O below 1 ppm, in battery electrolyte).

The main objective of Chapter 1 is to explore and contextualize the use of SPM methods to address the evolving need for characterization of nanostructured materials for energy conversion and storage devices. The rapid growth of SPM-based methods has allowed a more in-depth understanding of the fundamental properties of LIBs and insights into degradation and failure mechanisms.

Nano-active materials improve the performance of LIBs substantially. The decrease in dimension reduces the length scale lithium ions have to move within the active material; this is the bottle neck as the diffusion coefficient inside the active material is several orders of magnitude lower than within the electrolyte. Understanding the properties of these nano-materials necessitates new analytical characterization tools for studying nanoscale processes. SPM-approaches bring many more potential characterization opportunities in comparison to standard macroscopic electrochemical methods. SPM-based methods bring the ability to gain information about the surface with high resolution and the prospect for mapping nanoscale individual active grains or particles. This chapter investigates SPM based-techniques that have potential to further our understanding of LIB. Namely, in-situ scanning tunneling microscopy (STM), atomic force microscopy (AFM) including conductive AFM (c-AFM), Kelvin probe microscopy (KPM), electrochemical strain microscopy (ESM), electrostatic force microscopy (EFM), scanning spreading resistance microscopy (SSRM), SECM, scanning electrochemical cell microscopy (SECCM), scanning ion conductance microscopy (SICM), scanning vibrating electrode technique (SVET), and combined SPM-methods (e.g. AFM-SECM) are identified as analytical tools for their application in the field.

1. ABSTRACT

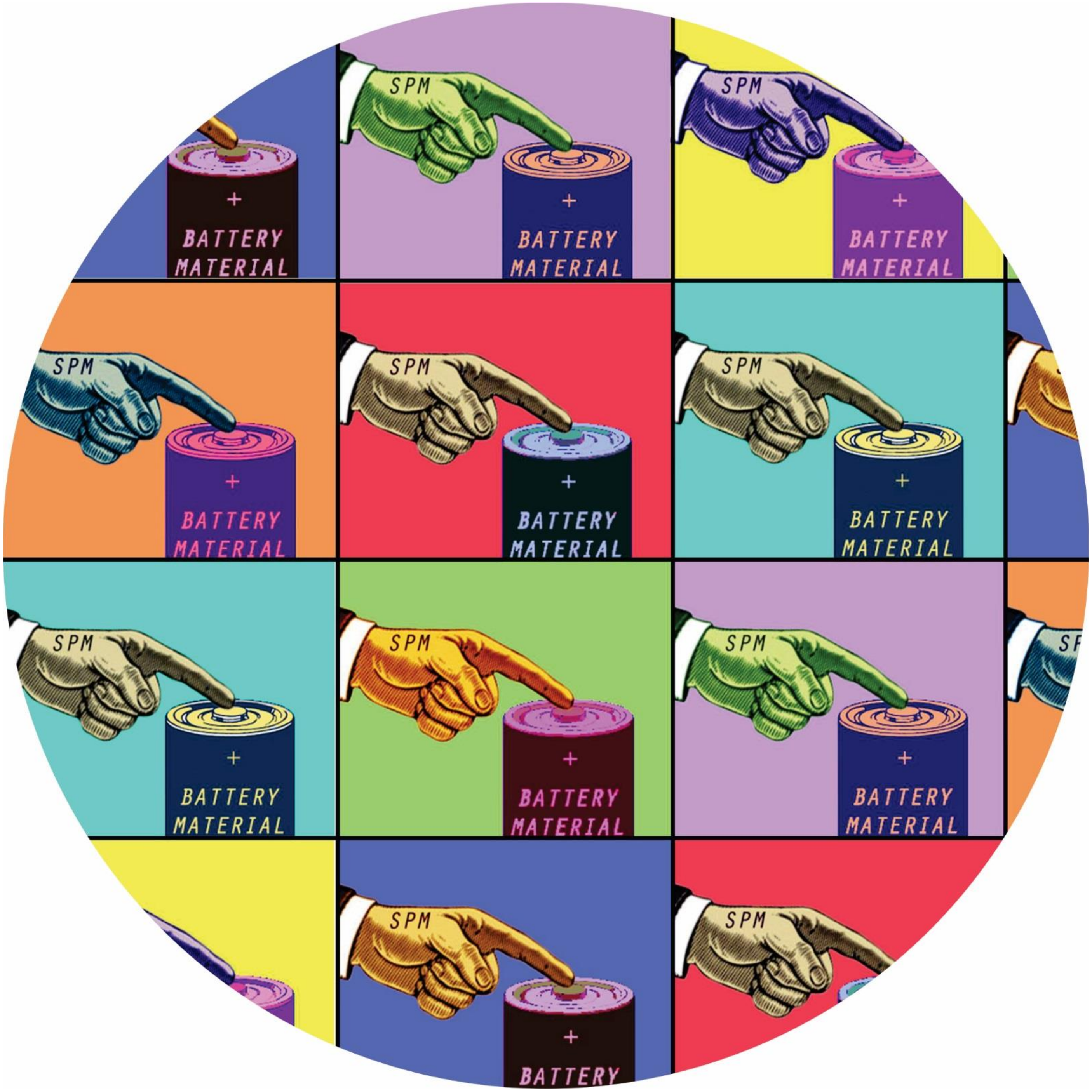

The state of the art of SPM methods applied to energy conversion and storage devices, specifically lithium ion batteries is reviewed with emphasis on the electroactive elements. The unique abilities of SPM-based methods to provide localized information has proven highly valuable for in-depth understanding of LIBs fundamental mechanisms, processes and degradation. As such, SPM analysis is poised to play a strong role in the competition for new higher performing LIB, especially given the unprecedented choice and availability of SPM techniques tailored to provide physical and chemical information at the nanoscale.

1.1. Introduction: Lithium Ion Battery

SONY Corporation's commercialization of the first LIB in 1991 [1] marks a major event in the portable electronics revolution that has swept through society over the past three decades. The success of LIBs in portable application is intimately related to their comparably high energy density, as well as, their good cyclability. The same virtues are key arguments for choosing the LIB as the energy storage device for electrification of off-the-grid transportation. However, these new applications require a significant increase in gravimetric (Wh kg^{-1}) and volumetric (Wh L^{-1}) energy densities, longer cycle life, higher tolerance for high power operation, lower cost, as well as, better large unit safety, in order to replace the current combustion engine technology.

LIB, like all batteries, rely on an electrochemical cell, where the positive and negative electrode parts of the overall redox reaction are separated by an electrolyte that exclusively conducts ions and an external circuit that exclusively conducts electrons. It is thus in the external circuit, where injection and harvest of the electric energy stored chemically in the cell takes place. An important feature of the LIB is that lithium has the most negative redox potential of any metal, which ensures that a large cell operating potential can be reached when combined with an appropriate positive electrode reaction and an organic electrolyte, typically $LiPF_6$ in organic carbonates.

Rechargeable batteries require that the redox processes of the electrodes be highly reversible; *e.g.* a 0.1 % irreversibility loss per cycle, leads after five years of one charge/discharge per day to a battery with only 16 % of the initial capacity! This extreme requirement for chemical reversibility, as well as, safety concerns when using metallic lithium has led to the development of the LIB where both electrodes are based on lithium ion intercalation into solids (Figure 1.1.).

Consequently, lithium ions are shuttled between the positive and negative electrode during the charge and discharge processes to charge compensate the solids during the redox reaction, hence the "ion" part of LIB, which are also known as rocking chair batteries.[2]

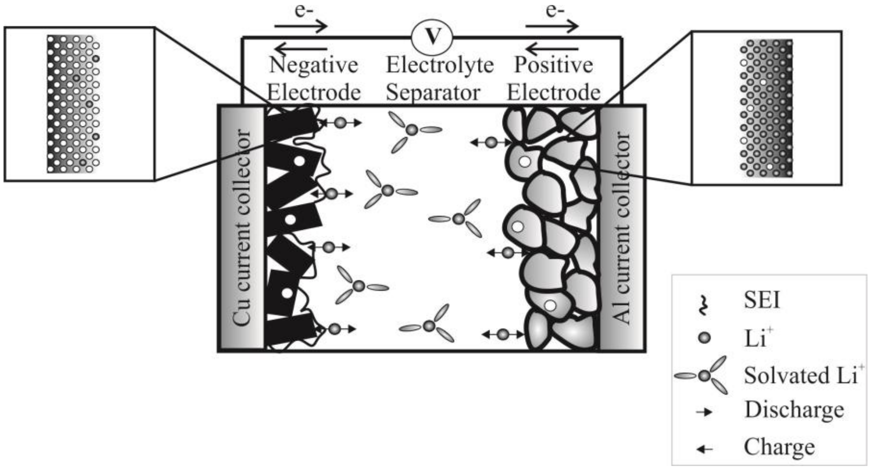

Figure 1.1. Schematic illustration of the operating principle in LIBs.

While the original materials combination chosen by SONY, *i.e.* graphite negative electrode and $LiCoO_2$ positive electrode, have provided sufficient reversibility to ensure that it is still among the most common for portable electronics LIBs, these batteries still suffer from parasitic reactions that limit performance. One example is the surface reaction between the negative electrode and the electrolyte that continues during cycling, which leads to formation of an increasingly thick and resistive solid electrolyte interphase (SEI) layer. These type of challenges are further compounded when designing for transportation application due to the required increase in operation potential, the use of low cost but potentially soluble manganese, increase in surface area as the insertion material particles are nano-sized to shorten the charge transport within the solid and accommodate the more rapid volume changes associated with high power performance *etc*. Moreover, these problems may be non-uniformly distributed over the sample, due in part to non-uniform electrochemical use of the electrodes, particle-to-particle variation and particle surface heterogeneity. A manifold of analysis tools, which can probe locally, will therefore be highly valuable for development of new LIB with improved performance. Herein, we review such a class of tools, known collectively as scanning probe microscopy (SPM).

1.2. ELECTROCHEMICAL MEASUREMENTS USING SCANNING PROBE MICROSCOPY TO STUDY LITHIUM ION BATTERIES FUNDAMENTAL MECHANISMS AND PROCESSES

SPMs bring extensive *ex-situ*, *in-situ* and *operando* local characterization opportunities of battery materials.[3] The basic requirements for SPMs are that i) a local probe be positioned in close proximity to the surface or alternatively brought into contact with the surface with sufficiently small force that neither the probe nor the surface be significantly deformed; and ii) that an imaging system converts a signal at every point into an image that is related to a physical/chemical quantity of the sample surface.[4] The nature of the desired interaction between the probe and surface then defines the type of microscopy used. For example, STM[5] measures a tunneling current between the surface and the probe. STM is used to study LIB material because of its ability to measure electronic properties combined with surface topography with high spatial resolution.[6] AFM[7], and its derivatives like KPM[8], c-AFM, SSRM, ESM are based on probes consisting of a tip placed at the extreme of a cantilever, where a laser beam reflection from the backside serves to gauge the forces exerted on the probe. AFM informs on mechanical properties (surface roughness, mechanical toughness, and expansion/contraction) at the nanoscale[9], which are altered during (de-)lithiation in LIB electrode materials, as well as, surface layer growth, both impacting the life and capacity of the battery.[10] KPM tracks the surface potential difference enabling *in-situ* probing of structural and chemical changes occurring at different locations in an aging battery material.[11] SSRM allows quantitative measurements of variation in contact resistance between a probe and a substrate, requiring significant mechanical pressure be exerted at the probe.[12] SSRM is used for studying aging mechanisms in LIBs since the battery impedance increase with ageing is often linked to an increase in surface resistance of the electrode.[13] In ESM, [14] the application of a high frequency periodic potential at the probe or the surface induces localized volume change due to ionic movement that is detected as probe movement. This ionic response to an electric field similar to conductivity is a key property for lithium-ion electrode material design, since it is often the solid ionic transport that limits the performance. SECM, SECCM, SICM, and SVET are based on monitoring electrochemical potential through the measurement of current or potential at the surface of a microelectrode (SECM[15] and SVET[16]) or at the apex of a micropipette electrode (SECCM[17] and SICM[18]). Classically, surface-to-probe distance in these techniques is based on electrochemical signal change with vertical movement of the probe over the surface. *E.g.* SVET provides surface redox activity, by vibrating a microelectrode above the substrate and measuring the potential gradients resulting from ionic transport. As such, it has served to provide the two-dimensional distribution of ionic currents *in-situ* from SEI layer covered metal electrodes.[16a] Since these electrochemical probe techniques monitor local fluxes of electroactive species, they are inherently useful for visualization of redox activity in LIB electrodes at the nano to micron scale[18], and thus for monitoring the material aging.[17]

Due to space limitations the focus herein is on the electroactive parts of the battery with Table 1.1. providing an overview of SPM applied to LIB organized by techniques and the following text organized according to the nature of the electrode and SEI-layer. SPM techniques have however also been successfully applied to the study of novel separators [19] as well as solid electrolytes [20] illustrating the vast versatility of these techniques.

Table 1.1. *Overview of SPM Applied to LIB*

Method	Extracted information	Materials
AFM incl. conductive AFM	Topography	$LiCoO_2$,[10a, 21] $LiNi_{0.8}Co_{0.2}O_2$,[22] $LiMn_2O_4$,[23] $LiFePO_4$,[24] V_2O_5,[25] Graphite,[26] Si–Sn,[27] $Li_{1.2}Co_{0.13}Ni_{0.13}Mn_{0.54}O_2$,[28] Silicon[29]
	Interlayer distances	Graphite[30]
	Lithium transport	$LiCoO_2$[31]
	Electronic properties	$LiMn_2O_4$,[23e] $LiNi_{0.8}Co_{0.2}O_2$[32]
	SEI: thickness	Graphite[26b]
	SEI: formation	Silicon,[29, 33] Graphite[26b]
	Mechanical properties	Silicon,[34] SEI (Silicon)[35]
AFM-SECM	SEI: electrochemical properties, Topography	Glassy carbon[36]
ESM	Lithium transport and Electrochemical properties	$LiCoO_2$,[31,37] $LiFePO_4$,[38] $Li_{1.2}Co_{0.13}Ni_{0.13}Mn_{0.54}O_2$,[28] $LiCo_{0.33}Ni_{0.33}Mn_{0.33}O_2$,[39] $LiMn_2O_4$,[40] Silicon[14, 41]
KPM	Surface potential	$LiFePO_4$[11]
SECM	Lithium transport	$LiCoO_2$,[42] Lithium in PC[43]
	Electronic properties	TiO_2[44]
	Leaching	$LiCoO_2$[45]
	Topography	Graphite[46]
	SEI: formation	Glassy carbon,[47] Graphite,[48] TiO_2[44]
	SEI: electrochemical properties	Metallic Li foil,[49] Glassy carbon,[47] Graphite[48a, 50]
	SEI: Defect formation	Graphite[51]

Method	Extracted information	Materials
SECCM	Electrochemical activity	$LiFePO_4$[17]
SICM	Topography	Silicon,[18] Tin film,[18] MnO[52]
	Lithium transport	Silicon,[18] Tin film[18]
	SEI: formation	MnO[52]
SSRM	Surface resistance	$LiFePO_4$[13]
STM	Topography	$LiMn_2O_4$,[6b, 23a] V_2O_5,[6a]Graphite[53]
	Electronic properties	V_2O_5[6a]
SVET	Lithium transport	Lithium metal[16]

1.3. SCANNING PROBE MICROSCOPY STUDIES OF LITHIUM ION BATTERY POSITIVE ELECTRODE MATERIAL

Widely studied positive electrode materials include *layered* $LiCoO_2$, $LiNiO_2$, and Li_2MnO_3-$LiMO_2$, *spinel* $LiMn_2O_4$, *olivine* $LiFePO_4$ and *layered* V_2O_5.[28] SPM techniques applied to positive electrode materials include AFM,[24a] KPM,[11] SSRM,[13] STM,[6b] ESM,[28] SECM,[42] and SECCM[17] which has been used to track changes in the localized material properties[23b, 54] to inform on positive electrode material aging[55], lithium transport in bulk and across interfaces, and the impact of composite electrode design.[56]

1.3.1. LITHIUM COBALT OXIDE AND OTHER LAYERED OXIDES

Layered $LiCoO_2$ is arguably the most studied system as it is one of the most important commercial positive electrode material in LIBs.[31] Consequently, substitution into this structure has become a major research field with considerable commercial success.[57]

AFM

To understand the fracturing mechanism that leads to capacity and power fading of positive electrode materials, AFM has been used to measure changes in the surface morphology at the single grain boundary and dislocation level while operating the battery,[23c, 27] allowing static strains[21], as well as, electronic currents to be mapped[9, 23e].

Balke *et al.* prior to their ESM measurements mapped volume changes associated with (de)intercalation in a single $LiCoO_2$ grains at a resolution of ~100 nm using AFM, [31] by applying a local high voltage pulses to force a redistribution of lithium ions within the solid, while at the same time imaging the topographic changes. Using the electrolyte rather than the material itself as Li^+ source and drain, Clémençon *et al*. studied *ex-situ* and *in-situ* by electrochemical AFM (EC-AFM) the morphological and dimensional changes on the surface of individual $LiCoO_2$ crystals.[21] *Ex-situ* AFM measurements revealed surface particles on the $LiCoO_2$ indicating that the surface layer is not a uniform film but exists as discrete surface particles which can be dissolved in $LiPF_6$ containing electrolyte. *In-situ* studies revealed no evidence of micro-cracks or cobalt dissolution (pitting) within the crystal upon charging indicating surface and dimensional stability of the crystals upon (de) intercalation, contrary to previous XRD studies.[58] To eliminate the effects of particle geometry and size micro-machined samples were investigated by Park et al., monitoring the positive electrode material in-situ showing expansion in volume of 1.28-1.3%.[10a]

Although $LiCoO_2$ is a successful commercialized positive electrode material, research continues to search for alternatives in order to increase energy density, lower cost, improve cycling stability and battery safety.[59] Nickel has been explored as a possible substitute for cobalt in $LiNiO_2$ as it is lower in cost and possesses a higher energy density, however it is less stable and less ordered in comparison to $LiCoO_2$.[60] The partial substitution of Co for Ni in $LiNi_{1-y}Co_yO_2$ positive electrodes produces an alternative material which holds good capacity retention, but nonetheless still experiences an inherent structural instability during long term cycling at moderate temperatures.[61] An electronic barrier and/or ionic barrier at the positive electrode's surface has been proposed to be an outcome from this structural instability and material degradation, causing the rise of positive electrode impedance.[32] C-AFM was used in combination with Raman microscopy by Kostecki and McLarnon to provide resistance information about the surface layers formed on $LiNi_{0.8}Co_{0.2}O_2$.[32] By examining electrodes cycled at different temperature, it was found that the electronic conductance followed the same trend as calendar and cycle life. By examining electrodes cycled at different temperature, it was found that the electronic conductance followed the same trend as calendar and cycle life.

ESM

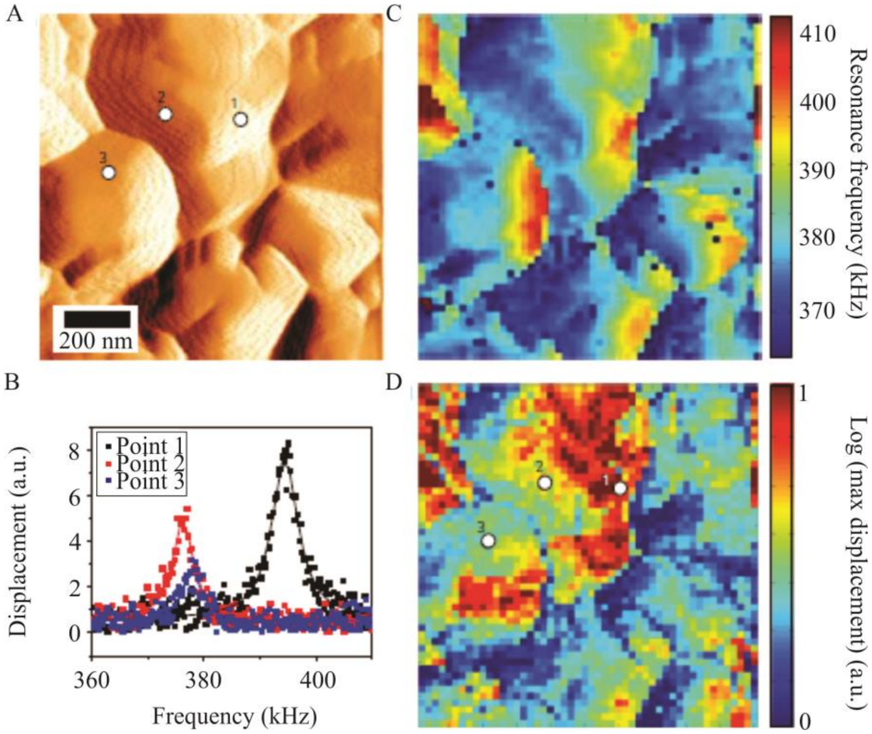

Figure 1.2. (A) The deflection signal of an area of 1 μm x 1 μm of $LiCoO_2$. (B) The strain response of the surface to a 1 V peak-to-peak AC voltage applied to the probe at three different locations in A, B, and D. (C) the resonance frequency and maximum displacement (D) of the contact resonance peak measured in a 50 x 50 point grid in the same area shown in (A).[31] Reprinted with the permission from: N. Balke, S. Jesse, A. N. Morozovska, E. Eliseev, D. W. Chung, Y. Kim, L. Adamczyk, R. E. García, N. Dudney, S. V. Kalinin, Nature Nanotechnology 2010, 5, 749-754. Copyright © 2010, Nature Publishing Group

Lithium motion within the solid has recently been investigated on the nanometer scale by ESM.[31] This SPM method enables the visualization of lithium ion diffusivity at single grains and fixed grain boundaries, detecting ~5-10% volume changes corresponding to complete (de)lithiation of the material within the ~ 20 nm regions probed as seen in (Figure 1.2.). Quantitative and spatially resolved mapping of diffusion times in nanometer scale volumes, showing significant variations of relaxation signals across active material grains indicating heterogeneous ion transport kinetics was presented by Guo *et al*. using bias-induced relaxation measurements.[37] Single crystal and polycrystalline $LiCoO_2$ film ESM data was simulated by Chung *et al*.[62] The diffusion pathway of lithium ions was found to be unidirectional in a single crystal and tortuous in the polycrystalline film. This multidirectional diffusion path induces stress locally throughout operation of the battery, ultimately diminishing its life. This investigation gives a strong theoretical basis for stating that local lithium diffusivity and crystallographic orientation of grains at the surface can be measured on the sub-one hundred nanometer scale by ESM.

Other *layered* oxides, studied the nanoscale by ESM, include $LiCo_{0.33}Ni_{0.33}Mn_{0.33}O_2$ and $Li_{1.2}Co_{0.13}Ni_{0.13}Mn_{0.54}O_2$. Zhu *et al*. report the high resolution real-space mapping of lithium ion diffusion on $LiCo_{0.33}Ni_{0.33}Mn_{0.33}O_2$ thin film solid state batteries,[39] where different stages of ageing showed a strong correlation between diffusion coefficients and capacity fading.[28] Yang *et al*. using a combination of ESM and classical AFM to observe $Li_{1.2}Co_{0.13}Ni_{0.13}Mn_{0.54}O_2$ demonstrated that the lithium ion diffusivity attenuates gradually over several bias-induced lithium ion redistributions.

SECM

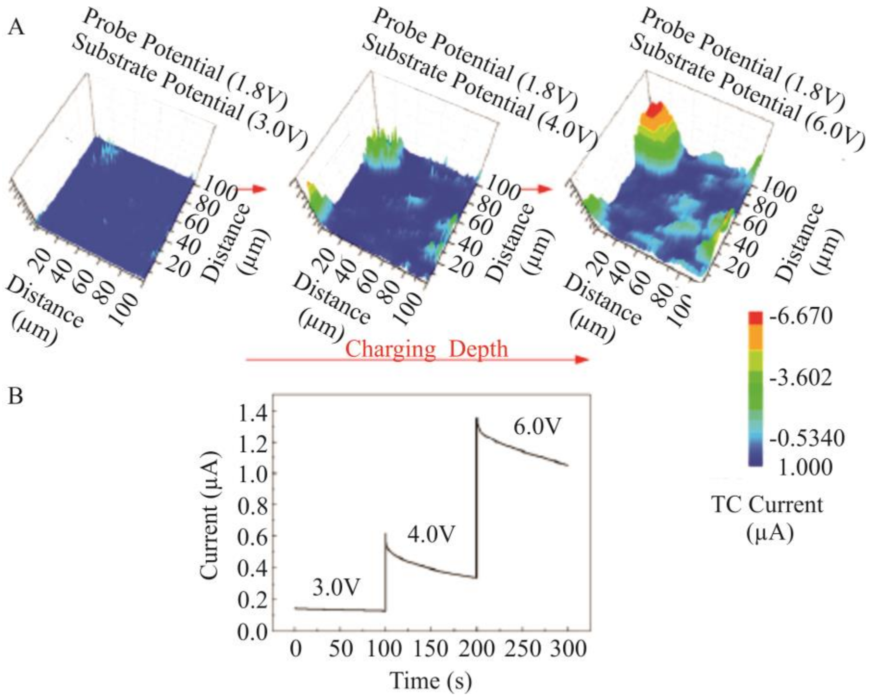

Figure 1.3. SECM images of $LiCoO_2$ substrate with the charging depth (A) (Probe: Pt) (Substrate: $LiCoO_2$) (Reference Electrode: Li metal)), and multi-potential step chronoamperometry of $LiCoO_2$ substrate applied at 3.0, 4 .0, and 6.0 V for 100 s (B).[42] Adapted with the permission from: F. Xu, B. Beak, C. Jung, Journal of Solid State Electrochemistry 2011, 16, 305-311.Copyright © 2011, Springer

Scanning microelectrode techniques like SECM[15] has also been employed on layered oxides. An *in-situ* study by Xu *et al.* on $LiCoO_2$ employed the substrate-generation/ tip-collection mode SECM in order to investigate lithium ion dissociation and transport from the charging positive electrode material.[42] The $LiCoO_2$ substrate exhibited heterogeneous electrochemistry consistent with non-uniform lithium ion transport throughout the sample (Figure 1.3.). Lithium ion quantification using a mercury amalgam microelectrode (Hg/Pt UME) SECM probe was later performed by Barton and Rodrigues-López, providing a method to directly correlate material defects and kinetic heterogeneity in electrode material with high resolution.[43] Snook *et al.* also performed SECM on $LiCoO_2$ material, but focusing on the behavior of the material in the presence of room temperature ionic liquids (RTILs), thus providing information about possible electrode degradation mechanisms.[45] It was concluded that reduction of Co^{3+} to Co^{+} entailing dissolution is a major contributor to the loss of capacity.

Spinel $LiMn_2O_4$ is known for its isotropic structure providing a 3D network for fast lithium ion diffusion and rapid (dis)charge reactions, making $LiMn_2O_4$-type materials good candidates for high-power LIBs.[63] Furthermore, $LiMn_2O_4$ is attractive due to its non-toxicity, low cost and relatively high voltage[64], yet, commercialization of this material class has been hindered by rapid capacity fade during cycling and storage, which is found to escalate at elevated temperatures.[23c, 65]

AFM

Several possible mechanisms such as the decomposition of electrolyte at high potential, slow dissolution of the material through a disproportionation reaction, and structural distortion due to the Jahn-Teller effect have been proposed and investigated.[66] A consensus on the dominating effect is however still outstanding. Zhu *et al*. investigated the effect of battery cycling on surface morphology, mechanical properties and interfacial stability using *ex-situ* tapping-mode AFM.[23b] Surface roughness increased with cycle number, whereas cycling performance and surface morphology stability remained high, suggesting that the increase of surface roughness is due to stress induced fragmentation and agglomeration of nano-grains. The creation of micro-cracks impacted the particle interconnectivity in the composite electrode, resulting in a reduced amount of material available for cycling. The origin of capacity fade of $LiMn_2O_4$ was also investigated by Doi *et al.* using contact mode *in-situ* AFM on thin film positive electrodes after repeated cycling or storage at elevated temperatures.[23c] After 100 galvanostatic cycles at elevated temperatures, the surface was covered with amorphous Li-Mn-O particles formed through a dissolution/precipitation reaction.[23a] Such morphology changes and capacity fade were not observed for thin films cycled at 25°C, consequently, they were proposed to be closely related to the $LiMn_2O_4$ capacity fade.[23c] AFM has also been used to study the connection between the surface morphology change in *spinel* $LiMn_2O_4$ and the Jahn-Teller instability. Kuriyama *et al*. applied a negative bias voltage to a conductive AFM probe to extract lithium ions from the tetrahedral sites of inner layers of the *spinel* towards the probe contact point.[23e] Volume expansion, observed as large surface morphology changes, is caused by the phase transition resulting from the lattice relaxation in $LiMn_2O_4$.[67] As such, the gradual decrease in surface roughness above 3.5 V *vs.* Li/Li$^+$ was associated with relaxation of the Jahn-Teller distortion.[23e]

ESM

ESM has been implemented by Luchkin *et al*. to measure the nanoscale lithium ion mobility in fresh and aged commercial $LiMn_2O_4$.[40a] The aged particles showed less uniform distribution of ion mobility, as well as, a decrease of diffusion coefficient by 1-2 orders of magnitude in comparison to the fresh samples. A later study by Amanieu *et al*. compared ESM $LiMn_2O_4$ measurements to a theoretical model of the time evolution of lithium concentration, surface displacement and the ESM signal below the probe during and after DC pulses.[40b] Due to the complex nature of the technique and the studied effects, discrepancies between model and experiment could not be mitigated.

STM

EC-STM was used by Inaba *et al.* to observe the surface morphology changes on $LiMn_2O_4$ thin films after galvanostatic cycling[6b]. Small particles, covering the pristine positive electrode's surface, were observed to become more numerous but smaller with cycling. It was suggested that the particles had been formed through Li-Mn-O dissolution/ precipitation reactions. The surface morphology of two stoichiometrically different $Li_{1+x}Mn_{2-x}O_4$ positive electrode materials were monitored using STM after cycling at both low and high potential by Doi *et al*.[23a] The capacity of the sample with high manganese concentration faded rapidly upon cycling at high potential, whilst small spherical particles formed to cover the electrode surface. Conversely, capacity fading was suppressed for the material with low manganese contents, concurrently, with suppression of particle formation, the morphology changes were therefore deemed to be related to the capacity fading.

Known particularly for its high safety, high cycling stability, low toxicity and low cost, *olivine* $LiFePO_4$ has found commercial application.[68] Despite this success, capacity degradation over long periods of time is still an important research area.[69]

AFM

Early AFM *ex-situ* studies on $LiFePO_4$ showed an increase in nanoparticle agglomeration with ageing of the battery[69], and later *in-situ* studies at various degrees of charging found significant particle shape and size changes, which was linked to unit cell volume difference of Li^+ release and uptake. [24] Importantly analyzing four particles, surface changes were found to be inhomogeneous thus suggesting non-uniform utilization of the electrode. [24b]

ESM

ESM has also been used to investigate the difference in lithium ion concentration and diffusivity between micro- and nanocrystalline $LiFePO_4$ under different states of charge by Chen *et al.*[38] $LiFePO_4$ is known to be able to accommodate more lithium defects in smaller crystallites, which should enhance lithium diffusivity.[70] The ESM mappings of samples with two different morphologies showed different strain levels at each different charge state (Figure 1.4.), which is attributed to larger amounts of lithium ion intercalation in the nanocrystalline material. The analysis also revealed that the redistribution of lithium ions in the nanocrystalline $LiFePO_4$ showed much smaller energy dissipation and thus smaller energy barriers for lithium ion (de)intercalation, confirming the expected behavior.

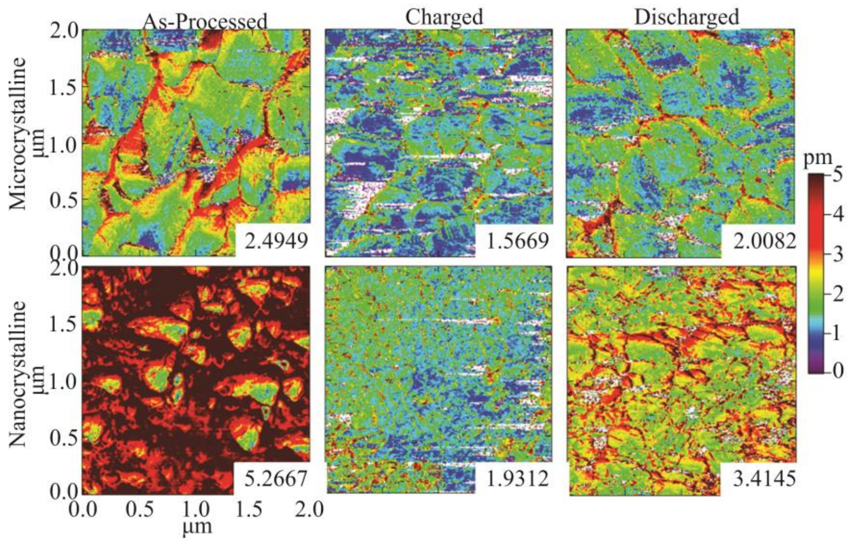

Figure 1.4. Corrected ESM amplitude mappings of LiFePO4 electrode in micro- and nano- crystalline areas at different stages of processing and testing. The averaged amplitude is given in the right bottom corner of the maps.[38] Reprinted with the permission from: Q. Nataly Chen, Y. Liu, Y. Liu, S. Xie, G. Cao, J. Li, Applied Physics Letters 2012, 101, 063901.Copyright © 2012, AIP Publishing LLC

Nagpure *et al.* used KPM for the first time to characterize aged $LiFePO_4$ positive electrodes of LIBs, showing that a larger charge sustaining capacity in the unaged sample was found compared to the aged sample under the same externally applied voltage.[11] By utilizing SSRM, the variations in the contact resistance of samples can be measured with high spatial resolution (< 15 nm). As such, carbon coated $LiFePO_4$ has been used to investigate the changes in surface resistance as a result of aging.[13] By comparison of pristine and aged electrodes, topography and resistance maps were constructed showing a coarsening of the particles, as well as, an increase in surface resistance of the cycled cells. The authors attribute the resistance increase to the loss of carbon coating due to coarsening of the material and to the formation of a nanocrystalline deposit layer similar to the one observed by Kostecki and McLarnon's on $LiNi_{0.8}Co_{0.2}O_2$ positive electrode surfaces.[32] Takahashi and co-workers introduced SECCM as a technique to measure the electrochemical activity of $LiFePO_4$ at the nanoscale, which enabled mapping of the local heterogeneous redox activity with resolution of ~ 100 nm.[17]

1.3.4. VANADIUM PENTOXIDE

AFM

Layered vanadium pentoxide V_2O_5 is a promising candidate as a positive electrode material in LIBs due to its high energy density and its overall faradic capacity which is close to 420 mAh g^{-1}[71] it has however not met with commercial success in part due to its fast capacity fading with cycling, and is thus a subject of continued study.[72] As such, *In-situ* AFM was used by Światowska-Mrowiecka *et al*. to study the nanostructure of V_2O_5, which showed flattening and lateral extension of the grains during repeated cycling.[25] Furthermore, the surface of the grains exhibited new ridges within the thin film, resulting from plastic deformation of the material.

V_2O_5 as a thin film positive electrode material within an all solid state battery was studied *in-situ* by Semenov *et al*. with ultrahigh vacuum STM.[6a] The results show nano-sized heterogeneities in conductance at the interface between positive electrode and solid electrolyte, which was associated with the local structure modifications due to lithium ion intercalation and linked to capacity fading in this type of battery.

1.4. SCANNING PROBE MICROSCOPY STUDIES OF LITHIUM ION BATTERY NEGATIVE ELECTRODE MATERIAL

1.4.1. LITHIUM BASED MATERIALS

Historically lithium based batteries featured negative electrodes of lithium metal, leading to dendritic growth of lithium during repetitive cycling.[16] In order to suppress the loss of coulombic efficiency caused by the dendritic deposition of Li, the use of inorganic (*i.e.* Mg^{2+}, Zn^{2+}, In^{3+}, Ga^{3+}, Sn^{2+} and AlI_3) and organic (*i.e.* 2-methylthiophene (2MeTp), 2-methyltetrahydrofuran (2MeTHF) and 2-methylfuran (2MeF)) additives was proposed.[16] The inorganic additives were expected to create a thin layer of Li metal alloys, while organic additives targeted higher conductance SEI-layers. *In-situ* SVET has been used to investigate the magnitude and the two-dimensional distribution of ionic current at the interface between metallic lithium and the organic electrolyte in the presence and the absence of these additives. Results from the Ishikawa group showed that Al inorganic additives improved homogeneity of the current distribution compared to the pure lithium metal, and a Sn inorganic additive.[16c] Consequently, the formation of a Li/Al surface alloy was suggested to reduce dendrite growth. Furthermore, they also observed a synergistic effect on the cycling efficiency when using aluminium iodide (AlI_3) in conjunction with 2MeF. The potential gradient map of the combination additive displayed a highly uniform current distribution with no inactive site.[16a] A correlation between the uniformity and the magnitude of the Li ionic current obtained by SVET and the coulombic efficiency has been reported.[16a,b]

1.4.2. GRAPHITE BASED MATERIALS

The problem of dendritic lithium growth on lithium metal has been overcome with the use of lithium intercalation graphite negative electrodes, which exhibit a highly negative and flat lithium intercalation potential and long cycle life, at low cost and toxicity.[73] Unfortunately, compared to silicon presented in section 1.4.3, graphite lags far behind in capacity (theoretical only 372 mAh g^{-1}) and power.[74] The low working potential of graphite leads to a partial reduction of most lithium battery electrolyte solutions, and the decomposition products deposit as the SEI layer.[75] The SEI, which can form both on negative and positive electrode materials, has a major impact on the electrode stability and performance, and is therefore the subject of intense study that will be discussed separately in section 1.5.

STM

In-situ electrochemical STM (ECSTM) probed exfoliation mechanisms, which are detrimental to the operation of the battery, on highly oriented pyrolytic graphite (HOPG) and its solvent dependence. Inaba and coworkers studied the atomically flat basal plane of HOPG in 1 M $LiClO_4$ in ethylene carbonate-diethyl carbonate EC + DEC (1:1) and in propylene carbonate PC. In EC/DEC, surface morphology changes were strongly dependent on bias voltage. [53a] When the potential was stepped to 1.1 V *vs.* Li/Li^+, 8-10 Å height hill-like structures appeared, which was linked to solvent cointercalation. Wan and coworkers studied morphology change on HOPG in $LiPF_6$ dissolved in EC-DMC. The initial lithium uptake when the potential is stepped below 1.50 V vs. Li/Li^+, leads to exfoliation of the graphite at the step edge. Consequently, the height of the step was also strongly correlated to the exfoliation initial potential. When the potential was further reduced to 0.8-0.7 V *vs.* Li/Li^+, they observed the growth of clusters and flakes on the step edge ascribed to the formation of ternary graphite intercalation compounds, the growth of small island clusters with poor conductivity on the terrace attributed to the reduction product of EC as well as the exfoliation of the graphite layers. [53e]

In comparison, PC electrolyte showed faster exfoliation and rapid rupture of the graphite layer. Importantly, exfoliation is accompanied with the regeneration of highly reactive edge planes hindering formation of stable protective films. Inaba *et al.* thus conclude that intercalation of lithium ions is essential to the formation of a stable film on graphite. [53b] Finally, the use of $LiClO_4$ dissolved in trifluoropropylene carbonate (TFPC), lead to slow exfoliation of the graphite layers at potentials between 1.0 and 1.1 V and irregular-shape swelling of graphite layers. In contrast with the above studied PC electrolyte, the degree of exfoliation in $LiClO_4$ dissolved TFPC was not found to cause catastrophic graphite deterioration.[53c]

AFM

AFM brings many opportunities for studying failure mechanisms,[29, 76] morphology and volume change, [27, 29, 77] *In-situ* AFM was used to study the morphology, dimensional evolution, degradation and exfoliation during the intercalation and (de)intercalation process of lithium on graphite. For example by monitoring the local evolution of the graphene interlayer distance, an irreversible increase was observed in the first cycle followed by reversible swelling/shrinking in subsequent cycles.[30] AFM experiment performed on HOPG also demonstrated that exfoliation occurs on edge, as well as, basal planes. On basal planes, the formation of fine cracks was observed first, followed by the evolution of large blisters.[26a]

SECM

The feedback mode of SECM has been used to quantify the physical swell ratio of graphite composite electrodes. Physical swelling occurs when electrolyte is taken up by the composite battery material prior to electrochemical cycling. The SECM experiments performed inside an Ar-filled glove box imaged the non-uniform swelling and measured the time evolution of local film thicknesses of composited electrodes having greater roughness and thickness (*i.e.* 100 µm for graphite composite electrode) than what is conventionally measured by AFM. In comparing the swell ratios obtained for composite electrodes consisting of graphite particles, conductive agents and polyvinylidene fluoride (PVDF) to that of a model PVDF electrode, the authors demonstrated the physical swelling and topographical change of the composite electrode were mainly attributed to the swelling of the PVDF binder in interaction with the electrolyte.[46]

1.4.3. SILICON BASED MATERIALS

Silicon has a promising initial capacity of ~4200 mAh g^{-1}, approximately 10 times more than the traditional graphite negative electrode. However, Si negative electrodes experience significant capacity loss due to severe volume changes during cycling (up to 400 %), cracking and pulverization.[78]

ESM

ESM has been used to map mobility and electrochemical reactivity in amorphous Si negative electrodes.[14, 41] The image displays the presence of strong ESM activity or highly active transport pathways at sharp grain boundaries and hot-spots at defect locations.[14a] Balke *et al.* demonstrated the high-resolution power of ESM by mapping the evolution of the local lithium ion flow during high-frequency—high-voltage cycling of the battery material with an effective spatial resolution below ~20 nm. The results provided a direct nano-scale view of the lithium ion flow in the Si negative electrode, showing an evolution in response from random spots to highly localized regions at the grain boundary sites when comparing pristine and cycled samples, respectively.[14b]

AFM

In-situ AFM [29, 34] and AFM/STM [79] were used to investigate mechanical properties of silicon for LIBs during lithiation and delithiation. *In-situ* AFM nanoindentation, a technique in which the AFM probe interact strongly with the surface to obtain stress-strain information, has been used to examine amorphous silicon (a-Si) nanopillars with different dimensions.[34] The samples were measured *ex-situ* before cycling and then *in-situ* at two lithium levels during lithiation and delithiation. It was shown that volume changes, interface properties and mechanical degradation were size dependent and that pillars with a diameter of 500 nm exhibited maximum recovery of the mechanical properties, thus guiding future morphology designs.[34] *In-situ* AFM has also been used to compare performance of a-Si in different geometries.[29b] Comparing, a confined pit and pillars, the pit structure exhibited high cycling efficiency, yet, to further improve performance Atomic Layer Deposition (ALD) coating have been proposed. *In situ* AFM imaging clearly show the morphological differences between ALD coated and un-coated materials (Figure 1.5.). [29b] Using this information, the authors conclude that a 3 nm layer was ideal in protecting the surface, whilst allowing sufficient ionic conduction. ALD coatings hampered cracking and material erosion from the bulk even post cycling based on c-AFM analysis that demonstrated that the majority of ALD coated material remained electrically insulating after cycling. [29b]

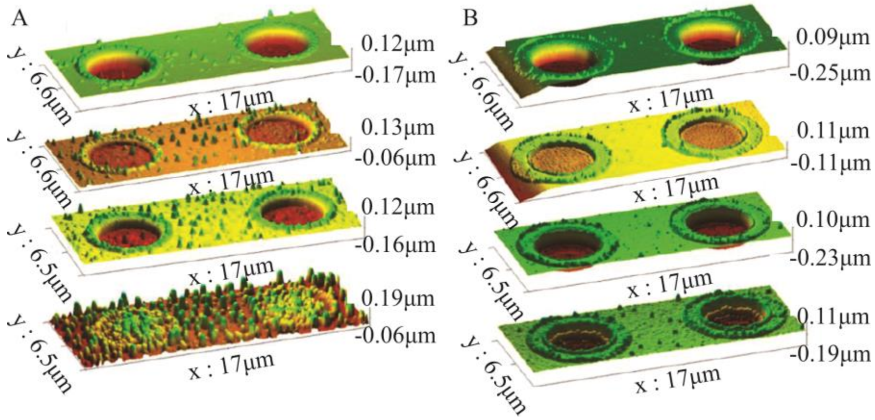

Figure 1.5. AFM images of a-Si pits cycled in 3:7 EC: EMC with 1.2 M $LiPF_6$ with and without 3 nm of ALD in panels A and B respectively. The top image is at OCP, the second image is the first lithiation, the third image is the first delithiation, and the bottom image is after 10 complete cycles. The sloping portion on the left side of the top two rows of panel b is an artifact of AFM imaging.[29b] Adapted with the permission from: C. R. Becker, S. M. Prokes, C. T. Love, ACS Applied Materials and Interfaces 2016, 8, 530-537.Copyright © 2016, American Chemical Society

1.5. SCANNING PROBE MICROSCOPY STUDIES OF SOLID ELECTROLYTE INTERPHASE

The SEI is an electronically insulating but ionically conducting layer deposited on the negative electrode, and is attributed to the degradation electrolyte at low potential.[80] In depth understanding of SEI formation is crucial for the fine-tuning the electrolyte from which it is formed. However, due to its very thin nature, sensitivity to air and humidity, and heterogeneous morphology characterization of the SEI to provide consistent data is very difficult also by SPM methods.

AFM

AFM was used to evaluate the morphology of the SEI,[26a, 27, 81] and to monitor *in-situ* the SEI formation process,[33, 82] in order to determine the effect of different additives, solvents and salts on the properties of the SEI,[82a, 83] to investigate the SEI mechanical properties[35, 82j, 84] and to assess the quality of the film formed.[85]

AFM nano-identation analysis evaluated the surface contact stiffness of the SEI on a silicon negative electrode. Upon addition of alkoxysilanes to the electrolyte a significant increase in contact stiffness was observed, suggesting an improvement in mechanical adhesion, binding properties and the ability to withstand large volume change during cycling.[84a] Chen and coworkers used AFM topography and AFM force spectroscopy measurements, to study morphology, structure, mechanical property, evolution of the SEI, specifically quantifying the mechanical properties (Young's modulus) and inhomogeneity of the SEI layer. The force curves obtained by AFM force spectroscopy measurements displayed the mechanical response of single layered and double-layered SEI film consistent with a multilayered model.[35] Recently, Xu *et al.* used *in-situ* AFM with electrochemical control in combination with *ex-situ* X-ray photo electron spectroscopy (XPS) to study the *in-situ* formation of the SEI film (Figure 1.6.) on highly oriented pyrolytic graphite (HOPG). [26b] From the open circuit voltage (OCV≈ 2.5 V) to 2.1 V (V1 to V2), no interface layer is visible on the AFM image. At 2.1 V (V2) the reduction of O_2 contamination from the electrolyte is observed as an increase in cathodic current. Between V2 and V3, interfacial species along edge sites accumulated and were associated with the intercalation of solvated Li^+ in HOPG and subsequent reduction of the ethylene carbonate. Around 1.0 V (V3) the basal plane is completely covered with surface species well before the HOPG lithiation at approximately 0 V. [26b]

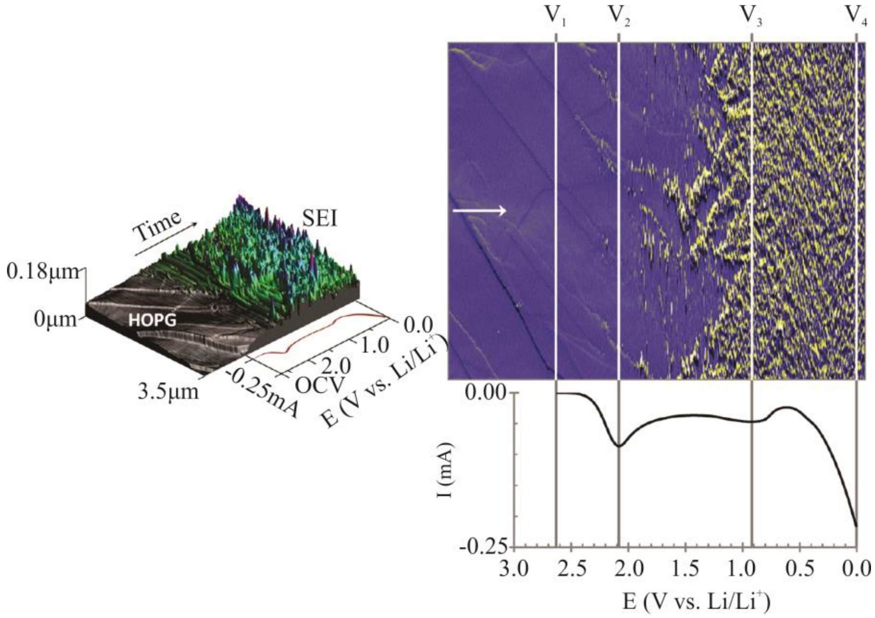

Figure 1.6. AFM analysis of the formation of the SEI on HOPG in 1.5 M LiTFSI dissolved in EC imaged (top) during electrochemical potential sweep (bottom). Vertical lines correspond to key features described in the text. The arrow indicates the slow scan direction. The image lines to the right are at lower potential and later time than lines to the left. Image parameters: 3.5 x 4.5 μm^2. The collected topographic image was differentiated to highlight height variations with strong contrast, in which the leading edges and rough areas appear more yellow and descending edges and smooth areas appear more blue. Adapted with the permission from: A. V. Cresce, S. M. Russell, D. R. Baker, K. J. Gaskell, K. Xu, Nano Letters 2014, 14, 1405-1412.Copyright © 2014, American Chemical Society

In-situ AFM measurements on silicon negative electrodes were performed in order to determine the impact of the initial cycling conditions on the SEI formation. The authors demonstrate the challenges of stabilizing the formed SEI on Si negative electrodes given the irreversible expansion of Si features after the first cycle. Their study suggests that faster initial cycling with a fast stabilization of the SEI leads to a smoother and thinner SEI layer that is stabilized even after slower succeeding lithiation / delithiation cycles.[33]

SECM

SECM brings opportunities for *in-situ* and *in-operando* characterization of the SEI, including formation, stability and passivating properties. Passivation was found to depend on the nature of negative electrode and nature of the electrolyte used. *E.g.* Using 2,5-di-tertbutyl-1,4-dimethoxy benzene as a mediator, the electron transfer rate across the SEI was found to be slightly superior on the lithiated graphite compared to the lithium foil.[49] Schuhmann and coworkers, investigated *in-operando* SEI formation and stability on glassy carbon[47] and graphite[48a], specifically to examine the electrolyte additive vinylene carbonate (VC) effect on SEI formation. They found that a strong resistive behavior was initiated at 0.8 V *vs.* Li/Li$^+$ in electrolytes without VC, while 1.3 V *vs.* Li/Li$^+$ was required when VC was present.

SEI defect formation can compromise safety as well as decrease the lifetime of LIBs. Differencing defects from gradual change of the SEI properties is therefore of great interest. Bülter *et al.* found short and long-term spatiotemporal variations in electron transfer rate of Li foil and graphite negative electrodes, indicative of damage of the SEI[49] Long term variations were tied to the nature of the electrolyte solution[49] where as another *in-situ* SECM study attributed short-term or spontaneous variations to volume change or expansion during galvanostatic cycling, dissolution of SEI components, gas-bubble formation and detachment (Figure 1.7.).[51]

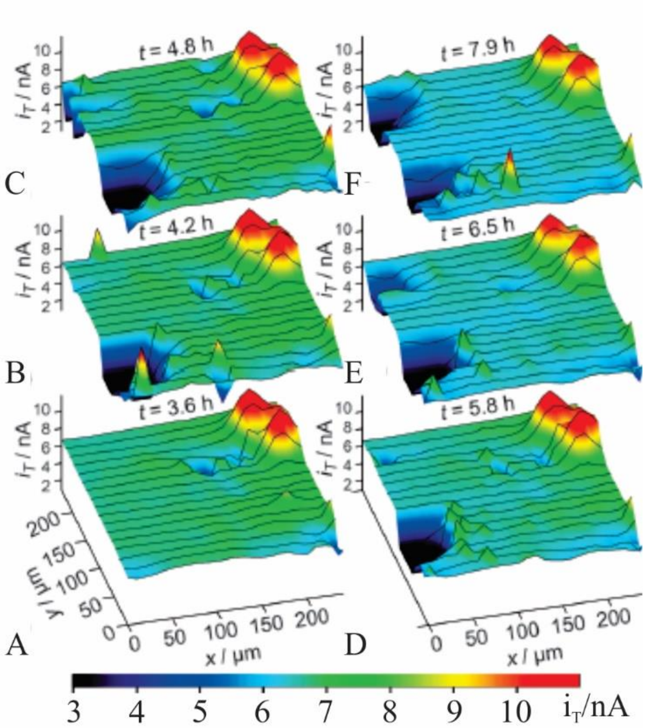

Figure 1.7. Detection of gas-bubble formation within a sequence of SECM FB images of an identical region of a SEI-covered graphite electrode recorded A) 3.6 h, B) 4.2 h, C) 4.8 h, D) 5.8, E) 6.5 h, and F) 7.9 h after filling electrolyte solution in the SECM cell at a distance (d) ≈3 µm.[51] Reprinted with the permission from: H. Bülter, F. Peters, J. Schwenzel, G. Wittstock, Angewandte Chemie International Edition 2014, 53, 10531-10535.Copyright © 2014, John Wiley and Sons

In-situ visualization and kinetic analysis of SEI formation as well as lithium (de)intercalation using SECM has also been applied to TiO_2.[44] Titanium-ion based negative electrodes have attracted considerable attention due the relatively low redox potential of the Ti^{3+}/Ti^{4+} redox couple in oxides as well as the low density of Ti. Specifically, $Li_4Ti_5O_{12}$ has meet with commercial success as a high rate negative electrode material.[86] SECM was used to investigate *in-situ* the Li^+ ions (de)insertion in *anatase* TiO_2 nanoparticles based paste negative electrode material and to investigate the kinetics of SEI formation.[44a] The insertion of Li^+ ions in titania occurs at 1.65V *vs.* Li/Li^+ and the (de)insertion at 2.2V *vs.* Li/Li^+. An increase in feedback current was observed when the TiO_2 potential was swept from 3.0 V to 1.5 V *vs.* Li/Li^+ attributed to the increased driving force for the local reduction of the chosen redox species (Fc/Fc^+). However, when the applied potential reach the Li^+ insertion potential, in Li^+ containing electrolyte, the increase in feedback signal is considerably more pronounced (more than double) compared to Li free electrolyte. This is followed by a decrease back to its original value when the potential was swept back from 1.5 V to 2.5 V *vs.* Li/Li^+. This process was found to be reversible for Li^+ containing and Li^+ free solutions. As such this experiment serves to quantify the effect of Li ions insertion on the conductivity of the paste electrode. As expected, when the potential was swept to a potential where SEI formation would occur (0.8 V *vs.* Li/Li^+), the feedback current irreversibly decreased.[44a]

Finally, a platform that combined AFM and SECM in an Ar-filled glovebox was used to study the electrochemical properties of the SEI formed on glassy carbon electrodes. Topography changes were investigated using AFM, with the conclusion that the SEI was starting to form at a potential of ca. 0.6 V *vs.* Li/Li^+. Dissolution of the SEI during the anodic scan could not be observed. Through scratching of the surface, the consequences of SEI film failure could be studied with SECM feedback mode.[36] Clearly, this combined approach within a protective gas environment has the potential to uncover other unresolved mechanisms within the battery environment.

(SICM)

Modern SICM simultaneously records topography and ion current with sub-pA sensitivity. As such, it is well-suited to measure spatially resolved Li^+ ion currents which has been applied to silicon and tin negative electrodes.[18] Figure 1.8. displays the SICM *in-situ* topographic and current maps before and after lithiation. Inhomogeneities in the topographic and ionic current maps was attributed to electrochemical processes such as lithiation and inhomogeneous SEI formation [18]

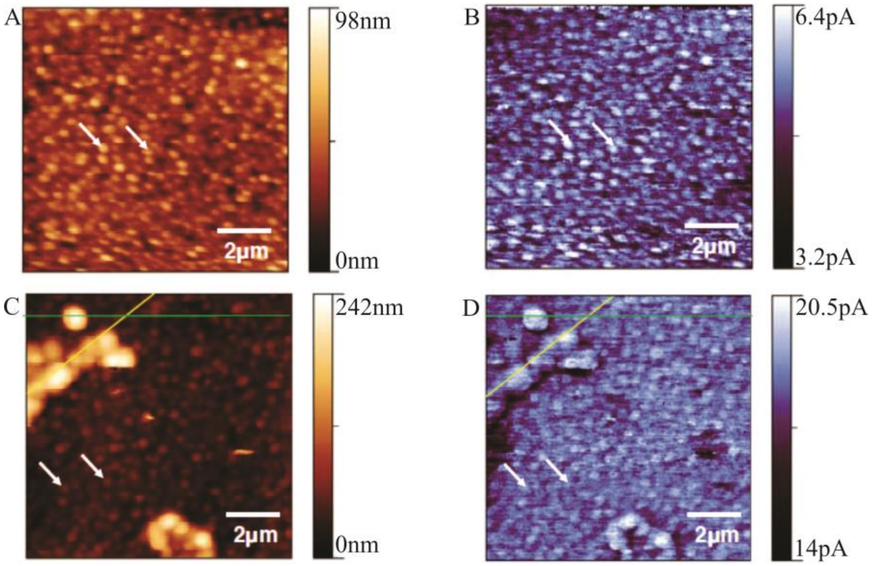

Figure 1.8. SICM (A,C) topography and (B,D) DC current images of a 60 nm thick tin thin film deposited on a 60 nm thick copper thin film on glass (A,B) before lithiation and (C,D) after 24 $\mu Ahcm^{-2}$ lithiation.[18] Reprinted with the permission from: A. L. Lipson, R. S. Ginder, M. C. Hersam, Advanced Materials 2011, 23, 5613-5617. Copyright © 2011, John Wiley and Sons

In-situ SICM imaging has also been used to investigate atomic layer deposition (ALD) alumina (Al_2O_3) coatings on MnO. Whereas uncoated MnO grows a thick SEI, a 3 Å Al_2O_3 coat reduces SEI formation, and 9 Å can inhibit it nearly completely (Figure 1.9.).[52] Importantly, Figure 9b shows a region where, despite being coated, the SEI formation has still occurred, suggesting the presence of defects in the protective layer.

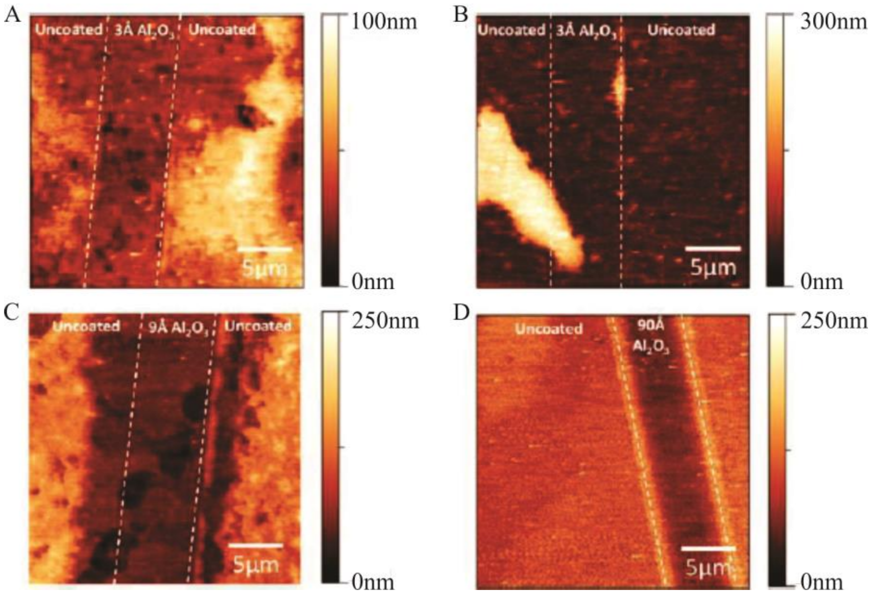

Figure 1.9. SICM topography images of samples that have undergone one electrochemical cycle with lithographically defined Al2O3 stripes on the surface of MnO. (A, B) Two different regions of a sample with stripes of 3 Å thick ALD Al2O3 on the surface of MnO. (C) 9 Å thick and (D) 90 Å thick stripes of ALD Al$_2$O$_3$.[52] Reprinted with the permission from: A. L. Lipson, K. Puntambekar, D. J. Comstock, X. Meng, M. L. Geier, J. W. Elam, M. C. Hersam, Chemistry of Materials 2014, 26, 935-940.Copyright © 2014, American Chemical Society

1.6. SUMMARY AND OUTLOOK

Analytical techniques based on X-ray diffraction and spectroscopy, as well as, electron microscopies and other classical materials characterization methods have been and will likely continue to be the work horses of LIB research. However as the works reviewed here show, SPMs are poised to bring a significant addition to the battery researcher's toolbox. Their very nature where only volumes in the immediate vicinity of the probe are measured makes them unique tools to quantify ionic fluxes and to examine the electroactive solid-electrolyte interphase, which have been notoriously difficult using classical techniques especially under *operando* conditions. The relative simplicity of the SPM instrument compared to synchrotrons and high performance electron microscopes should make SPM methods available to a wide range of battery researchers. Further, the continued development of new SPM modes and techniques like electrochemical tip-enhanced Raman spectroscopy,[87] opens a wide range of new nanoscale characterization opportunities, some of which hopefully will be instrumental in the development of the new LIB that will enable large scale storage and transportation of energy produced by sustainable means.

1.7. DEVELOPMENT OF MICRO-AND NANO SECM PROBES FOR PROSPECTIVE APPLICATION IN LITHIUM ION BATTERIES

As mentioned earlier, this work presents the development of a high resolution SECM based technique for the quantitative detection of Mn^{2+} cations. SECM is an electroanalytical technique that involves scanning the surface of a substrate in a solution containing an electroactive species using an UME (electrodes with a dimension smaller than 25 μm) [88] placed in close proximity to the substrate surface. The geometry of the UME tip significantly influences the signal received in SECM. There are several possible UME geometries, including disk, [89] hemispherical, [90] inlaid ring, [91] ring-disk, [92] and finite conical, [93] which are depicted in Figure 10.

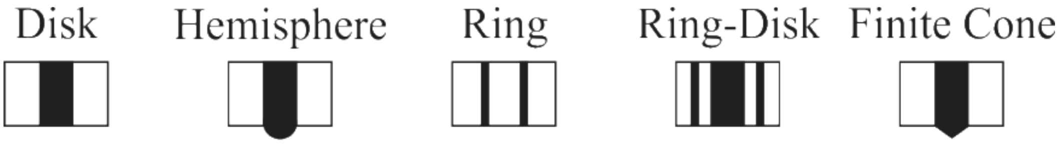

Figure 1.10. Several UMEs geometries including disk, hemispherical, inlaid ring, ring-disk, and finite conical

Between these geometries, the disk geometry is the most frequently used. Here, an electroactive material (such as platinum, gold, silver or carbon fiber) is embedded in a thin insulating layer. The development and fabrication UMEs with an ideal geometry is a challenge that faces several research group, and is the focus of several articles and reviews. The standard technique for the fabrication of gold or platinum disk UMEs with 10 or 25 μm diameters begins with sealing one end of a glass capillary (usually borosilicate for gold or quartz for platinum) using a Bunsen burner or a torch. The gold or platinum wire is then inserted into the open end of the capillary and positioned at the sealed end by vibrating the capillary. Using a heated coil, the glass is then sealed around the metal wire under vacuum. The UME tip is then polished to expose the electroactive surface using a polishing machine and a fine grit paper. In order to minimize the overall size of the electrode, the electrode is sharpened by rotating it over grit paper at a 45° angle. This technique results in UMEs with an electroactive surface diameter in the micron size and large glass to electroactive surface ratio. Finally, electrical and physical connections to the platinum or gold wire are made to fit the SECM platform. [94]

There are several advantages to reducing the size of an electrode, including an increased spatial resolution in SECM, which allows for the acquisition of higher resolution scans. A fabrication method for disk micro- electrodes with small overall size and controlled geometry is presented in chapter 2. A conventional methods to produce sub-micrometer sized UME involves sealing and pulling a metal wire inside a glass capillary using a CO_2 laser-based micropipette puller system is presented in chapter 3.[89]

The signal received in SECM is a combination of the flux densities of electrochemically active species with respect to the surface's electrochemical properties and a topography. Appropriate understanding of the behavior of these UMEs is vital for the flux quantification and the analysis of surface properties. The diffusion process at the surface of an electrode is size and geometry dependent. With a larger electrode the mass-transport occurs perpendicularly to the surface (also called planar diffusion) whereas with a microelectrode a spatial diffusion field develops (also known as hemispherical diffusion). When the UME is in the bulk solution, away from any surface, the current is governed by hemispherical diffusion. When approaching a UME towards a non-electroactive surface (i.e. a surface which does not regenerate redox active species) the diffusion of the species to the electrode is hindered by the presence of the surface, and therefore the faradaic current recorded by the UME is reduced compared to the measurement in the bulk solution. When approaching a UME towards a conductive substrate an increase of tip current can be observe due to an enhanced regeneration of redox species at the substrate surface.[95]

We have successfully developed a method for the fabrication for disk micro- and nano-electrodes with controlled geometry, which were used as backbones for the production of Hg-based hemispherical ASV sensors for the quantitative detection of Mn^{2+}. Hg-based hemispherical UMEs offer several advantages in comparison to the disk UMEs, including a large electrolyte potential window, enhanced sensitivity, a well-defined and smoother surface, and better approximation of the zero tip-to-substrate distance.

The Hg hemispherical nano sized electrodes were used for the quantitative detection of manganese cations for prospective LIBs applications.

[1] B. Dunn, H. Kamath, J. M. Tarascon, Science, 334 (2011), 928-935.

[2] S. Megahed, B. Scrosati, Journal of Power Sources, 51 (1994), 79-104.

[3] a) P. De Wolf, E. Brazel, A. Erickson, Materials Science in Semiconductor Processing, 4 (2001), 71-76; b) T. Schweinböck, S. Schömann, D. Alvarez, M. Buzzo, W. Frammelsberger, P. Breitschopf, G. Benstetter, Microelectronics Reliability, 44 (2004), 1541-1546.

[4] A. J. Bard, G. Inzelt, F. Scholz, Electrochemical dictionary, Springer Science & Business Media, (2008).

[5] G. Binnig, H. Rohrer, C. Gerber, E. Weibel, Physical Review Letters, 49 (1982), 57-61.

[6] a) A. E. Semenov, I. N. Borodina, S. H. Garofalini, Journal of The Electrochemical Society, 148 (2001), A1239-A1246; b) M. Inaba, T. Doi, Y. Iriyama, T. Abe, Z. Ogumi, Journal of Power Sources, 81–82 (1999), 554-557.

[7] G. Binnig, C. F. Quate, C. Gerber, Physical Review Letters, 56 (1986), 930-933.

[8] W. Melitz, J. Shen, A. C. Kummel, S. Lee, Surface Science Reports, 66 (2011), 1-27.

[9] R. García, R. Pérez, Surface Science Reports, 47 (2002), 197-301.

[10] a) J. Park, S. Kalnaus, S. Han, Y. K. Lee, G. B. Less, N. J. Dudney, C. Daniel, A. M. Sastry, Journal of Power Sources, 222 (2013), 417-425; b) R.-R. Liu, X. Deng, X.-R. Liu, H.-J. Yan, A.-M. Cao, D. Wang, Chemical Communications, 50 (2014), 15756-15759.

[11] S. C. Nagpure, B. Bhushan, S. S. Babu, Journal of Power Sources, 196 (2011), 1508-1512.

[12] G. Benstetter, R. Biberger, D. Liu, Thin Solid Films, 517 (2009), 5100-5105.

[13] S. C. Nagpure, B. Bhushan, S. Babu, G. Rizzoni, Scripta Materialia, 60 (2009), 933-936.

[14] a) N. Balke, S. Jesse, Y. Kim, L. Adamczyk, I. N. Ivanov, N. J. Dudney, S. V. Kalinin, ACS Nano, 4 (2010), 7349-7357; b) N. Balke, S. Jesse, Y. Kim, L. Adamczyk, A. Tselev, I. N. Ivanov, N. J. Dudney, S. V. Kalinin, Nano Letters, 10 (2010), 3420-3425.

[15] E. Ventosa, W. Schuhmann, Physical chemistry chemical physics : PCCP, 17 (2015), 28441-28450.

[16] a) M. Ishikawa, S. Yoshitake, M. Morita, Y. Matsuda, Journal of the Electrochemical Society, 141 (1994), L159-L161; b) Y. Matsuda, M. Ishikawa, S. Yoshitake, M. Morita, Journal of Power Sources, 54 (1995), 301-305; c) M. Ishikawa, M. Morita, Y. Matsuda, Journal of Power Sources, 68 (1997), 501-505.

[17] Y. Takahashi, A. Kumatani, H. Munakata, H. Inomata, K. Ito, K. Ino, H. Shiku, P. R. Unwin, Y. E. Korchev, K. Kanamura, T. Matsue, Nature Communications, 5 (2014), 1-7.

[18] A. L. Lipson, R. S. Ginder, M. C. Hersam, Advanced Materials, 23 (2011), 5613-5617.

[19] a) J. HunáKim, Journal of Materials Chemistry, 21 (2011), 8192-8198; b) R.-S. Juang, C.-T. Hsieh, P.-A. Chen, Y.-F. Chen, Journal of Power Sources, 286 (2015), 526-533.

[20] a) P. Raghavan, X. Zhao, J. Manuel, C. Shin, M.-Y. Heo, J.-H. Ahn, H.-S. Ryu, H.-J. Ahn, J.-P. Noh, G.-B. Cho, Materials Research Bulletin, 45 (2010), 362-366; b) C. Jangu, A. M. Savage, Z. Zhang, A. R. Schultz, L. A. Madsen, F. L. Beyer, T. E. Long, Macromolecules, 48 (2015), 4520-4528; c) X. Su, T. Zhang, X. Liang, H. Gao, B. W. Sheldon, Acta Materialia, 98 (2015), 175-181.

[21] A. Clémençon, A. T. Appapillai, S. Kumar, Y. Shao-Horn, Electrochimica Acta, 52 (2007), 4572-4580.

[22] X. Zhang, P. N. Ross, R. Kostecki, F. Kong, S. Sloop, J. B. Kerr, K. Striebel, E. J. Cairns, F. McLarnon, Journal of The Electrochemical Society, 148 (2001), A463-A470.

[23] a) T. Doi, M. Inaba, Y. Iriyama, T. Abe, Z. Ogumi, Journal of The Electrochemical Society, 155 (2008), A20-A23; b) J. Zhu, K. Zeng, L. Lu, Electrochimica Acta, 68 (2012), 52-59; c) T. Doi, M. Inaba, H. Tsuchiya, S. K. Jeong, Y. Iriyama, T. Abe, Z. Ogumi, Journal of Power Sources, 180 (2008), 539-545; d) F. T. Quinlan, K. Sano, T. Willey, R. Vidu, K. Tasaki, P. Stroeve, Chemistry of Materials, 13 (2001), 4207-4212; e) K. Kuriyama, A. Onoue, Y. Yuasa, K. Kushida, Surface Science, 601 (2007), 2256-2259.

[24] a) S. Ramdon, B. Bhushan, S. C. Nagpure, Journal of Power Sources, 249 (2014), 373-384; b) D. E. Demirocak, B. Bhushan, Journal of colloid and interface science, 423 (2014), 151-157.

[25] J. Światowska-Mrowiecka, V. Maurice, L. Klein, P. Marcus, Electrochemistry Communications, 9 (2007), 2448-2455.

[26] a) F. P. Campana, H. Buqa, P. Novák, R. Kötz, H. Siegenthaler, Electrochemistry Communications, 10 (2008), 1590-1593; b) A. V. Cresce, S. M. Russell, D. R. Baker, K. J. Gaskell, K. Xu, Nano Letters, 14 (2014), 1405-1412.

[27] L. Y. Beaulieu, V. K. Cumyn, K. W. Eberman, L. J. Krause, J. R. Dahn, Review of Scientific Instruments, 72 (2001), 3313-3319.

[28] S. Yang, B. Yan, T. Li, J. Zhu, L. Lu, K. Zeng, Physical chemistry chemical physics : PCCP, 17 (2015), 22235-22242.

[29] a) C. R. Becker, K. E. Strawhecker, Q. P. McAllister, C. A. Lundgren, ACS Nano 2013, 7, 9173-9182; b) C. R. Becker, S. M. Prokes, C. T. Love, ACS Applied Materials and Interfaces, 8 (2016), 530-537.

[30] F. P. Campana, R. Kötz, J. Vetter, P. Novák, H. Siegenthaler, Electrochemistry Communications, 7 (2005), 107-112.

[31] N. Balke, S. Jesse, A. N. Morozovska, E. Eliseev, D. W. Chung, Y. Kim, L. Adamczyk, R. E. García, N. Dudney, S. V. Kalinin, Nature Nanotechnology, 5 (2010), 749-754.

[32] R. Kostecki, F. McLarnon, Electrochemical and Solid-State Letters, 5 (2002), A164-A166.

[33] A. Tokranov, B. W. Sheldon, C. Li, S. Minne, X. Xiao, ACS Applied Materials & Interfaces, 6 (2014), 6672-6686.

[34] Q. P. McAllister, K. E. Strawhecker, C. R. Becker, C. A. Lundgren, Journal of Power Sources, 257 (2014), 380-387.

[35] J. Zhang, R. Wang, X. Yang, W. Lu, X. Wu, X. Wang, H. Li, L. Chen, Nano Letters, 12 (2012), 2153-2157.

[36] G. Zampardi, S. Klink, V. Kuznetsov, T. Erichsen, A. Maljusch, F. LaMantia, W. Schuhmann, E. Ventosa, ChemElectroChem, 2 (2015), 1607-1611.

[37] S. Guo, S. Jesse, S. Kalnaus, N. Balke, C. Daniel, S. V. Kalinin, Journal of The Electrochemical Society, 158 (2011), A982-A990.

[38] Q. Nataly Chen, Y. Liu, Y. Liu, S. Xie, G. Cao, J. Li, Applied Physics Letters, 101 (2012), 063901.

[39] J. Zhu, L. Lu, K. Zeng, ACS nano, 7 (2013), 1666-1675.

[40] a) S. Y. Luchkin, K. Romanyuk, M. Ivanov, A. L. Kholkin, Journal of Applied Physics, 118 (2015), 072016 ; b) H.-Y. Amanieu, H. N. M. Thai, S. Y. Luchkin, D. Rosato, D. C. Lupascu, M.-A. Keip, J. Schröder, A. L. Kholkin, Journal of Applied Physics, 118 (2015), 055101.

[41] S. Jesse, N. Balke, E. Eliseev, A. Tselev, N. J. Dudney, A. N. Morozovska, S. V. Kalinin, ACS Nano, 5 (2011), 9682-9695.

[42] F. Xu, B. Beak, C. Jung, Journal of Solid State Electrochemistry, 16 (2011), 305-311.

[43] Z. J. Barton, J. Rodríguez-López, Analytical Chemistry, 86 (2014), 10660-10667.

[44] a) G. Zampardi, E. Ventosa, F. La Mantia, W. Schuhmann, Electroanalysis, 27 (2015), 1017-1025; b) G. Zampardi, E. Ventosa, F. La Mantia, W. Schuhmann, Chemical Communications, 49 (2013), 9347-9349.

[45] G. A. Snook, T. D. Huynh, A. F. Hollenkamp, A. S. Best, Journal of Electroanalytical Chemistry, 687 (2012), 30-34.

[46] H. Bülter, F. Peters, J. Schwenzel, G. Wittstock, Journal of the Electrochemical Society, 163 (2016), A27-A34.

[47] G. Zampardi, F. La Mantia, W. Schuhmann, RSC Advances, 5 (2015), 31166-31171.

[48] a) G. Zampardi, F. La Mantia, W. Schuhmann, Electrochemistry Communications, 58 (2015), 1-5; b) J. Hui, M. Burgess, J. Zhang, J. Rodríguez-López, ACS Nano, 10 (2016), 4248-4257.

[49] H. Bülter, F. Peters, J. Schwenzel, G. Wittstock, Journal of the Electrochemical Society, 162 (2015), A7024-A7036.

[50] H. Bülter, P. Schwager, D. Fenske, G. Wittstock, Electrochimica Acta, 199 (2016), 366-379.

[51] H. Bülter, F. Peters, J. Schwenzel, G. Wittstock, Angewandte Chemie International Edition, 53 (2014), 10531-10535.

[52] A. L. Lipson, K. Puntambekar, D. J. Comstock, X. Meng, M. L. Geier, J. W. Elam, M. C. Hersam, Chemistry of Materials, 26 (2014), 935-940.

[53] a) M. Inaba, Z. Siroma, A. Funabiki, Z. Ogumi, T. Abe, Y. Mizutani, M. Asano, Langmuir, 12 (1996), 1535-1540; b) M. Inaba, Z. Siroma, Y. Kawatate, A. Funabiki, Z. Ogumi, Journal of Power Sources, 68 (1997), 221-226; c) M. Inaba, Y. Kawatate, A. Funabiki, S.-K. Jeong, T. Abe, Z. Ogumi, Electrochimica Acta, 45 (1999), 99-105; d) E. Peled, C. Menachem, D. Bar-Tow, A. Melman, Journal of The Electrochemical Society, 143 (1996), L4-L7; e) L. Wang, X. Deng, P. X. Dai, Y. G. Guo, D. Wang, L. J. Wan, Physical Chemistry Chemical Physics, 14 (2012), 7330-7336.

[54] J. Zhu, J. Feng, L. Lu, K. Zeng, Journal of Power Sources, 197 (2012), 224-230.

[55] Y. Xia, Y. Zhou, M. Yoshio, Journal of The Electrochemical Society, 144 (1997), 2593-2600.

[56] G. V. Zhuang, G. Chen, J. Shim, X. Song, P. N. Ross, T. J. Richardson, Journal of Power Sources, 134 (2004), 293-297.

[57] C. Pillot, in The Rechargeable Battery Market and Main Trends 2014-2025, 32nd International Battery Seminar and Exhibit, Fort Lauterdale, FL, USA, March 9 (2015).

[58] a) G. G. Amatucci, J. M. Tarascon, L. C. Klein, Solid State Ionics, 83 (1996), 167-173; b) Z. Chen, Z. Lu, J. R. Dahn, Journal of The Electrochemical Society, 149 (2002), A1604-A1609.

[59] a) D. Belov, M.-H. Yang, Journal of Solid State Electrochemistry, 12 (2007), 885-894; b) D. Belov, M.-H. Yang, Solid State Ionics, 179 (2008), 1816-1821; c) M. S. Whittingham, Chemical Reviews, 104 (2004), 4271-4302; d)J. W. Fergus, Journal of Power Sources, 195 (2010), 939-954.

[60] a) T. Amriou, B. Khelifa, H. Aourag, S. M. Aouadi, C. Mathieu, Materials Chemistry and Physics, 92 (2005), 499-504; b) A. Rougier, P. Gravereau, C. Delmas, Journal of the Electrochemical Society, 143 (1996), 1168-1175.

[61] a) J. Cho, H. Jung, Y. Park, G. Kim, H. S. Lim, Journal of The Electrochemical Society, 147 (2000), 15-20; b) R. V. Chebiam, F. Prado, A. Manthiram, Journal of the Electrochemical Society, 148 (2000), A49-A53.

[62] D.-W. Chung, N. Balke, S. V. Kalinin, R. Edwin García, Journal of The Electrochemical Society, 158 (2011), A1083-A1089.

[63] a) T. Ohzuku, M. Kitagawa, T. Hirai, Journal of the Electrochemical Society, 137 (1990), 769-775; b) I. Yamada, T. Abe, Y. Iriyama, Z. Ogumi, Electrochemistry Communications, 5 (2003), 502-505.

[64] F. Simmen, A. Hintennach, M. Horisberger, T. Lippert, P. Novák, C. W. Schneider, A. Wokaun, Journal of The Electrochemical Society, 157 (2010), A1026-A1029.

[65] G. G. Amatucci, C. N. Schmutz, A. Blyr, C. Sigala, A. S. Gozdz, D. Larcher, J. M. Tarascon, Journal of Power Sources, 69 (1997), 11-25.

[66] a) D. H. Jang, Y. J. Shin, S. M. Oh, Journal of the Electrochemical Society, 143 (1996), 2204-2211;

b) X. Wang, H. Nakamura, M. Yoshio, Journal of Power Sources, 110 (2002), 19 26; c) C. Y. Ouyang, S. Q. Shi, M. S. Lei, Journal of Alloys and Compounds, 474 (2009), 370-374.

[67] M. M. Thackeray, W. I. F. David, P. G. Bruce, J. B. Goodenough, Materials Research Bulletin, 18 (1983), 461-472.

[68] P. P. R. M. L. Harks, F. M. Mulder, P. H. L. Notten, Journal of Power Sources, 288 (2015), 92-105.

[69] S. C. Nagpure, B. Bhushan, S. S. Babu, Journal of the Electrochemical Society, 160 (2013), A2111-A2154.

[70] N. Meethong, H. Y. S. Huang, W. C. Carter, Y. M. Chiang, Electrochemical and Solid-State Letters, 10 (2007), 134-138.

[71] A. Tranchant, R. Messina, J. Perichon, Journal of Electroanalytical Chemistry and Interfacial Electrochemistry, 113 (1980), 225-232.

[72] A. Gies, B. Pecquenard, A. Benayad, H. Martinez, D. Gonbeau, H. Fuess, A. Levasseur, Solid State Ionics, 176 (2005), 1627-1634.

[73] S. Goriparti, E. Miele, F. De Angelis, E. Di Fabrizio, R. Proietti Zaccaria, C. Capiglia, Journal of Power Sources, 257 (2014), 421-443.

[74] K. Persson, V. A. Sethuraman, L. J. Hardwick, Y. Hinuma, Y. S. Meng, A. van der Ven, V. Srinivasan, R. Kostecki, G. Ceder, The Journal of Physical Chemistry Letters, 1 (2010), 1176-1180.

[75] R. Marom, S. F. Amalraj, N. Leifer, D. Jacob, D. Aurbach, Journal of Materials Chemistry, 21 (2011), 9938-9954.

[76] D. Aurbach, M. Koltypin, H. Teller, Langmuir, 18 (2002), 9000-9009.

[77] a) Y. Domi, T. Doi, T. Yamanaka, T. Abe, Z. Ogumi, Journal of the Electrochemical Society, 160 (2013), A678-A683; b) M. Kitta, T. Akita, Y. Maeda, M. Kohyama, Langmuir, 28 (2012), 12384-12392.

[78] U. Kasavajjula, C. Wang, A. J. Appleby, Journal of Power Sources, 163 (2007), 1003-1039.

[79] A. Kushima, J. Y. Huang, J. Li, ACS Nano, 6 (2012), 9425-9432.

[80] V. A. Agubra, J. W. Fergus, Journal of Power Sources, 268 (2014), 153-162.

[81] S. K. Jeong, M. Inaba, Y. Iriyama, T. Abe, Z. Ogumi, Journal of Power Sources, 119-121 (2003), 555-560.

[82] a) S. Yamaguchi, H. Asahina, K. A. Hirasawa, T. Sato, S. Mori, Molecular Crystals and Liquid Crystals Science and Technology. Section A. Molecular Crystals and Liquid Crystals, 322 (1998), 239-244; b) D. Alliata, R. Kötz, P. Novák, H. Siegenthaler, Electrochemistry Communications, 2 (2000), 436-440; c) S.-K. Jeong, M. Inaba, T. Abe, Z. Ogumi, Journal of The Electrochemical Society, 148 (2001), A989-A993; d) P. Novák, F. Joho, M. Lanz, B. Rykart, J.-C. Panitz, D. Alliata, R. Kötz, O. Haas, Journal of Power Sources, 97–98 (2001), 39-46; e) S. Leroy, F. Blanchard, R. Dedryvère, H. Martinez, B. Carré, D. Lemordant, D. Gonbeau, Surface and Interface Analysis, 37 (2005), 773-781; f) I. T. Lucas, E. Pollak, R. Kostecki, Electrochemistry Communications, 11 (2009), 2157-2160; g) Y. Domi, M. Ochida, S. Tsubouchi, H. Nakagawa, T. Yamanaka, T. Doi, T. Abe, Z. Ogumi, The Journal of Physical Chemistry C, 115 (2011), 25484-25489; h) L. Wang, D. Deng, L. C. Lev, S. Ng, Journal of Power Sources, 265 (2014), 140-148; i) X. Deng, X. Liu, H. Yan, D. Wang, L. Wan, Science China Chemistry, 57 (2014), 178-183; j) X.-R. Liu, X. Deng, R.-R. Liu, H.-J. Yan, Y.-G. Guo, D. Wang, L.-J. Wan, ACS Applied Materials & Interfaces, 6 (2014), 20317-20323; k) A. Tokranov, R. Kumar, C. Li, S. Minne, X. Xiao, B. W. Sheldon, Advanced Energy Materials (2016), 1502302.

[83] a) S. K. Jeong, M. Inaba, R. Mogi, Y. Iriyama, T. Abe, Z. Ogumi, Langmuir, 17 (2001), 8281-8286; b) S.-K. Jeong, M. Inaba, Y. Iriyama, T. Abe, Z. Ogumi, Electrochimica acta, 47 (2002), 1975-1982; c) O. Matsuoka, A. Hiwara, T. Omi, M. Toriida, T. Hayashi, C. Tanaka, Y. Saito, T. Ishida, H. Tan, S. S. Ono, S. Yamamoto, Journal of Power Sources, 108 (2002), 128-138; d) R. Mogi, M. Inaba, S. K. Jeong, Y. Iriyama, T. Abe, Z. Ogumi, Journal of the Electrochemical Society, 149 (2002), A1578-A1583; e) Y. Domi, M. Ochida, S. Tsubouchi, H. Nakagawa, T. Yamanaka, T. Doi, T. Abe, Z. Ogumi, Journal of the Electrochemical Society, 159 (2012), A1292-A1297; f) J. Zhang, X. Yang, R. Wang, W. Dong, W. Lu, X. Wu, X. Wang, H. Li, L. Chen, The Journal of Physical Chemistry C, 118 (2014), 20756-20762; g) L. Martin,

H. Martinez, M. Ulldemolins, B. Pecquenard, F. Le Cras, Solid State Ionics, 215 (2012), 36-44.

[84] a) W. Xu, S. S. S. Vegunta, J. C. Flake, Journal of Power Sources, 196 (2011), 8583-8589; b) H. Shin, J. Park, S. Han, A. M. Sastry, W. Lu, Journal of Power Sources, 277 (2015), 169-179; c) J. Zheng, H. Zheng, R. Wang, L. Ben, W. Lu, L. Chen, L. Chen, H. Li, Physical Chemistry Chemical Physics, 16 (2014), 13229-13238.

[85] M. Inaba, H. Tomiyasu, A. Tasaka, S.-K. Jeong, Z. Ogumi, Langmuir, 20 (2004), 1348-1355.

[86] T.-F. Yi, S.-Y. Yang, Y. Xie, Journal of Materials Chemistry A, 3 (2015), 5750-5777.

[87] Z.-C. Zeng, S.-C. Huang, D.-Y. Wu, L.-Y. Meng, M.-H. Li, T.-X. Huang, J.-H. Zhong, X. Wang, Z.-L. Yang, B. Ren, Journal of the American Chemical Society, 137(2015), 11928-11931.

[88] A.J. Bard, L.R. Faulkner, Electrochemical Methods: Fundamentals and Applications, 2 (1980) 169.

[89] a) L. Danis, M.E. Snowden, U.M. Tefashe, C.N. Heinemann, J. Mauzeroll, Electrochimica Acta, 136 (2014) 121-129; b) B.B. Katemann, W. Schuhmann, Electroanalysis, 14 (2002) 22-28.

[90] a) J. Velmurugan, J.M. Noël, M.V. Mirkin, Chemical Science, 5 (2013) 189-194; b) J. Mauzeroll, E.A. Hueske, A.J. Bard, Analytical Chemistry, 75 (2003) 3880-3889.

[91] a) Y. Takahashi, A.I. Shevchuk, P. Novak, Y. Murakami, H. Shiku, Y.E. Korchev, T. Matsue, Journal of the American Chemical Society, 132 (2010) 10118-10126; b) Y. Lee, A.J. Bard, Analytical Chemistry, 74 (2002) 3626-3633.

[92] a) S.L.R. Harvey, P. Coxon, D. Bates, K.H. Parker, D. O'Hare, Sensors and Actuators, B: Chemical, 129 (2008) 659-665; b) P. Liljeroth, C. Johans, C.J. Slevin, B.M. Quinn, K. Kontturi, Electrochemistry Communications, 4 (2002) 67-71.

[93] a) F.R.F. Fan, M.V. Mirkin, A.J. Bard, Journal of Physical Chemistry, 98 (1994) 1475-1481; b) M.V. Mirkin, F.R.F. Fan, A.J. Bard, Journal of Electroanalytical Chemistry, 328 (1992) 47-62.

[94] C.G. Zoski, Handbook of electrochemistry, Chapter 6, 2007.

[95] A.J. Bard, M.V. Mirkin, Scanning Electrochemical Microscopy, Chapter 1, 2001.

CHAPTER 2: FABRICATION OF CARBON, GOLD, PLATINUM, SILVER AND MERCURY ULTRAMICROELECTRODES WITH CONTROLLED GEOMETRY

As new materials for LIBs are getting developed the need for analytical techniques to characterize these nano-sized materials is also evolving. SECM has great potential for application to the study of energy materials to gain a more in-depth understanding of LIBs. Indeed, SECM has been proven a powerful technique to monitor *in situ* the degradation of battery materials, to determine the solubilisation mechanism linked to capacity fading and to probe the SEI formation *in operendo*. SECM involves positioning an ultramicroelectrode (UME) in close proximity (few microns) to a substrate, and laterally scanning the surface of the substrate to detect flux densities of electrochemically active species with respect to the surface chemical properties. As will be discuss in greater detail in this chapter, the geometry of the UME tip greatly influences the signal received in SECM. The sensing portion of the UME consists of a conducting material sealed within an insulating sheath. In particular, a small insulating sheath radius to active surface radius ratio (R_g) increases the current response measured. Additionally, the smaller R_g decreases the probability of contact between the insulating sheath of the UME and the sample allowing one to work at smaller tip-to-substrate distances and therefore allowing higher resolution. The work presented in Chapter 2, tackles the problem of reducing the R_g of UMEs in order to improve the resolution in SECM and increases our ability to consistently produce reproducible sensors.

The work presented in this chapter was originally published and is adapted with permission from: Danis L., Polcari D., Kwan A., Gateman S.M., Mauzeroll J., *Fabrication of Carbon, Gold, Platinum, Silver and Mercury Ultramicroelectrodes with Controlled Geometry*. Analytical Chemistry. 2015, 87 (5), 2565-2569. Copyright © 2015, American Chemical Society.

Danis L., Noyhouzer A.T., Snowden M.E., Tefashe U. M., Mauzeroll J., “Electrochemical Flow Cell and Ultramicroelectrode”. 2016, International (PCT) Patent Application No. PCT/CA2016/050314; Danis L., Mauzeroll J., “Ultramicroelectode Devices and Manufacturing Methods”. 2015, US patent application No. 62/200,156. McGill Report of Invention (ROI) number 16005

2.1. ABSTRACT

A simple, fast, and reproducible method for the fabrication of disk UMEs with controlled geometry is reported. The use of pre-pulled soda-lime glass capillaries allows one to bypass the irreproducible torch-sealing and experimentally challenging tip-sharpening steps used in conventional fabrication protocols. A micron-sized electroactive wire is sealed inside this capillary producing UMEs with a highly reproducible geometry. Total fabrication time (1h) and experimental difficulty are significantly reduced. Disk UMEs with various diameters and cores were fabricated, including carbon fiber (7 and 11 μm), gold (10 and 25 μm), platinum (10 and 25 μm), silver (25 μm), and mercury (25 μm). The ratio of the insulating sheath to the electroactive core of the UMEs was 2.5 – 3.6. Silver UMEs were also used to produce Ag/AgCl micro-reference electrode. This general fabrication method can be readily applied to other electroactive cores, and could allow any research group to produce high quality disk UMEs, which are a prerequisite for quantitative scanning electrochemical microscopy.

2.2. INTRODUCTION

UMEs are defined as electrodes with at least one dimension smaller than 25 μm.[1] They offer several advantages including small size, high sensitivity, fast steady state response, low double-layer charging currents, and small ohmic losses.[2] The development and fabrication of UMEs has been the subject of several reviews.[3, 4] Common geometries include disk,[5, 6] hemispherical,[7, 8] inlaid ring,[9, 10] ring-disk,[11, 12] and finite conical.[13, 14] The most frequently used geometry is disk, whereby an electroactive material is embedded in a thin insulating layer. UMEs have been used in a variety of applications including biological systems,[15, 16] charge transport at liquid/liquid interfaces,[17, 18] and corrosion studies.[19, 20]

The fabrication of high quality UMEs with an ideal geometry is a difficult and time-consuming process requiring experimental skill and patience. Alternatively, research groups can opt to purchase UMEs from commercial sources, but the price per UME is high (142-417 USD$). A critical geometric parameter affecting the overall quality of the UME is the R_g, defined as the ratio between the radius of the insulating sheath (r_T) and the radius of electroactive surface (a). UMEs with small R_g are essential in SECM to achieve minimal tip-to-substrate distances (d), allowing for a higher sensitivity.[21] The R_g also has a significant effect on the current recorded during SECM approach curve measurements. A smaller R_g will result in a larger current at short tip-to-substrate distances (< 5) because of enhanced contributions from back diffusion of the mediator.[22] They also decrease the probability of contact between the insulating sheath of the UME and the sample, which experimentally occurs upon axial misalignment of the UME.[4]

There are two conventional techniques for the fabrication of gold or platinum disk UMEs. The first initially seals one end of a glass capillary (usually borosilicate or quartz) using a Bunsen burner or a torch. A metal wire is then inserted into the capillary and the glass is sealed around the metal wire using a heated coil. The UME tip is then polished to expose the electroactive surface using a polisher/grit paper. To minimize the R_g, the electrode is sharpened by rotating over grit paper at a 45° angle.[3] This technique results in UMEs with an electroactive surface diameter ≥ 1 µm. The second UME fabrication technique involves sealing and pulling a metal wire inside a glass capillary using a laser-based micropipette puller system.[23]

We present herein a simple universal method for the fabrication of disk UMEs with various electroactive materials (platinum, gold, silver, mercury, and carbon fiber). This method produces highly reproducible UME geometries and decreases total fabrication time to less than one hour. Importantly for SECM applications, the resulting disk UMEs have a small R_g (2.5 – 3.6) with 90 % yield. Moreover, the fabricated disk UMEs can be used as a geometrically controlled platform to develop other UME geometries. For example, the UMEs have been used as a backbone for the production of Hg disk UMEs and Ag/AgCl micro-reference electrodes.

2.3. EXPERIMENTAL

2.3.1. MATERIALS AND REAGENTS

Gold and platinum wire (0.01 mm and 0.025 mm diameter, purity: 99.99 %; temper: hard), silver wire (0.025 mm diameter, purity: 99.99 %), and carbon fiber (0.011 mm diameter, Tex: 720; filaments: 4000; Grade: P25; Condition: Epoxy sized) were purchased from Goodfellow (U.K.). Carbon fiber (0.007 mm) was graciously donated by Bombardier (Canada). Soda-lime glass capillaries (AR8350; L.: 75 ± 0.5 mm; O.D.:1.0 ± 0.05 mm; I.D.:0.4267 ± 0.05 mm; S.:0.2867 mm) and borosilicate capillaries (L.: 75 mm; O.D.:2.0 mm; I.D.:1.16 mm) were purchased from Hilgenberg GmbH (Germany) and Sutter Instruments (U.S.A), respectively. Abrasive polishing discs (4000 grit) and alumina powder (0.05, 0.1, 0.3, 1.0 μm particle diameter) were purchased from Struers (Mississauga, Canada). Other materials included electrically conductive silver epoxy (EPO-TEK H20E; Epoxy Technology, U.S.A), copper wire (0.50 mm diameter), and gold connector pins (Heka, U.S.A). Ferrocenemethanol, potassium chloride, potassium nitrate, and hexaammineruthenium (III) chloride (Ruhex) were purchased from Sigma Aldrich (Canada). Other chemical reagents included nitric acid (10% v/v, Caledon Laboratories Ltd.) and mercury (I) nitrate dihydrate (Fisher Scientific, Canada).

2.3.2. APPARATUS

UMEs were fabricated using a P-2000 laser-based micropipette puller system (Sutter Instruments, U.S.A), a PC-10-CA vertical pipette puller (Narishige, Japan) and a vacuum pump (Edwards RV8, Edwards, Canada). The electroactive surface was exposed and polished using a Tegrapol 23 variable speed grinder/polisher (Struers, Canada). All electrochemical measurements were performed using an Electrochemical Probe Scanner 3 (HEKA Elektronik, Germany) in a three electrode setup with a platinum wire counter electrode. All potentials were recorded relative to a chloridized silver wire (in house) quasi-reference electrode, unless specified otherwise. Optical micrographs were obtained using a customized Axio Vert.A1 inverted microscope (Zeiss, Canada). The coil temperature was measured using a HH11B digital thermometer (OMEGA, Canada).

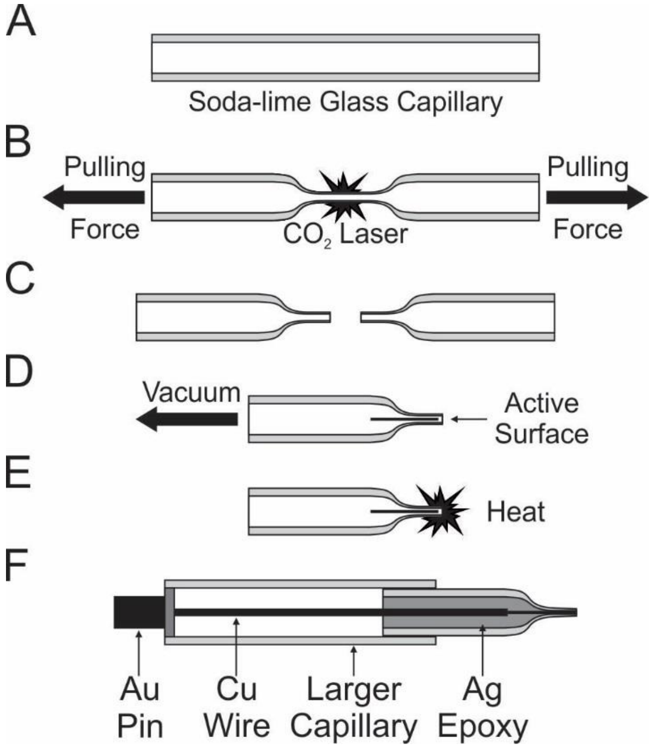

Figure 2.1. Schematic representation of pulling protocol (A) Soda-lime glass capillaries (B) Heat and a pulling force was applied to both end of the capillary using a P-2000 Laser-Based Micropipette Puller. (C) Tapered micropipette tips following pulling. (D) Insertion and positioning of the wire inside the micropipette tip. (E) Sealing of the UME using a heating coil. (F) External and electrical connections; Final UME assembly.

A complete schematic of the disk UME fabrication technique is presented in Figure 2.1. Soda-lime glass capillaries were cleaned using 10 % v/v nitric acid (1-2 hr), rinsed with nanopure water, and dried in an oven (100°C) for 12 h (Figure 2.1.A). Using a P-2000 micropipette puller, a capillary was pulled using a single line heating and pulling program (Heat: 240, Fil: 5, Vel: 60, Del: 140, Pul: 70) (Figure 2.1.B). Equal tensile force was applied at each end of the capillary along with simultaneous heat from a CO_2 laser, resulting in the production of two symmetric micropipette tips (Figure 2.1.C). A 1 cm long section of electroactive material (Ag, Au, C, or Pt) was inserted into the pulled micropipette tip. By placing the assembly tip down and lightly tapping on the open extremity of the micropipette tip, the wire/fiber travelled downwards until trapped in the sealed extremity. The assembly was then inserted into a PC-10-CA vertical pipette puller

(Figure 2.1.D). A vacuum pump was attached to the open end of the micropipette and pressure was reduced for 5 min to minimize bubble formation. The wire was sealed by centering the assembly inside a Kanthal (iron-chromium-aluminum) heating coil and applying heat for ~10-20 s after maximum temperature was reached (bright orange coil) (Figure 2.1.E). The sealed wire was connected to a Cu wire using conductive silver epoxy, which was subsequently cured for 15 min at 120 °C. The assembly was inserted into a larger borosilicate capillary to provide additional reinforcement and the overlapping edges were sealed using 5 min epoxy. A gold connector pin was then soldered to the copper wire, completing the assembly (Figure 2.1.F). The electroactive surface of the UME was exposed using a grinder/polisher (400 rpm, 4000 grit) followed by an alumina powder polishing.

2.3.4. PREPARATION OF MERCURY AND HEMISPHERICAL DISK ULTRAMICROELECTRODES

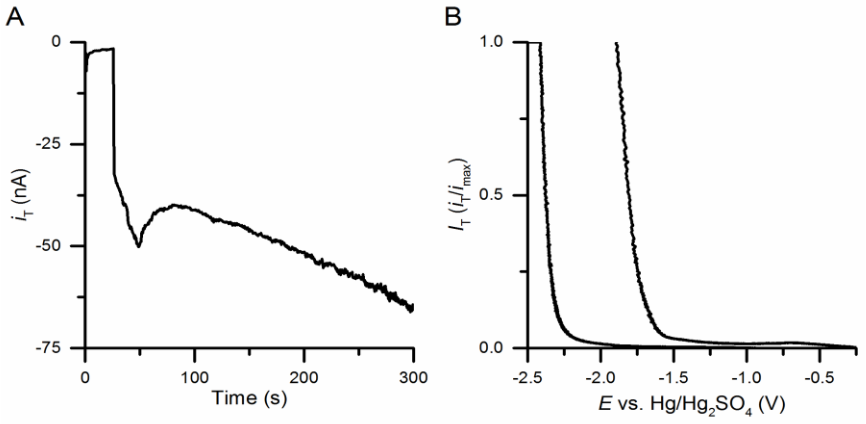

Figure 2.2. (A) Mercury deposition curve where a potential of 0 V was held for 0.35 s before a potential step of -0.5 V *vs.* Hg/Hg_2SO_4 (Sat. K_2SO_4) was applied for a duration of 300 s. (B) Linear sweep voltammetry (current-potential curve) performed at a scan rate of 10 mV s^{-1} in deaerated 0.1 M KNO_3 for the bare disk UMEs and the hemispherical Hg UMEs.

Hg hemispherical UMEs (with Ag, Au, C, or Pt) were fabricated by electrodeposition using a previously published procedure, according to the following reaction:

$$\mathrm{Hg_2^{2+}(aq) + 2e^- \leftrightarrow 2Hg\ (l)} \tag{2.1}$$

Briefly, a Hg hemisphere was electrodeposited onto the electroactive surface of a disk UME using 10 mM $Hg_2(NO_3)_2$ in 0.1 M KNO_3 acidified to 0.5 % with HNO_3 solution. The electrochemically-controlled deposition was performed by applying a potential of -0.5 V *vs.* Hg/$HgSO_4$ until the current reached π/2 (~1.57) times the initial current from the 25 μm disk UME. The Hg deposition curve is shown Figure 2.2.A.

25 μm Au disk UMEs were chemically etched by immersion in aqua regia (nitro-hydrochloric acid) solution for 10-20 min. The UME was rinsed with acetone and nanopure water to halt etching. Hg was then electrodeposited onto the recessed electroactive surface of the UME using the same procedure as for hemispherical UMEs. However, the potential was applied for a longer period of time, such that a Hg hemisphere protruded from the glass. A disk was then formed by mechanically polishing the excess Hg. As the quantity of mercury released is essentially negligible, no precaution was taken to collect the mercury from the polishing waste.

The full coverage of the electroactive surface has been investigated for both Hg disk and hemispherical UMEs. Both type of Hg UMEs display the expected shift in proton reduction to more negative potentials compared to the bare disk UMEs Figure 2.2.B. Once fabricated, the Hg UMEs were stored in degassed, 0.5% acidified 0.1 M KNO_3 solution.

2.3.5. PREPARATION OF SILVER-SILVER CHLORIDE MICRO-REFERENCE ELECTRODES

Bare 25 μm Ag disk UMEs were coated with silver chloride by immersion in 1.0 M KCl solution and the application of 2.0 V in a two-electrode setup using a Pt wire counter electrode for 20 s according to the following reaction:

$$\mathrm{AgCl_{(s)}} + \mathrm{e^-} \leftrightarrow \mathrm{Ag_{(s)}} + \mathrm{Cl^-_{(s)}} \tag{2.2}$$

The micro-reference electrodes were stored in 0.1 M KCl when not in use.

2.3.6. ELECTROCHEMICAL MEASUREMENTS

Electrochemical behavior was characterized by cyclic voltammetry and SECM approach curves. Ferrocenemethanol (FcMeOH; 1 mM) was used for Au, C, and Pt measurements, while 1 mM hexaammineruthenium (III) chloride (Ruhex) solution was used for measurements with Ag and Hg.

For cyclic voltammetry using FcMeOH, the potential was varied linearly from -100 to 400 mV, while a window of 0 to -500 mV vs. Ag was used with Ruhex. All cyclic voltammograms (CVs) were performed using a scan rate of 10 mV s^{-1}.

SECM approach curves were performed at constant potential of 400 mV for FcMeOH and -400 mV for Ruhex (-450 mV *vs.* Ag for Hg). Negative feedback approaches were performed over solvent-resistant chlorotrifluoroethylene (CTFE) plastic, while positive feedback approach curves were performed over a 1.6 mm gold disk macroelectrode (MF-2014; BASi, Lafayette, USA). The speed of approach used was 1 μm s^{-1}.

The electrochemical behavior of Hg hemispherical UMEs was characterized using cyclic voltammetry in Ruhex from -300 to -900 mV *vs.* Hg/Hg_2SO_4 (Figure 2.7.) at a scan rate of 10 mV s-1. The full surface coverage of the Hg on the active material was characterized using linear sweep voltammetry (from 0 to -2.0 V *vs.* Hg/Hg_2SO_4) in a 0.1 M KNO_3 solution (Figure 2.2.B), whereby the proton reduction overpotential shifted to more negative potentials compared to a bare disk UME. In this case, potentials were recorded relative to a chloride free Hg/Hg_2SO_4 (Sat. K_2SO_4) (REF 601, Radiometer Analytical, Burlington, USA) reference electrode.

2.4. RESULTS AND DISCUSSION

2.4.1. DISK ULTRAMICROELECTRODES CHARACTERIZATION

The fabrication procedure (Figure 2.1) was tested by 10 subjects without any prior electrode fabrication experience whatsoever, yielding consistently high quality UMEs. Total fabrication time for a single UME was less than one hour. However, several steps can be performed concurrently for several UMEs (*e.g.* epoxy curing), allowing for the production of a batch of 30

UMEs during a single day. UMEs were characterized using optical microscopy, cyclic voltammetry, and SECM approach curves. These three complementary techniques evaluate several important parameters including the R_g, quality of the polishing and sealing, and most importantly, the electrochemical behavior of the UME.

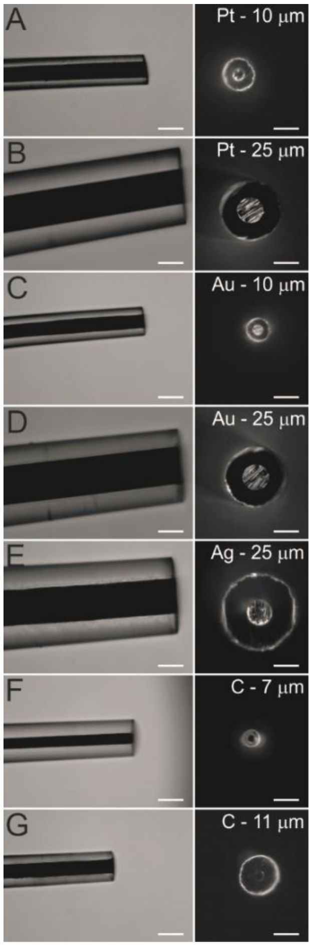

Figure 2.3. Optical micrographs for platinum (A, B), gold (C, D), silver (E), and carbon (F, G) disk UMEs. Side views (left) show well-sealed electroactive cores (absence of air bubbles) with a straight tip. Top views (right) show clean and centered electroactive cores. Scale bars represent 25 µm. Labels indicate the nature of electroactive wire/fiber and the manufacturer's dimensions.

Side view images (Figure 2.3.A-G, left) confirm the absence of air bubbles and a proper concentric seal of the wire/fiber within the insulating glass sheath. The sealed length was 3-5 mm. To avoid capillary bending during sealing, concentric alignment of the UME within the heating coil and coil temperature (heater level 60.0 or 717 °C) were rigorously controlled. Bending effects were more prevalent when using smaller diameter wires. Top view optical micrographs (Figure

2.3.A-G, right) confirm ideal disk geometry with a well-centered electroactive core surrounded by an insulating sheath, requiring no further sharpening step as previously described.

To characterize the electrochemical behavior of the UMEs, cyclic voltammetry was used (Figure 2.4). The steady state current (i_{ss}) is governed by the flux of redox species in solution towards the electrode surface as described by:[22]

$$i_{ss} = k\, n\, F\, r_T\, D\, C^*\, \beta \tag{2.3}$$

Where k is a geometric constant (Disk: k = 4; Hemispherical: k = 2π), n is the number of electrons involved in the reaction, F is the Faraday constant (96 485 C eq^{-1}), r_T is the radius of the electroactive surface, D is the experimental diffusion coefficient of the redox species (D_{FcMeOH} = 7.8 x 10^{-6} cm^2 s^{-1} D_{Ruhex} = 8.7 x 10^{-6} cm^2 s^{-1}), C* is the concentration of dissolved redox species and β is a tabulated factor dependent on the R_g of the UME. Using this equation and the experimental i_{ss} of the CVs (see Table 2.1.), the diameters of the electroactive surface of the UMEs were calculated, as reported above the corresponding CVs in Figure 2.4. The calculated diameters are consistent with those observed in optical micrographs (Figure 2.3.A-G) and reported by the manufacturer, confirming a high quality seal devoid of leaks and cracks, which would have manifested as an increased steady state current. This seal quality is further confirmed by the presence of a long current plateau over hundreds of mV. The lack of significant hysteresis in the CVs is also qualitatively indicative of a good polishing.

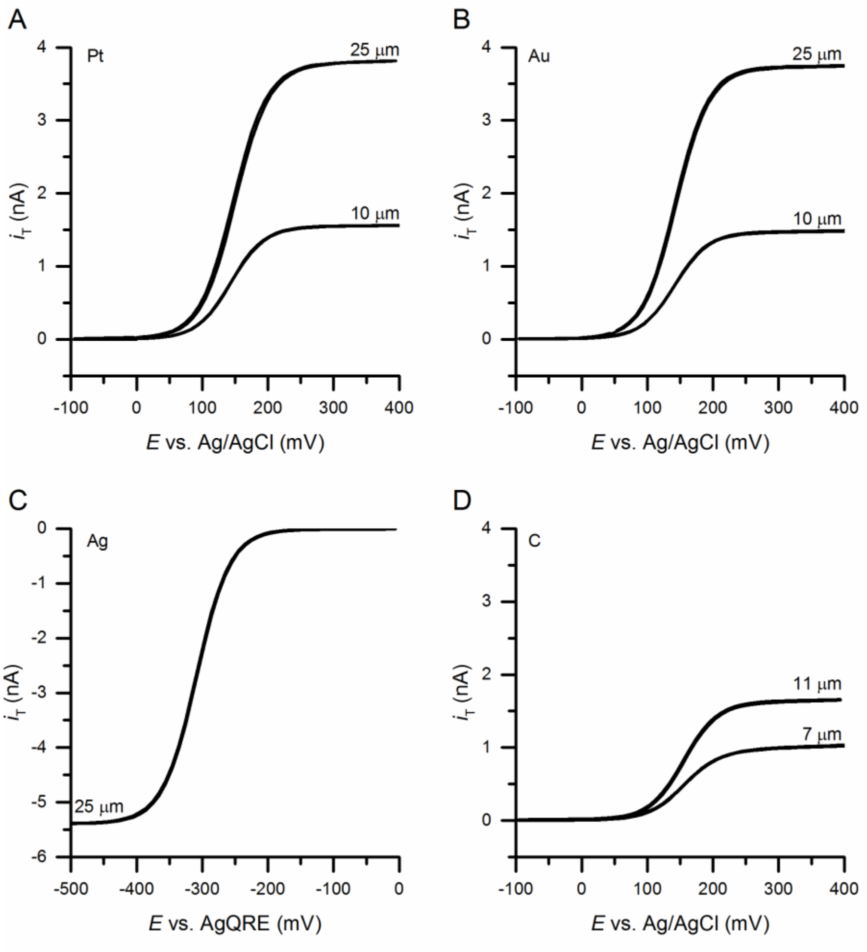

Figure 2.4. CVs for (A) platinum, (B) gold, (C) silver, and (D) carbon disk UMEs of various sizes. (A, B, D) were performed using 1 mM FcMeOH in 0.1 M KCl with an Ag/AgCl reference electrode, and (C) was performed using 1 mM Ruhex in 0.1 M KNO_3 with an AgQRE. All scans were performed at 10 mV sec^{-1}.

Table 2.1 – *R_g of Experimental Disk UMEs*

Electroactive Surface	Electroactive Surface Diameter (µm)	R_g	Steady-State Current (nA)	n
Carbon	7	3.2 ± 0.1	1.07 ± 0.003	4
	11	2.5 ± 0.1	1.64 ± 0.02	3
Gold	10	3.2 ± 0.2	1.51 ± 0.02	4
	25	2.7 ± 0.1	3.78 ± 0.04	5
Platinum	10	3.6 ± 0.1	1.51 ± 0.02	5
	25	2.7 ± 0.1	3.70 ± 0.05	5
Silver	25	2.7 ± 0.2	-4.47 ± 0.21	4
Average:	-	3.0 ± 0.2	-	30

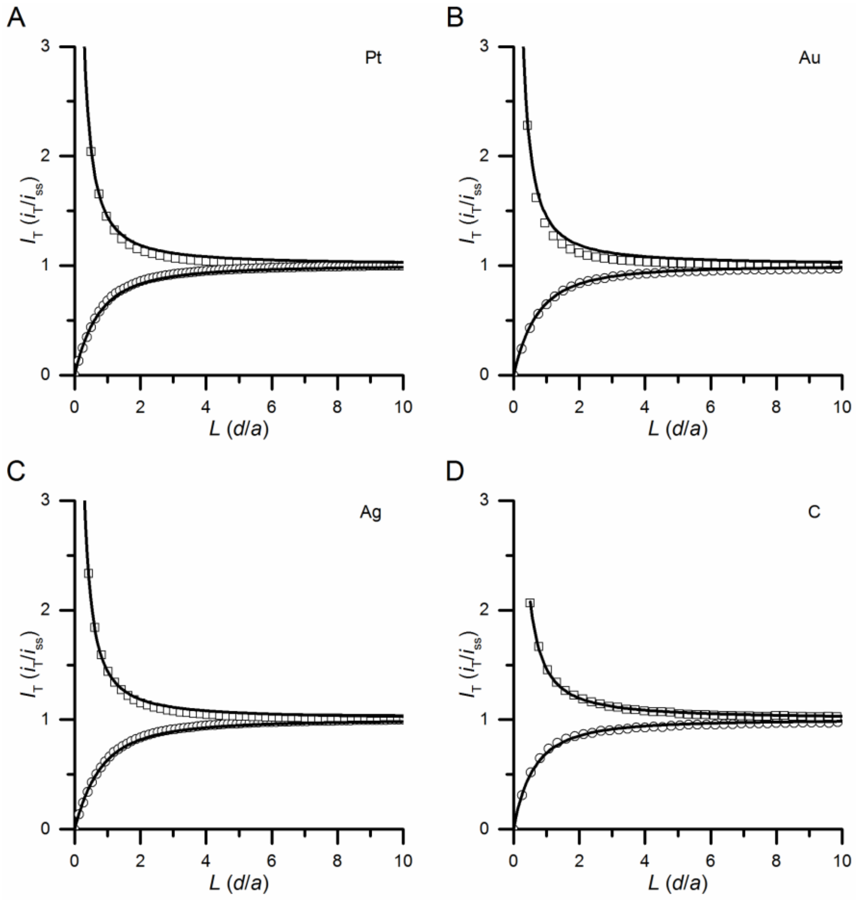

Figure 2.5. Negative (○) and positive (□) feedback approach curves for (A) platinum, (B) gold, (C) silver, and (D) carbon disk UMEs. Solid lines correspond to theoretical values obtained from an analytical expression. (A, B, D) were performed using 1 mM FcMeOH in 0.1 M KCl with an Ag/AgCl reference electrode, and (C) was performed using 1 mM Ruhex in 0.1 M KNO_3 with an AgQRE. UMEs were approached at a speed of 1 μm s^{-1}.

SECM approach curves were used to determine R_g. UMEs were approached towards an insulating or conducting surface whilst biased at a constant potential, producing negative and positive feedback currents, respectively (Figure 2.5). The R_g can be determined by fitting the experimental approach curves to theoretical expressions for current over an insulator or conductor.[22] The R_g of fabricated disk UMEs were tabulated in Table 2.1. Using the proposed technique, UMEs with small R_g are readily achievable. Moreover, the results in Table 2.1. indicate that the geometry of the fabricated UMEs is reproducible across electrode materials, with an average $R_g = 3.0 \pm 0.2$ (n = 30). The data is presented as mean ± standard error of the mean (S.E.M). The number of data points is defined as *n*. In comparison to a non-exhaustive compilation of commercially available SECM-grade disk UMEs (Appendix A Table A.1.), with only one exception, the R_g of commercial disk UMEs are much larger than the ones reported in Table 2.1.

2.4.2. MERCURY DISK AND HEMISPHERICAL ULTRAMICROELECTRODES CHARACTERIZATION

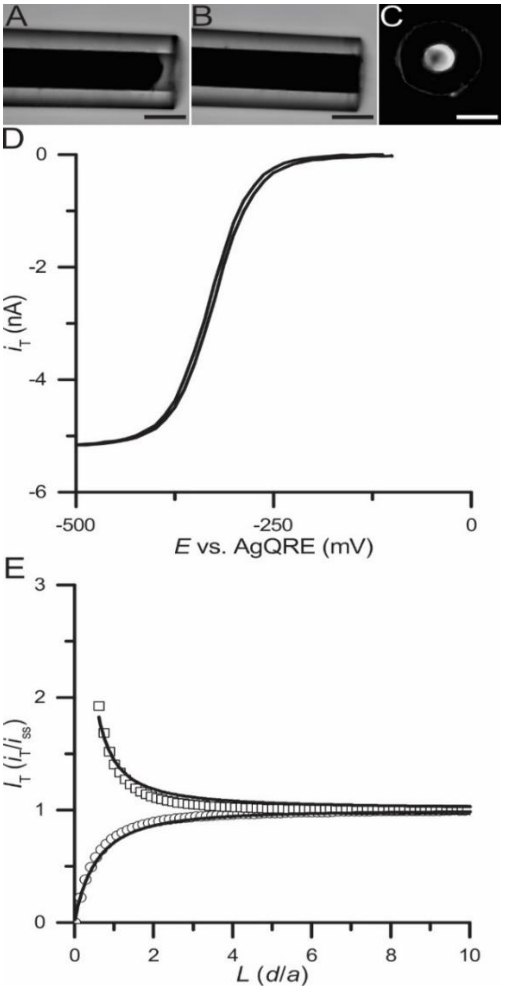

Figure 2.6. Characterization of Hg disk UMEs (A) Side view optical micrograph of a recessed 25 µm Au disk UME following etching in aqua regia solution. (B) Side view optical micrograph of a Hg disk UME formed after electrodeposition and mechanical polishing. (C) Top view optical micrograph of a Hg disk UME. (D) CV of a Hg disk UME. (E) Negative (○) and positive (□) feedback approach curves for a Hg disk UME performed using Ruhex at a speed of 1 µm s^{-1}. Solid lines correspond to theoretical values obtained from an analytical expression. Scale bars represent 25 µm.

Hg disk UMEs were fabricated using a combination of chemical etching, electrodeposition, and mechanical polishing. Optical micrographs were obtained at different stages of the fabrication process. The side view image (Figure 2.6.A) highlights a chemically recessed Au UME. Etching depth can be adjusted by controlling the immersion time in aqua regia. Since the bare disk UMEs used during this fabrication process were previously characterized, it was determined that the diameter of the produced gap was equal to the diameter of the electroactive core i.e. using a 25 µm Au disk UME, the diameter of the gap was also 25 µm. Following Hg electrodeposition and mechanical polishing, the side (Figure 2.6.B) and top view (Figure 2.6.C) optical micrographs confirm the disk geometry of the Hg UME. The top view (Figure 2.6.C) also demonstrates that the Hg electroactive area is well centered within the glass sheath. Following fabrication, Hg disk UMEs were characterized using CV (Figure 2.6.D) and SECM approach curves (Figure 2.6.E). Again, using equation 2.3 and the i_{ss} from the CV (Figure 2.6.D), the diameter of the Hg disk UME was 25 µm, which is consistent with the diameter of the recessed Au wire backbone. The positive and negative feedback approach curves (Figure 2.6.E) were fitted to theoretical expressions. The behavior of the Hg disk UME was equivalent to its Au disk UME backbone, with the same R_g. The complete surface coverage of the Hg on the recessed gold surface was demonstrated using linear sweep voltammetry (Figure 2.2.B), whereby a 650 mV overpotential cathodic shift in the proton reduction current is observed at the Hg UME as compared to the recessed disk UME.[24] The development of Hg disk UMEs allows for an extended solvent window in the negative potential region, which is not possible with conventional cores such as Au or Pt, and also offers an increase of sensitivity compared to other metals for the electroanalysis of trace metal.[25, 26] Moreover the disk geometry allows fitting to established theoretical expressions.

The method can also produce Hg hemispherical UMEs. Hg hemispheres were grown onto disk UMEs using electrodeposition and evaluated by optical microscopy. Side view optical micrographs (Figure 2.7 insets) confirmed full surface coverage of the Hg hemisphere on the electroactive core (Ag, Au, C, or Pt) without expansion to the glass sheath (i.e. not overgrown) and determined that Hg hemispheres were properly tethered. The response of hemispherical Hg UMEs made with different electroactive cores was also evaluated using cyclic voltammetry, as shown in Figure 2.7. As expected, steady-state currents were larger for hemispherical Hg UMEs compared to bare disk UMEs. This behavior was the result of the change in geometry from disk to hemispherical, which according to equation 2.3 results in a steady-state increase of π/2 ($i_{ss,\text{ hemisphere}}$ / $i_{ss,\text{ disk}}$ = 2π/4 = 1.57). The well-defined geometry of the disk UMEs used as a backbone allowed relatively simple modification of their electroactive surface and produced hemispherical UMEs with an equally well-defined geometry, which makes them highly suitable for SECM measurements.

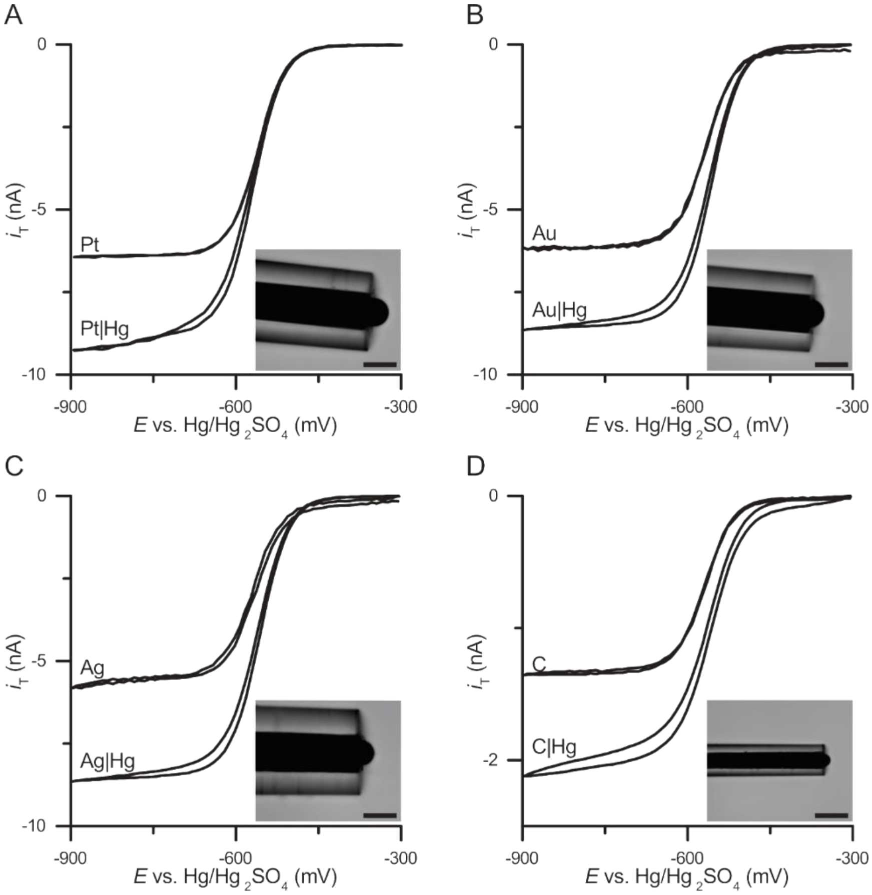

Figure 2.7. Steady-state voltammograms recorded in 1 mM Ruhex in 0.1 M KNO$_3$ for the bare disk electroactive surface and for the Hg hemisphere deposited on the surface. Inset are the side view optical micrographs of the Hg hemispherical UMEs. Scale bars represent 25 µm. (A) 25 µm Pt disk UME and Hg/Pt UME. (B) 25 µm Au disk UME and Hg/Au UME. (C) 25 µm Ag disk UME and Hg/Ag UME. (D) 11 µm C disk UME and Hg/C UME.

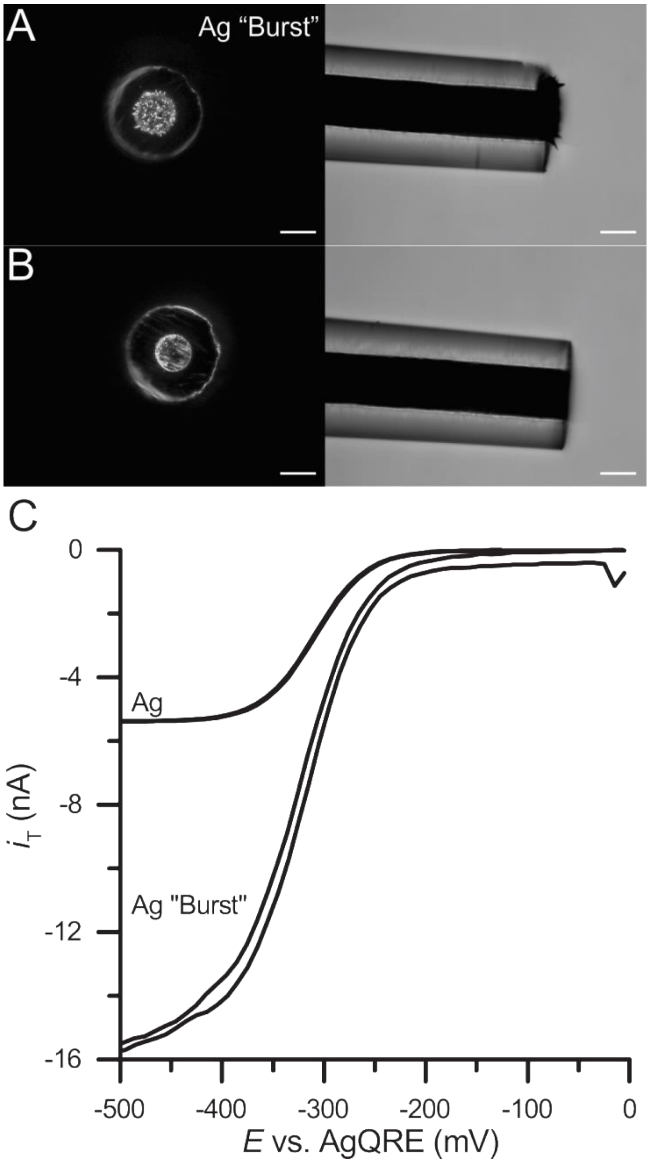

Figure 2.8. Assessment of Ag disk UMEs. (A) Top and side view optical micrographs of a burst 25 µm silver UME. (B) The same UME after a quick repolish to produce a flat surface. Scale bars represent 25 µm. (C) Steady-state voltammograms for both the burst and the repolished 25 µm Ag disk UME. An increase of the i_{ss} can be observed for the burst CV, attributed to the increase of surface area.

A particular challenge was encountered during the fabrication of silver disk UMEs. Among the noble metals used, silver has the lowest melting point, which means it is also the softest. Sealing glass around the silver wire was not a problem but polishing the UME tip proved to be more difficult than other electroactive cores. Typically, the tip is polished until the electroactive surface is exposed. In the described protocol, this is done using a speed of 400 rpm for approximately 15 min. Electrochemical characterization using CV showed that the fabricated silver disk UMEs had an electroactive core with a diameter much larger than 25 μm (Figure 2.8.C), which seemed unreasonable considering the inserted wire was only 25 μm. Subsequent optical microscopy imaging showed that the surface of UME was not flat, resembling a "burst effect", whereby the metal seemed to burst out of the capillary (Figure 2.8.A). After repolishing for a short period (~1 min), the surface became clean and flat (Figure 2.8.B), similar to other electroactive cores used. It was determined that in fact, the "burst effect" was caused by polishing for an extended period of time. The friction produced by the speed and time of polishing caused the silver to soften and "burst" out of the glass sheath. This observation highlights the fact that although polishing is an important component of the fabrication process, great care must be taken to ensure proper UME geometry.

Top and side view optical micrographs (Figure 2.9.A-B) show that an AgCl layer has successfully been electrodeposited onto the bare Ag disk UME. In order to evaluate the electrochemical stability of the micro-reference electrodes, cyclic voltammetry in FcMeOH was used. Figure 2.9.C shows CVs obtained with 10 different micro-reference electrodes and the same working electrode (25 μm Pt disk UME). The exhibited electrochemical behavior is consistent with the response obtained from a commercial (and much larger) reference electrode. Even after 100 cycles, electrochemical response remained stable. The experimental E^0 was calculated to be 166.9 ± 2.3 mV (n = 10). The small size of these micro-reference electrodes make them suitable for use in micro-electrochemistry. Furthermore, using a double-barrel soft glass capillary with similar dimensions would allow fabrication of UMEs with an integrated Ag/AgCl micro-reference electrode.

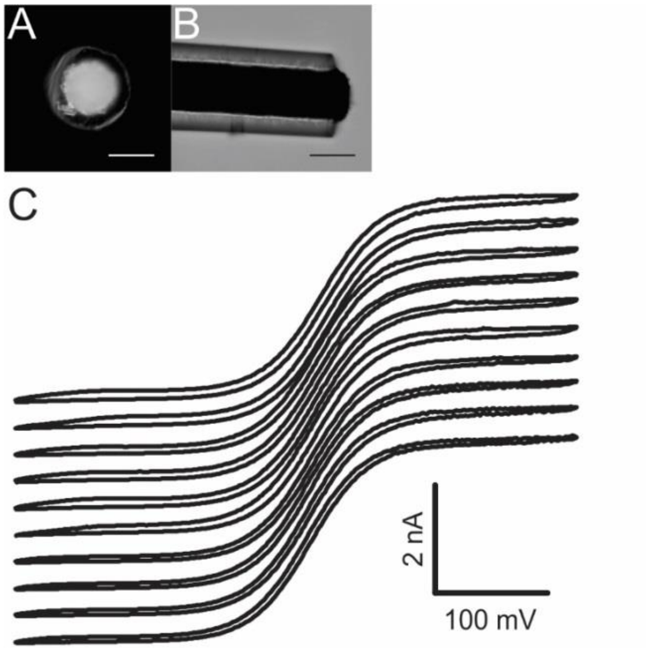

Figure 2.9. (A) Top and (B) side view optical micrograph of a 25 µm Ag/AgCl micro-reference electrode. (C) Steady-state voltammograms recorded using the same working electrode (25 µm Pt UME) and 10 different 25 µm Ag/AgCl micro-reference electrodes in FcMeOH. Scale bars represent 25 µm.

2.5. CONCLUSIONS

We have successfully developed a general technique for the fabrication of disk UMEs with different electroactive cores, including carbon, gold, mercury, platinum, and silver. This technique leads to UMEs with small R_g ranging from 2.5 – 3.6. The main advantages of the proposed fabrication technique include speed and relative ease of fabrication, controlled and reproducible geometry, and the ability to expand to multiple electroactive cores. Furthermore, the disk UMEs produced using this technique make them ideal backbones for surface-modified electrodes, demonstrated here by the production of Hg disk, hemispherical UMEs and Ag/AgCl micro-reference electrodes. Finally, the optimal geometry of theses probe makes them highly suitable for use in SECM measurements.

[1] A.J. Bard, L.R. Faulkner, Electrochemical Methods: Fundamentals and Applications, 2 (1980) 169.

[2] J. Heinze, Angewandte Chemie (International Edition in English), 32 (1993) 1268-1288.

[3] C.G. Zoski, Handbook of electrochemistry, Chapter 6, 2007.

[4] C.G. Zoski, Electroanalysis, 14 (2002) 1041-1051.

[5] L. Danis, M.E. Snowden, U.M. Tefashe, C.N. Heinemann, J. Mauzeroll, Electrochimica Acta, 136 (2014) 121-129.

[6] B.B. Katemann, W. Schuhmann, Electroanalysis, 14 (2002) 22-28.

[7] J. Velmurugan, J.M. Noël, M.V. Mirkin, Chemical Science, 5 (2013) 189-194.

[8] J. Mauzeroll, E.A. Hueske, A.J. Bard, Analytical Chemistry, 75 (2003) 3880-3889.

[9] Y. Takahashi, A.I. Shevchuk, P. Novak, Y. Murakami, H. Shiku, Y.E. Korchev, T. Matsue, Journal of the American Chemical Society, 132 (2010) 10118-10126.

[10] Y. Lee, A.J. Bard, Analytical Chemistry, 74 (2002) 3626-3633.

[11] S.L.R. Harvey, P. Coxon, D. Bates, K.H. Parker, D. O'Hare, Sensors and Actuators, B: Chemical, 129 (2008) 659-665.

[12] P. Liljeroth, C. Johans, C.J. Slevin, B.M. Quinn, K. Kontturi, Electrochemistry Communications, 4 (2002) 67-71.

[13] F.R.F. Fan, M.V. Mirkin, A.J. Bard, Journal of Physical Chemistry, 98 (1994) 1475-1481.

[14] M.V. Mirkin, F.R.F. Fan, A.J. Bard, Journal of Electroanalytical Chemistry, 328 (1992) 47-62.

[15] X. Zhao, P.M. Diakowski, Z. Ding, Analytical Chemistry, 82 (2010) 8371-8373.

[16] S. Kuss, D. Polcari, M. Geissler, D. Brassard, J. Mauzeroll, Proceedings of the National Academy of Sciences of the United States of America, 110 (2013) 9249-9254.

[17] P. Sun, M.V. Mirkin, Analytical Chemistry, 78 (2006) 6526-6534.

[18] A.L. Barker, P.R. Unwin, J. Zhang, Electrochemistry Communications, 3 (2001) 372-378.

[19] U.M. Tefashe, M.E. Snowden, P.D. Ducharme, M. Danaie, G.A. Botton, J. Mauzeroll, Journal of Electroanalytical Chemistry, 720-721 (2014) 121-127.

[20] K. Eckhard, T. Erichsen, M. Stratmann, W. Schuhmann, Chemistry - A European Journal, 14 (2008) 3968-3976.

[21] M. Shen, N. Arroyo-Currás, A.J. Bard, Analytical Chemistry, 83 (2011) 9082-9085.

[22] C. Lefrou, R. Cornut, ChemPhysChem, 11 (2010) 547-556.

[23] M.A. Mezour, M. Morin, J. Mauzeroll, Analytical Chemistry, 83 (2011) 2378-2382.

[24] J. Velmurugan, M.V. Mirkin, ChemPhysChem, 11 (2010) 3011-3017.

[25] D. Rudolph, S. Neuhuber, C. Kranz, M. Taillefert, B. Mizaikoff, Analyst, 129 (2004) 443-448.

[26] C. Wechter, J. Osteryoung, Analytical Chemistry, 61 (1989) 2092-2097.

CHAPTER 3: DEVELOPMENT OF NANO-DISC ELECTRODES FOR APPLICATION AS SHEAR FORCE SENSITIVE ELECTROCHEMICAL PROBES

Smaller UMEs have immense potential to gain knowledge that could not be obtained with larger electrodes. One of the main advantages of decreasing the size of the UMEs is the increased spatial resolution in SECM, for the acquisition of higher resolution scans. Electrodes with smaller critical dimensions bring advantages such as increased mass transport, smaller RC constants, higher sensitivity, faster steady-state voltammetric response, lower double-layer charging currents, smaller ohmic losses and can make measurements in solutions of higher resistance than with larger electrodes. The work presented in Chapter 3 directly relates to an optimized methodology to produce a well-defined Pt disk encapsulated in glass with the electroactive core in the nanometer scale. This chapter also describes the shear force behavior of these nanoelectrodes. Shear force is used in SECM for maintaining a constant tip-to-substrate distance. In comparison with constant height imaging, constant distance imaging brings the ability to separate the substrate topography signal from the electrochemical signal. In Chapter 3, we investigate factors that impact the SF sensitivity (*i.e.* the tip-to-substrate distance, position of the piezo, and probe geometry) in order to enhance the sensitivity the SF signal. A new methodology to determine shear force sensitive frequencies is also explored in this chapter.

The nano-disc electrodes presented in Chapter 3 will serve as a backbone for the development of the nano Hg-based ASV sensors used in Chapters 4 and 5 for the quantitative detection of Mn^{2+} and the evaluation of the Mn^{2+} chelating agents for the LIB application mentioned in earlier chapters.

The work presented in this chapter was originally published and is reprinted (adapted) with permission from:

Danis L., Snowden M.E., Tefashe U. M., Heinemann C. N., Mauzeroll J., *Development of Nano-Disc electrodes for Application as Shear Force Sensitive Electrochemical Probes*. Electrochimica Acta. 2014, 136, 121-129. Copyright © 2014, Elsevier

3.1. ABSTRACT

Maintaining a well-defined tip-to-substrate separation is a critical area of development in SECM. One technique that provides topographic data independently to the electrochemical measurement is SF-SECM. SF measurements are highly sensitive to factors including the tip-to-substrate separation, experimental solution, and probe geometry. We present a procedure for the fabrication of highly reproducible electrochemical probes with an active electrode disc with radii between 3 nm to 190 nm. A systematic study of the SF characteristics of these nanoelectrodes provides details on how to achieve the highest sensitivity and stability of SF signals, and maximize the number of SF sensitive frequencies. A new methodology to identify SF sensitive frequencies without needing to immerse the probes in solution or approach the surface is presented. Furthermore, we demonstrate that the greatest source of error in achieving reproducible SF behavior lies in the positioning of the piezo electric components and the piezo-nanoelectrode interface.

3.2. INTRODUCTION

SECM is a well-established electroanalytical method for the characterization of substrate surfaces.[1] This method has been applied to several analytically relevant fields including bioelectrochemistry,[2, 3] corrosion studies,[4] charge transport at liquid/liquid interfaces[5-7] and microfabrication.[8] In conventional SECM, a “constant height” mode is used, where, under ideal experimental conditions, the UME is moved parallel to the substrate (*x*,*y* plane) with no vertical motion (*z* axis) of the UME. In this case, the UME signal depends on the local topography and electrochemical reactivity of the substrate.[9]

To decouple the current contribution of topography from surface reactivity several methodologies have been proposed. For example by using impedance[10, 11] or alternating current signals,[2] the topographic and surface reactivity can be determined by post-processing of the data. Alternatively, a dual electrode probe where one UME monitored a surface independent reaction to determine the topography (*e.g.* the reduction of oxygen), whilst the second UME monitored the substrate sensitive reactant has been reported.[12] The physical interaction between the tip and substrate can be used in hybrid SECM systems,[13-15] for example, tip-position modulation (TPM) algorithms,[16] intermittent-contact mode (IC),[17] voltage switching mode (VSM)[18] and SF detection which rely on the reduced damping of a vertically or laterally vibrated probe in close proximity to the substrate.[19-21]

SF force distance controlled SECM is used routinely by several electrochemistry laboratories to report the topography of a variety of surfaces, including live cells,[22, 23] large and complex metal samples,[24] or to monitor local activities of ions in proximity of a solid/liquid interface.[25] The method employs a feedback signal based on changes of SF tip to substrate interactions to maintain a constant probe-substrate separation. These SF interactions may be attributed to hydrodynamics forces, van der waals interactions, direct mechanical contact and capillary forces.[26] Several types of SF methodologies have been reported in the literature.[19, 27, 28]

Typically, the SF method involves a UME fastened to two piezoelectric plates: dither and receiver.[19] The dither piezoelectric plate induces a sinusoidal lateral mechanical oscillation of the UME, and a receiver plate detects the oscillation. When the UME is in close proximity to the surface, the lateral oscillation is damped due to SF interactions between the tip and the surface of the sample. As the UME is scanned laterally, a constant tip-to-substrate separation can be achieved by adjusting the z position of the probe to maintain constant SF amplitude. Simultaneously, the height profile (or the topographic variation) of the surface can be constructed from the z motion of the probe. Early design for SF constant distance imaging suggested a constant separation mode in which the tip was maintained within the SF sensitive zone throughout all of the measurement.[19]

Our system is equipped with a hopping or picking mode[29] SF amplitude controlled unit analogous to what has been described in recent work from Schuhmann.[28] This mode tends to minimize the contact between the tip and the surface by retracting the tip and performing a SF z-approach curve at each position on the x-y axes grid. When operating under conditions where the tip and substrate are not in contact, SF-SECM can be applied to substrates that are easily deformed without compromising the electrochemical and topographic data, such as a living cell. Hopping mode can also result in a faster measurement for samples with large topographical variations where the SF signal would be lost in constant distance mode.[28] The SF sensitive region is thought to extend to a few hundred nanometers above the surface,[30] depending on the nature of substrate surface, the viscosity of the liquid, and the tip size, physical properties and geometry.[25, 26, 30]

UMEs with a small tip diameter or a small R_g exhibit shorter length of the SF signal which is very interesting for SECM imaging as it allows the measurement to be performed at a very short tip to substrate distance.[30] Pulled microelectrodes with long tapers producing flexibility reportedly exhibit improved vibrational characteristics, which implies an increased number of shear force sensitive resonance peaks.[9, 31] Quartz encapsulated Pt nanoelectrodes display enhanced oscillation features.[27, 32] Laser-pulled Pt/quartz disk UMEs, which possess a small diameter and long flexible taper, are suitable for SF experiments. In addition to the UME, instrumental and experimental factors are thought to affect the SF response; these include the piezo-UME interface, the choice of SF sensitive frequencies, the viscosity of the liquid or gas, surface properties of the substrate, and the probe immersion depth.[25, 26]

Herein, we report a method for fabricating nano-disc Pt electrodes and the subsequent parametric optimization which provided a highly reproducible, sensitive and stable SF response for frequencies in the range of 350–550 kHz. The identification and selection of these stable SF sensitive frequencies was key to providing high stability for constant distance measurements. Furthermore, we present a fast diagnostic method that was performed entirely off sample in order to rapidly identify SF sensitive frequencies. This methodology removes the need for frequency analysis of the SF signal with the UME in contact with the substrate, significantly reducing the risk of damaging the electrode tip and the substrate during measurements.

3.3. EXPERIMENTAL

3.3.1. PREPARATION AND CHARACTERIZATION OF NANOELECTRODE PROBES

The nanoelectrodes were fabricated using a P-2000 laser-based micropipette puller system (Sutter Instrument Company, USA) according to a previously published procedure.[33-36] The quartz capillaries (L.: 10 cm; O.D.:1.0 mm; I.D.:0.50 mm; Sutter Instrument, USA) were cleaned using (10 % v/v, Caledon Laboratories Ltd.) nitric acid solution, rinsed with water purified using Milli-Q Reference system (resistivity 18.2 MΩ cm) (Millipore), and dried in an oven (100 °C) for 12 h. A 1 cm long 0.025 mm diameter Pt-Wire (purity 99.99 %; temper hard; Goodfellow, England) was cleaned with acetone, straightened and electrically connected with conductive silver epoxy (EPO-TEK H20E; Epoxy Technology, USA) to a 0.3 mm diameter standard copper wire and inserted centrally in a quartz capillary. The assembly was then inserted in the laser-puller (Figure 3.1.A). A vacuum pump (Edwards RV8, Edwards, Canada) was attached to each end of the capillary and applied reduced pressure for 30 min to remove air and trace solvent that could compromise the Pt/glass seal. During the sealing step, no pull force was applied to the pipet and ensured by the presence of stoppers added to the puller bars of the puller. To seal quartz around the Pt wire, a single line heating program (Heat: 685, Filament: 005, Velocity: 060, Delay: 140, Pull: 000) was then applied five times in a cycle of 40 s of heating followed by a 20 s of cooling time. Following sealing (Figure 3.1.B), the stoppers and vacuum connections were removed. The final hard pull (Figure 3.1.C) was then performed (Heat: 780, Filament: 002, Velocity: 060, Delay: 140, Pull: 200). This procedure resulted in the production of two nearly identical UMEs. Internal electrical connections were then done using silver epoxy. The UMEs were reinforced and sealed using 5 min epoxy with a larger borosilicate capillary (L.: 7.5 cm; O.D.: 2.0 mm; I.D.: 1.16 mm; Sutter Instrument, USA) to provide more stability or robustness to the electrode and to obtain a better fit to the SECM platform (Figure 3.1.D). A gold electrode connector pin (HEKA Instruments Inc., USA) was connected to the copper wire. The UMEs were then polished to expose the metal surface using a variable speed polisher (Tegrapol 23, Struers, Canada) spinning at 400 rpm on 4000 grit abrasive discs (4000 grit, Struers, Canada) followed by an alumina powder polishing (0.05, 0.1, 0.3, 1.0 μm particle diameter).

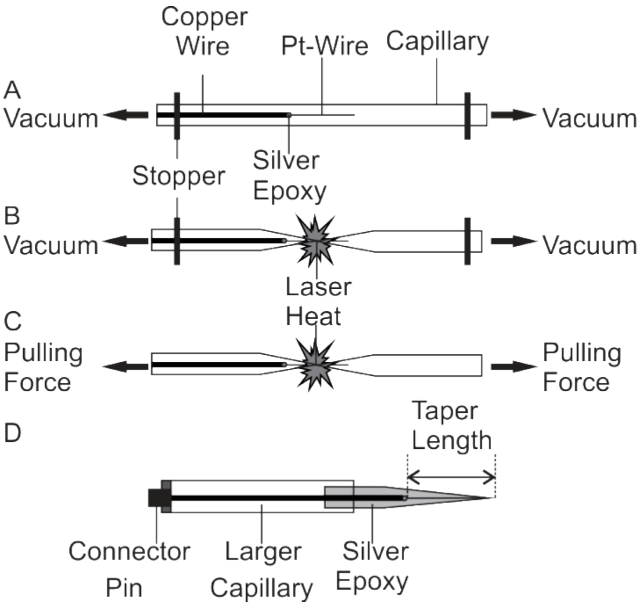

Figure 3.1. Optimization of UME fabrication procedure (A) Pt wire was inserted into the quartz capillary and (B) the quartz capillary was sealed around the Pt wire using a P-2000 Laser Based Micropipette Puller. (C) A pulling force was applied to produce reproducible tapered UME tips. (D) The UME was reinforced with the larger capillary and the electrical connection was made.

The quality of the polishing, the radius of the electroactive surface, the platinum-glass seal and the electrochemical behavior of the UME were characterized using cyclic voltammetry in an aqueous solution of 1 mM FcMeOH ($FcCH_2OH$ 97 %, Sigma Aldrich, Canada) and 0.1 M potassium chloride (KCl, Fisher Scientific, USA) by linearly sweeping the potential from -100 to 450 mV at a scan rate of 10 $mV.s^{-1}$. The radius of the glass was determined by negative and positive feedback approach curves over an insulating CTFE plastic puck and over a well-polished gold disk 1.6 mm (macroelectrode MF-2014 (BASi)), respectively. The speed of approach varied from 0.1 to 1 µm s^{-1} depending on the diameter of the UME. The counter electrode was a platinum wire. Potentials were recorded relative to a chloridized silver wire (in house) quasi-reference electrode.

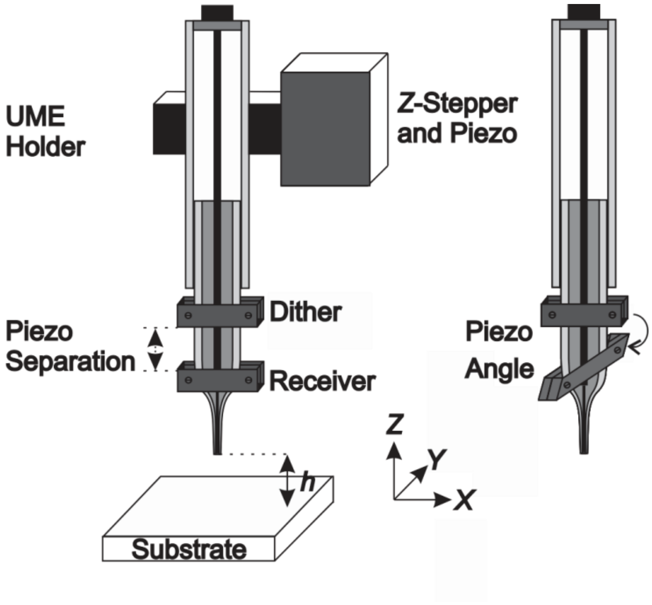

Figure 3.2. Scheme of the holder by which the piezos are mechanically mounted to the capillary using four screws (2 screws per piezo). The holder is attached to the Z-stepper motor of the SECM setup.

3.3.2. SHEAR FORCE - SCANNING ELECTROCHEMICAL MICROSCOPY SETUP

SECM measurements were performed using an ElProScan 3 system (ELP 3), with POTMASTER software (version v2x66) and the ElProScan Controller ESC 3 equipped with a SF unit, SFU 3 (HEKA Elektronik, Germany). The two piezo electric plates (PIC 255, PI Ceramic GmbH, Germany) were mounted on the UME using four screws (2 screws per piezo) as shown in Figure 3.2. A frequency scan range from 10 kHz to 1 MHz was performed to identify SF sensitive peaks. A stimulation amplitude of 1 mV to 10 V was applied. The duration of a frequency scan depended the number of samples recorded.

3.3.3. SHEAR FORCE - SCANNING ELECTROCHEMICAL MICROSCOPY MEASUREMENTS

The substrate surface for the SECM mapping was prepared by first cutting a blank gold CD-R (Staples, recordable disks 4.7GB) into 1 cm x 1 cm chips. The CD-R was immersed in a mixture of concentrated nitric acid and sulfuric acid solution for 1 min to selectively etch the CD-R. The etching process removed the metallic layer of rewritable CD (Au) from the raised sections (plateaus) whilst leaving the metallic layer exposed within the trenches. Therefore the plateaus were not electrochemically active and the trenches were electrochemically active. The treated CD-R was then washed with water, dried under nitrogen. SF-SECM maps were performed in a solution containing 3.5 mM FcMeOH/0.1 M KCl (100 µL anhydrous ethyl alcohol (Commercial Alcohols, Brampton, Canada) made to 25 mL volume in water).

3.4. RESULTS AND DISCUSSION

3.4.1. OPTIMIZATION OF ULTRAMICROELECTRODE FABRICATION PROCEDURE

UMEs were characterized by scanning electron microscopy (SEM), cyclic voltammetry and approach curves in both positive and negative feedback modes (Figure 3.3.). The optimization of the UME fabrication procedure has allowed the development of a reproducible technique leading to disk UMEs with long and flexible tapers ranging from 0.7 to 1.5 cm. The radius of the electroactive surfaces ranged from 3 nm to 190 nm. SEM images (Figure 3.3.B) confirmed the fabrication of a sealed concentric disk shaped UME.

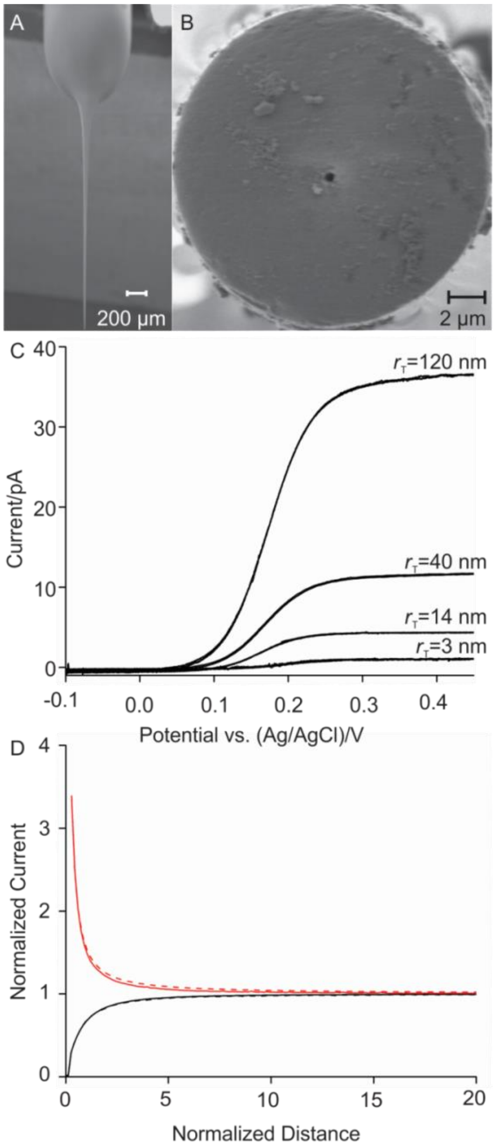

Figure 3.3. Scanning electron micrographs of the nanoelectrode tip from a side view (A) and viewed perpendicular to the electrode (B). (C) CVs of 4 UMEs with different electroactive radii in 1 mM FcMeOH in 0.1 M KCl recorded at a scan rate of 10 mV s^{-1}. (D) Solid lines are experimental approach curves for negative (black) and positive (red) feedback (solid). The dashed lines represent the theoretical response for the experimental probes. Best-fit parameters r_T = 190 nm and R_g = 23.4.[37, 38] The UMEs used for (C) and (D) are not the same probes as reported in (A) and (B).

The 4 CVs performed at a scan rate of 10 mV s^{-1} (Figure 3.3.C) display a sigmoidal shape and achieve diffusion-limited steady-state currents for the oxidation of FcMeOH when a potential of 300 mV (or greater) *vs.* Ag/AgCl was applied. Under diffusion control, the i_{ss} is given by Equation 2.3, presented in Chapter 2. [39,40]

For a set of 30 UMEs, the r_T ranged between 3 to 190 nm. The R_g was evaluated using SECM approach curves in feedback mode (Figure 3.3.D). For the feedback mode approach curve measurements, the UME was set at a potential of 450 mV *vs.* Ag/AgCl to ensure the complete oxidation of FcMeOH to $FcMeOH^+$ at the electrode surface. The approach curve was measured over both an insulating CTFE substrate (negative feedback) and a clean gold electrode (positive feedback). The R_g value have been extracted from fitting the experimental approach curves to the analytical approximation that describe the hindered diffusion near a surface [37, 41] and the positive feedback approach curves.[38] For the same set of 30 UMEs the R_g value ranged from 5 to 25 with a good consistency between R_g extracted from the negative and the positive feedback. In order to reduce the R_g value we used glass capillaries with a smaller outer diameter/inner diameter ratio compared to the literature.[36] UMEs with smaller R_g values have been reported using a similar fabrication technique with a pre-thinning step.[35] The previously explained fabrication protocol has comparable success rate to the other techniques. However, they exhibit higher resolution in SECM as the size of the electroactive surface is considerably smaller. Furthermore, the Pt nanoelectrodes presented here have significantly longer and more flexible tapers which is required for oscillation.[9, 31]

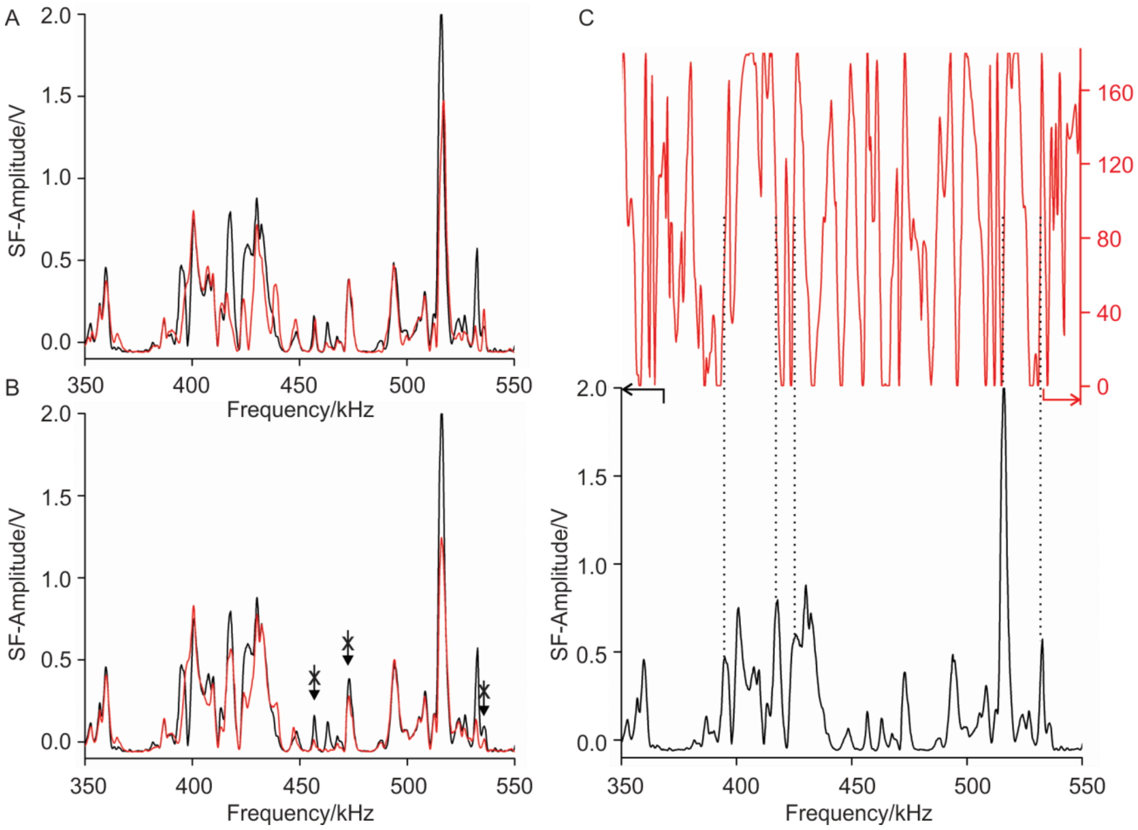

Figure 3.4. SF spectra recorded whilst driving the dither piezo with a sine wave frequency between 350 kHz to 550 kHz and an amplitude of 1 V. The spectra reported in Figure 3.4. were all performed with the same UME, without dismounting the piezoelectric plates from the UME or the UME from the stage. Determination of the shear force distance-dependent frequencies and phase behavior. Shear force spectra recorded from 350 to 550 kHz for (A) recorded above the surface (black line) and on the surface (red line), and for (B) recorded in air above the surface (black line) and in aqueous solution above the surface (red line). The arrows marked with an X represent false positives. (C) Phase selective SF characterization method, the phase is represented by the (red) solid line and the amplitude by the (black) solid line. The dashed lines emphasise the phase relationship at distance-dependent SF frequencies.

The first step in a SF experiment involves the selection of a SF sensitive frequency, as not all frequencies are SF sensitive. We have described a more accurate and safer method to distinguish between sensitive and non-sensitive frequencies. There are three different ways to determine tip-to-substrate separation sensitive frequencies which we all be discussed (including our new method) *vide infra*.

SF spectra recorded whilst driving the dither piezo with a sine wave frequency between 350 kHz to 550 kHz and an amplitude of 1 V. The spectra reported in Figure 3.4. were all performed with the same UME, without dismounting the piezoelectric plates from the UME or the UME from the stage.

The first approach (Figure 3.4.A) involves the acquisition of two complete SF spectra whereupon one is recorded whilst the tip was above surface (distance greater than 1 µm) and a second spectrum whilst the tip was in contact with the surface (distance 0 µm). The SF spectrum recorded with the tip in contact with the surface was subtracted from the spectrum recorded when the tip was above the surface to obtain a differential spectrum. From the differential spectrum, the frequencies at which the tip oscillation is damped, or amplified, as the tip moved closer to the surface are ascribed as SF sensitive.[25] Appendix B Figure B.1.A is the difference spectrum and was constructed by subtracting the amplitude of the spectrum recorded on surface from the spectrum recorded above surface. In general, a more stable SF response was obtained at frequencies with a large amplitude and narrow peak width with the attenuation of the peak amplitude when the UME is close to the substrate. The amplitude in a SF experiment was expressed as the magnitude of dither oscillation measured at the receiver (V).

The second method consisted of obtaining a differential spectrum from a SF spectrum recorded above the surface with the probe immersed in a liquid medium from one recorded above the surface in air, this technique has been described by Schuhmann (Figure 3.4.B).[19] The spectrum in appendix B Figure B.1.B was obtained by the subtraction of the amplitude of the spectrum recorded in liquid and from the spectrum recorded in air. Again, from the differential spectrum, the frequencies at which the SF-amplitude (V) show a discrepancy as the tip moved closer to the surface are ascribed as SF sensitive.

From our parametric optimisation, a third empirical method can be used to identify the SF sensitive frequencies by performing a single frequency spectrum measurement with the tip positioned above the surface (Figure 3.4.C). In the above surface SF spectrum there was a very steep decrease in the phase (*i.e.* a drastic shift from 180 to 0 °) at every shear force sensitive frequency. These large changes in phase correspond to the frequencies with the greatest difference in amplitude when the tip to substrate distance was reduced. The maximum amplitude of these peaks occurred at a phase shift of 90°. Appendix B Figure B.1.C and D show an enlargement of the frequency spectrum and phase reported in Figure 3.4.C for the shear force sensitive peak at 417.5 kHz and the non-sensitive peak at 360 kHz respectively. The phase shift (θ) refers to the difference in phase between the sinusoidal input to the dither piezo and the oscillation measured at the receiver piezo. By using this methodology, it was possible to predict the sensitive frequencies without the probe coming into contact with the substrate and whilst using the probe only in air.

The three methods are in agreement with each other and provide the same relevant frequencies for each electrode. The contact / non-contact sensitivity experiments result in the detection of sensitive SF frequencies with no false positives, however, the initial blind approach to the substrate might result in the tip crashing on the surface resulting in possible damage of the tip and/or the substrate. The second procedure involving the acquisition of spectra while the tip was immersed in solution was also possible with our tips, however, this technique often provided false positives on SF sensitive frequencies as shown in Figure 3.4.B at 460 kHz. A false positive can be defined as a frequency where the peak shows a difference in amplitude between the above liquid and in liquid spectra but does not change in the above surface and on surface spectra. The arrows marked with an X in the appendix B Figure B.1.B denote frequencies at which a false positive occurs. In this appendix figure an absent amplifying shear-force sensitive frequency is also highlighted. Selecting a false positive on SF sensitive frequencies can result in the UME crashing into the surface.

The phase selective SF characterization method presented here involved a single measurement recorded in air, which provided no false positives and removed the risk of crashing the tip and the need to immerse the tip in solution. As the SF spectrum strongly depends on the physical properties of the probes and on external factors such as the stimulation amplitude, the viscosity of the liquid, the angle and distance between dither and receiver (piezos) and the screw tightness of dither and receiver (piezo), it is difficult to predict characteristic frequencies prior to obtaining a frequency spectra (*vide-infra*). However, the application the UME fabrication protocol outlined above reproducibly yields electrodes which exhibit a consistent SF sensitive region between 350 kHz and 550 kHz with SF sensitive frequencies which can be determined by the three techniques outlined above.

3.4.3. CHARACTERISTIC MEASUREMENT OF A SHEAR FORCE CALIBRATION CURVE (PULL BACK CURVE)

A frequency spectrum with the tip positioned away from the substrate in air was performed and SF sensitive frequencies were identified by the phase selective SF characterization method (empirical method 3). All, frequency candidates presented stable off surface amplitudes and phase values (root mean square (RMS) signal variation of roughly 1 %). The electrode was lowered towards the surface whilst the SF amplitude was measured.

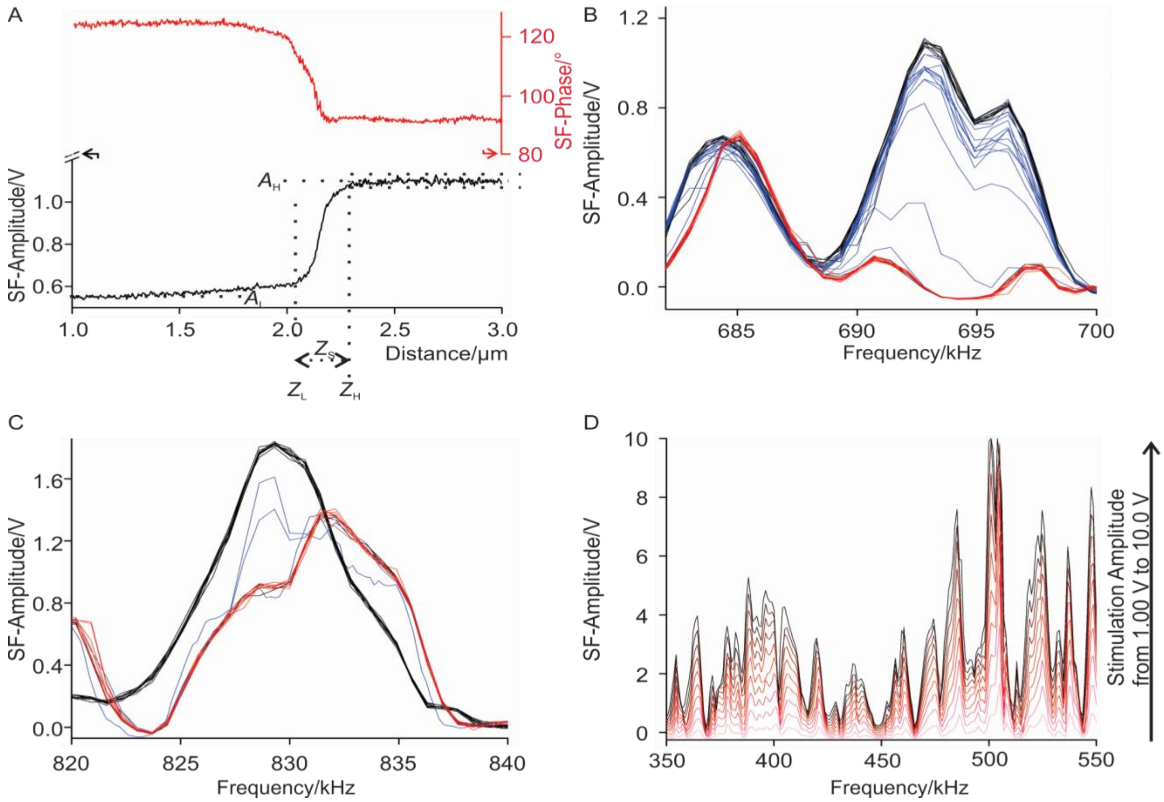

Figure 3.5. (A) Shear force calibration curve (pull back curve) recorded at 451.0 kHz with a stimulation amplitude of 1.00 V. Frequency spectra recorded during a SF approach for (B) a tip with two SF sensitive peaks that decrease in amplitude with tip to substrate and (C) a tip with peaks that increase and decrease in SF amplitude with tip to substrate separation. Black data was with the tip off surface; blue data was at an intermediate distance; and red data was for the tip on surface. (D) The increase in SF amplitude magnitude with respect to the increase of stimulation amplitude with the UME tip positioned on the surface.

Figure 3.5.A shows the change in SF amplitude recorded, when the tip is retracted from the surface, with respect to tip-to-substrate separation at a SF sensitive frequency (in this case 451 kHz

with a stimulation amplitude of 1.00 V). The SF amplitude was constant when the tip was on the surface (where Z_L represents the absolute value where the tip is on the substrate surface). When the tip is in the SF sense length regime (Z_S) the SF amplitude increases with the tip-to-substrate separation before reaching a constant SF amplitude at a tip-to-substrate separation represented by Z_H (Figure 3.5.A). High reproducibility over multiple approach curves were observed (see Appendix B Figure B.2.B) demonstrating that the nanoelectrode tip is not damaged during the approach curve measurements. The stability of the electrochemical response upon successive approaches was demonstrated by cyclic voltammetry (Appendix B Figure B.2.A).

We assessed the quality of the probe at the chosen frequency by evaluation of the approach curve (Figure 3.5.A). Here we define the quality of the probe with respect to the signal to noise ratio (Q_F) and the SF sense length of the probe to assess the selected SF frequency and the vibrational characteristics of the tip and reproducibility of the SF response of multiple probes. We define Q_F as

$$Q_F = \frac{(A_H - A_L)}{A_{SD}} \tag{3.1}$$

where A_H, and A_L are the maximum response amplitude and the minimum response amplitude respectively, and A_{SD} is the standard deviation of signal due to background noise of the measurement (Figure 3.5.A). It is important to note that A_{SD} is constant throughout the approach curve measurements.

The maximum response amplitude, for SF sensitive frequencies, was described as the mean magnitude measured at the receiver (V) while the tip is away from the surface. The maximum response of a SF pull back curve depends on the magnitude of the input signal with higher dither input signals providing higher receiver signals (*vide infra*). The minimum response amplitude was described as the mean magnitude of oscillation at the receiver piezo (V) while the tip was touching the surface. Therefore, the Q_F provides an analytical number to determine if a frequency provides a SF approach curve that has a suitable resolution for a constant distance scan. All 30 probes produced and assessed by this methodology had at least 1 SF sensitive frequency that had a Q_F

greater than 50, demonstrating that the probes produced provide a SF approach response that can be clearly resolved over instrumental noise.

In addition to the Q_F, knowing the z displacement between the maximum and minimum oscillation amplitudes is critical for mapping substrate topography, referred to as the sense length (Z_s). The sense length was defined as the SF sensitive region which can be measured between the on and off surface amplitude. To account for experimental noise the sense length was expressed as the difference between the z-piezo position at A_1 and A_2;

$$A_1 = A_H - 3A_{SD} \tag{3.2}$$

$$A_2 = A_L + 3A_{SD} \tag{3.3}$$

Using the UMEs described above we obtain sense lengths between 25 nm and 465 nm, which is comparable to existing literature values.[31, 42] This wide range can be attributed to the relationship between the sense length and the R_g of the UME. As previously discussed in the literature the tip geometry greatly influences the sense length of the shear force signal (i.e the larger the R_g the greater the sense length).[30] Independent roughness measurements over the substrate (borosilicate slide) were performed by AFM, which provided a RMS roughness of 400 pm. Due to the 2-3 order of magnitude difference between sense length and surface roughness we show that tip-substrate interactions which are attributed solely to surface roughness are not the source of the SF sensitivity herein.

Based upon approach curves generated from multiple tips we recommend a SF amplitude set point value for constant distance imaging that can be measured between 25 % and 40 % of the sense length above the surface (Figure 3.5.A). This range of operating amplitudes reduces tip and substrate contact, whilst maintaining high topographic sensitivity. At lower SF set point amplitudes the interaction forces between the tip and substrate will increase which, depending on the substrate, could result in the damage of the substrate or fouling of the active electrode area.

3.4.4. OBSERVING THE CHANGE IN RESONANCE PEAKS DURING A SHEAR FORCE APPROACH

Comparing the SF amplitude spectra obtained with the tip positioned on and off the surface in Figure 3.5.C, we observed both peaks that are SF sensitive and peaks which are not SF sensitive. Peaks that are not SF sensitive are likely the resonances of the additional SECM components that do not interact with the surface. For peaks that are SF sensitive the amplitude and peak frequency can change with respect to tip-to-substrate separation (Figures 3.5.B and C), hence these changes are due to tip-substrate interactions. This would suggest that the observed change in amplitude in the pullback curve (which is used to control tip-to-substrate distance), is due to a combination of change in the peak amplitude and a shift in the resonance frequency due to the tip-sample interaction.

To better understand the behavior of the tip during the approach/pullback, full frequency spectra at different distances from the surface were measured (Figures 3.5.B and C). Figure 3.5.B shows an approach spectra where two SF sensitive peaks were observed with off surface frequencies of 694 kHz and 697 kHz. For the peak at 694 kHz, as the tip-to-substrate separation decreases, both the amplitude and the frequency of the resonance peak decreases. This suggests the probe was oscillating with a mode akin to a harmonic oscillator which does not have a node located at the end of the tip. As the tip-to-substrate separation decreases, the oscillation mode is progressively damped resulting in the observed shift in frequency and decrease in amplitude. When the tip is on surface the damping has significantly reduced the peak amplitude from 1.1 V to 0.2 V and shifted the peak position to 691 kHz. For the peak at 697 kHz, the peak amplitude decreased as the tip-to-substrate separation decreased, however, no shift in frequency was observed. Similar behavior was observed in Figure 3.5.C with the off surface peak at a frequency of 829 kHz. As these peaks do not exhibit classical behavior for a damped harmonic oscillator, full understanding would require deconvolution of the interacting modes. The high frequencies required for SF sensitivity make this a difficult problem, as the operating frequency of 500 KHz (approximately the SF sensitive frequencies reported herein) corresponds to an oscillation period of 2 μs.

In Figure 3.5.C a second peak was present at a frequency of 832 kHz when the tip was in the SF sensitive regime and in contact with the substrate. However, the amplitude of the peak at 832 kHz does not have a strong dependence upon tip-to-substrate separation. We attribute the peak at 832 kHz to a new resonance mode caused by surface damping as the tip approaches the substrate.

Further understanding of the resonance modes would require modeling the resonance modes of the tip and the influence of tip and surface interactions. However, modeling oscillations on the relevant time scales (~2 µs period) is beyond the scope of this work. However, this should not detract from the observation that the SF sensitive peaks can exhibit both positive and negative amplitude changes with changes in tip-to-substrate separation, and the peak frequency can change.

3.4.5. EXPERIMENTAL FACTORS THAT INFLUENCE SHEAR FORCE SENSITIVITY

To exemplify the dependence of the SF response on the experimental assembly we present data to highlight the influence of the applied oscillation amplitude, separation and alignment of the stimulation piezo and receiver piezos. Additionally, we observed that the pressure exerted between the stimulation and receiver piezo plates and the UME influenced the frequency response.[30] To ensure reproducibility, both the stimulation and receiver piezos were secured with a torque of 0.009 Nm (DID-4 Digital Screw Torque Screwdriver, Cedar). All experiments in this section were performed in air.

Figure 3.5.D shows the dependence of SF amplitude on the stimulation amplitude for a dither-to-receiver separation of 1.00 cm apart (between the edges of the piezo holders), with an alignment of 90°. As the stimulation amplitude was increased, the detected amplitude increases. Figure 3.5.D shows the amplitude response from 1.00V to 10.0 V in the region between 300 to 500 kHz yet the same behavior was observed over larger spectra (10 kHz to 1 MHz) and over a greater range 40 mV to 10.0 V. The effect of the stimulation amplitude on the amplitude SF spectra is presented in (Appendix B Figure B.3.A, B and C). The difference in receiver amplitude was linearly dependent with the applied dither amplitude (Appendix B Figure B.3.D, E and F). This is in agreement with an increased force applied to drive oscillations in a resonator. Therefore, the utilization of higher stimulation amplitude would optimize the overall quality parameter and SF sensitivity. However, large SF amplitudes (e.g. 10 V) would not be suitable for imaging soft substrates that can be

disturbed, or deformed by the large oscillation amplitudes, such as cells. Furthermore, oscillating the probe at a high frequency with large amplitude could induce convection. Therefore, amplitudes of approximately 1V with the reported probes are sufficient to achieve a SF signal with a high Q_F, whilst minimizing local disturbances of the sample and the surrounding environment.

The influence of varying the angle between the stimulation and receiver on the sensitive frequencies was investigated for a dither-to-receiver separation of 1.00 cm, at a dither amplitude of 1 V (Figure 3.6.). The experiments presented in Figure 3.6. have been performed with the same UME, the dither-to-receiver separation and the same pressure exerted on the piezoelectric plates. The same behavior has been observed with repeat measurements using 10 different UMEs, displaying different geometries and taper length, with experiments performed with three different ElPro Scan 3 instruments. The black lines were SF spectra recorded whilst the tip was above surface and the second red spectrum whilst the tip was in contact with the surface. For the cases where the piezo plates were positioned with 0 ° and 90 ° rotation (Figure 3.6.A and B respectively) a SF sensitive peak at *ca*. 380 kHz which attenuated by 0.4 V between off and on surface measurements was observed. In contrast when the piezo plates were positioned with rotations of 45 ° and 180 ° (Figures 3.6.C and D respectively) no significant SF sensitive frequencies were observed (Q_{F} less than 50). More angles have been investigated (Appendix B Figure B.4.), these do not show significant SF sensitive peaks. These data show that the orientation of the two piezo plates has a strong influence on the SF spectra obtained. Additionally, for the highest Q_{F} frequencies positioning the piezos so the receiver is exclusively stimulated by perpendicular (compression/expansion) forces or parallel (shear) forces is required. Interestingly, the case where the receiver is 180 ° out of alignment no SF sensitive frequencies were observed, a stark contrast to when the receiver and dither piezos are in line. This could be attributed to the distribution of mass around the pipet axis affecting the resonance modes of the pipet. Therefore, positioning the piezo plates at either 0 ° or 90 ° alignment is recommended for the greatest SF sensitivity.

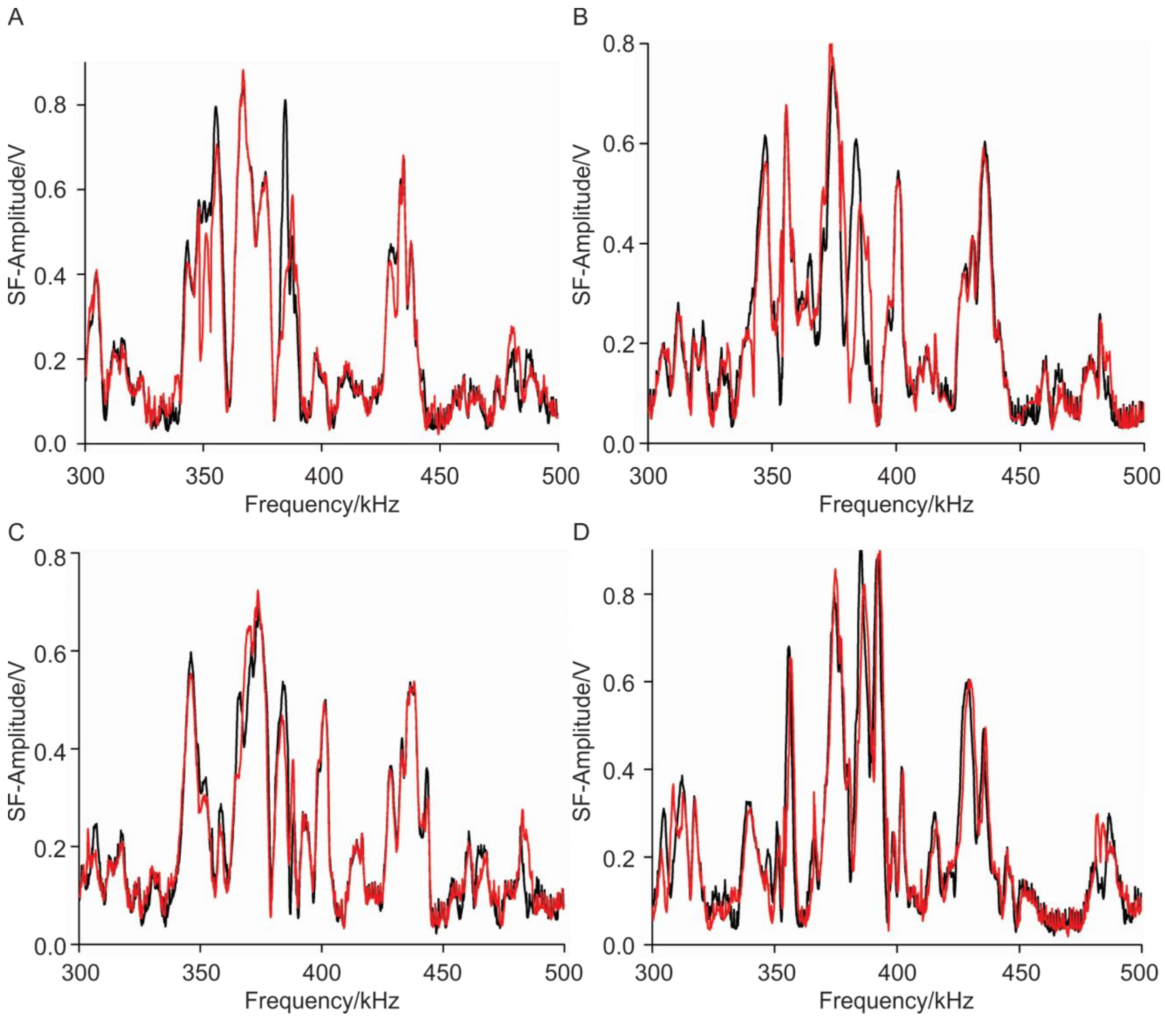

Figure 3.6. The influence of varying the angle between the stimulation and receiver on the sensitive frequencies the (black) solid line is a spectra recorded above surface and the (red) solid line is a spectra recorded on surface with an angle between the dither and receiver (A) 0 ° (B) 90 ° (C) 45 ° (D) 180 °.

3.4.6. DEPENDENCE OF THE DISTANCE BETWEEN DITHER AND RECEIVER ON THE SHEAR FORCE SENSITIVE FREQUENCIES

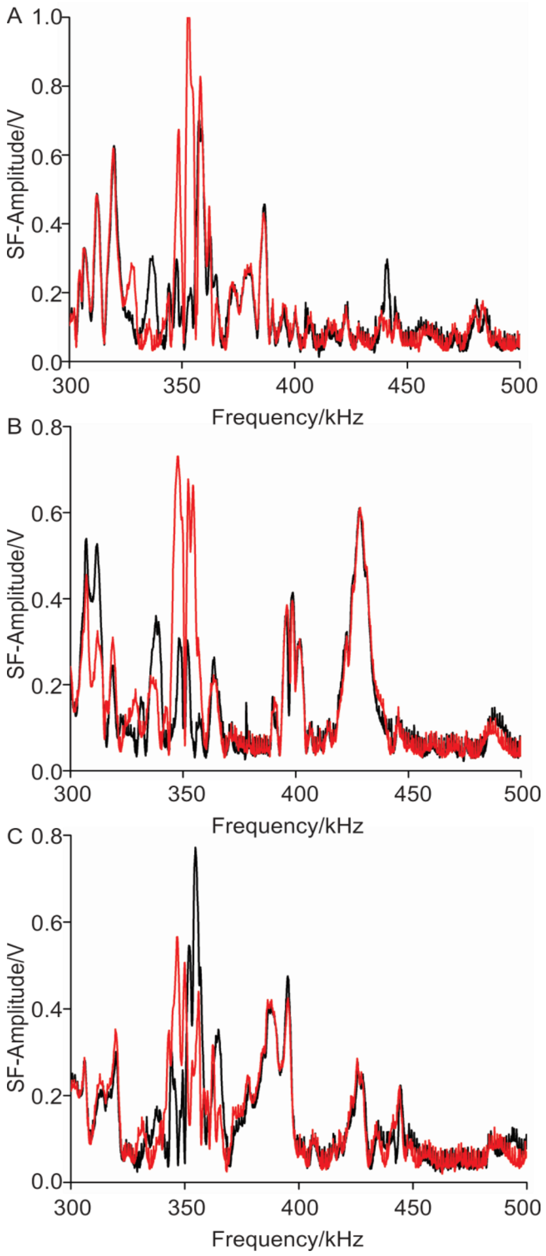

Figure 3.7. The influence of varying the distance between the stimulation and receiver on the sensitive frequencies the (black) solid line is a spectra recorded off surface and the (red) solid line is a spectra recorded on surface with a distance between the dither and receiver of (A) 15.1 mm (B) 10.1 mm (C) 5.5 mm.

Figure 3.7. shows how the separation of the piezo plates influences the recorded SF spectra. When the distance between the two piezo plates was varied the SF spectra was significantly altered, with both peak position and peak amplitude being affected. The difference in total response, sense length and Q_F vary with the distance between the piezos. However, no clear trend could be identified as suitable SF frequencies were found and every distance had a SF frequency with a Q_F greater than 50. We attribute the variation in spectra to the changing mass distribution on the pipet as the piezo plates contribute a significant weight to the total mass of the probe. Under our experimental conditions our probes were more amenable to operate with a dither to receiver distances of 1.00 cm, hence this separation was used purely on practical grounds.

3.4.7. IMAGING TOPOGRAPHY AND ELECTROCHEMISTRY SIMULTANEOUSLY WITH SHEAR FORCE - SCANNING ELECTROCHEMICAL MICROSCOPY

To demonstrate the practical use of the nano-probes for SF-SECM, proof of concept measurements were performed over a test substrate (an acid etched CD). Figure 3.8.A and B show the AFM image of a 10 µm × 10 µm portion of the CD surface. The image reveals 1.2 µm wide plateaus, 110 nm high, and separated by 690 nm wide valleys. The simultaneously measured topographic and electrochemical line scans measured using SF-SECM in a solution containing 3.5 mM FcMeOH /0.1M KCl were shown in Fig 8C. A nanoelectrode with r_T = 47 nm and R_g = 5 was employed with a stimulation amplitude of 130 mV, and the approach set point as 40% of the amplitude off surface, scans were performed at 0.1 µm s^{-1}. The shear force topography line scan reproduces the plateaus and valleys visualized by AFM (Figures 3.8.A, B and C). A maximum depth of 80 nm is reported by SF topography, the difference in height between AFM and SF topography was due to tip convolution preventing complete penetration of the UME into the recession (pit width 690 nm compared to outer glass radius of *ca*. 235 nm). Figure 3.8.C and D shows the electrochemical response during the scan where the tip current decreases over the raised sections and increases in the recessed regions. Figure 3.8.C shows a constant current of 0.7 nA was measured on the plateaus of the CD, with the current increasing to 4 and 6 nA within the recessed regions of the CD. When the electrode was positioned in the bulk solution (greater than 1 mm from the substrate) a steady state limiting current of 1.1 nA was recorded. Therefore, the

Figures 3.8.C and D show that the raised sections of the CD provide a negative feedback response and that the recessed regions provide a positive feedback response, with a measured current in excess of the bulk solution. Importantly, the electrochemical current remains constant on the plateaus whilst there are small variations in topography measured by SF, indicating that the nanoelectrodes are suitable for tracking topography. The topographic image (Figure 3.8.E) shows excellent agreement for the location of the recessed regions and the plateaus compared to the electrochemical map (Figure 3.8.D).

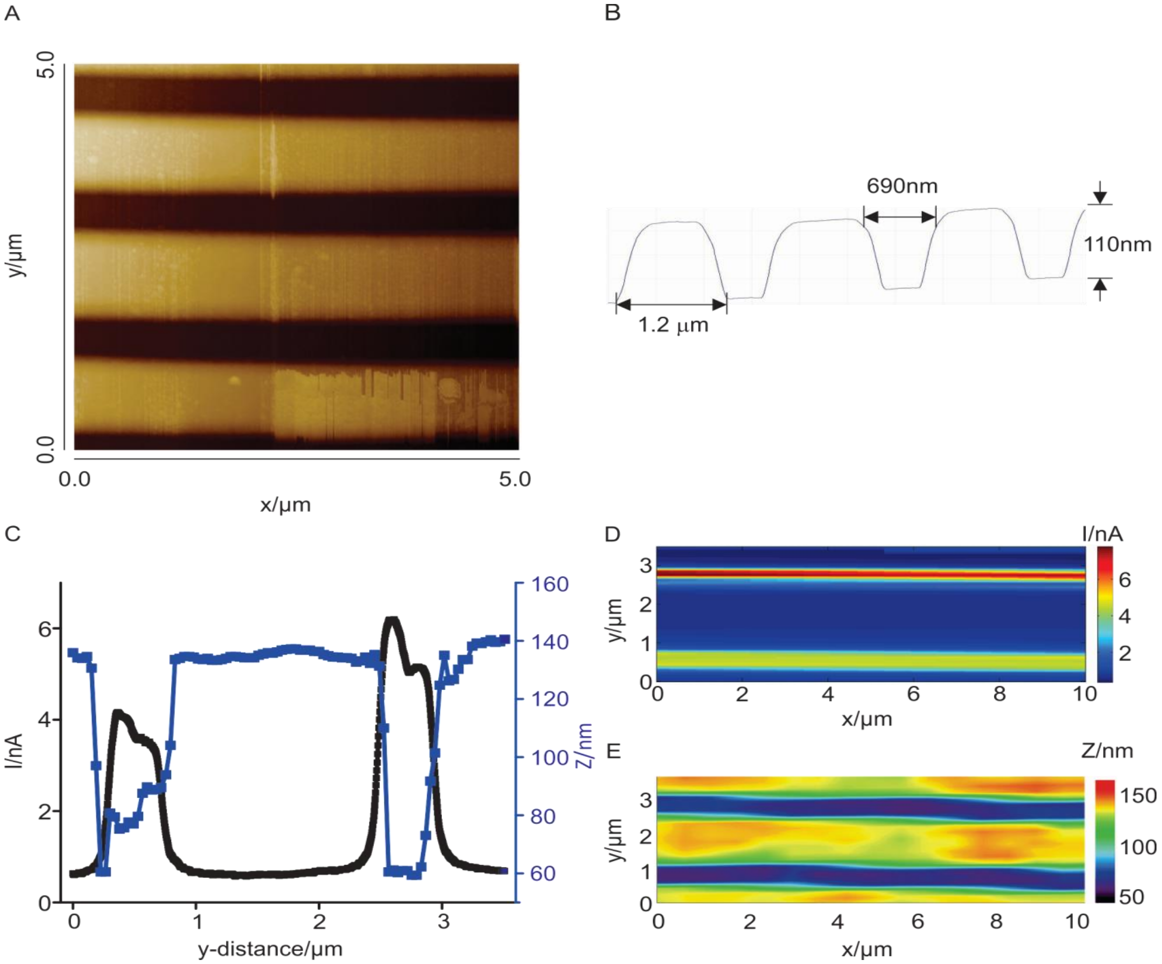

Figure 3.8. (A) Tapping mode AFM image of CD-R surface, where the raised areas were non-conductive and the recessed areas were conductive. (B) Topographic transect along the dotted line of A. (C) Topography and electrochemical current transects (D) SECM image of a 10 µm × 3.5 µm portion of CD surface obtained with a 47 nm radius Pt microelectrode (R_g = 5). (E) Shear force topography image.

We have reported the successful mass fabrication of Pt/quartz glass disk electrodes with an active electrode radius of 3 nm to 190 nm with a typical ratio of insulator to conductor ranging from 5 to 25. These electrodes have been thoroughly characterised by bulk electrochemical measurements and electrochemical approach curves. The well-defined geometry of the conducting and glass of the electrode has been confirmed by electron microscopy.

Furthermore, this fabrication procedure produces long flexible tapers that provide excellent SF sensitivity with a high signal to noise ratio and suitable sense length (between 25 nm and 465 nm). In order to achieve the highest SF sensitivity we investigated the nature of the approach curve by recording frequency spectra within the SF sense length of the probe. Different SF sensitive responses observed included a change in frequency and decrease in peak amplitude as the UME approached the substrate, indicative of resonance damping; a peak which decreased in amplitude, without a change in peak frequency; and an increase in peak amplitude as the tip approached the substrate, which we attribute to a new resonance mode of the UME.

To further enhance the SF sensitivity we looked into dominant experimental factors which influence the SF spectra. By increasing the stimulation amplitude a linear increase in the SF response was recorded, however, we stress that when dealing with low viscosity solutions or soft substrates care should be taken to avoid solution convection or substrate alteration due to tip oscillations. For the experimental configuration presented, we observed the most desirable SF properties were obtained with the piezo elements parallel and perpendicular to each other. However, there was significant change in the SF spectra, however, no clear trend in the recorded SF sensitivity when the separation between the piezo plates varied. These data highlight the importance of understanding the UME resonance modes, tip-piezo interaction and piezo operation modes to optimize the SF response and will be a subject of future work.

The capability of the nanoelectrodes to perform simultaneous topographic and electrochemical measurements has been successfully demonstrated. An etched blank CD-R was mapped showing excellent agreement between the lateral size of features recorded by SF topography and AFM. Small discrepancies between the vertical heights measured by the two techniques were due to the comparable width of the trenches to the UME size causing tip convolution. Importantly, the electrochemical features accurately correspond to the SF topography, clearly demonstrating the functionality of these probes for SF-SECM measurements.

[1] A.J. Bard, F.R.F. Fan, J. Kwak, O. Lev, Analytical Chemistry, 61 (1989) 132-138.

[2] X. Zhao, P.M. Diakowski, Z. Ding, Analytical Chemistry, 82 (2010) 8371-8373.

[3] I. Beaulieu, S. Kuss, J. Mauzeroll, M. Geissler, Analytical Chemistry, 83 (2011) 1485-1492.

[4] K. Eckhard, T. Erichsen, M. Stratmann, W. Schuhmann, Chemistry - A European Journal, 14 (2008) 3968-3976.

[5] P. Sun, M.V. Mirkin, Analytical Chemistry, 78 (2006) 6526-6534.

[6] A.L. Barker, P.R. Unwin, S. Amemiya, J. Zhou, A.J. Bard, Journal of Physical Chemistry B, 103 (1999) 7260-7269.

[7] A.L. Barker, P.R. Unwin, J. Zhang, Electrochemistry Communications, 3 (2001) 372-378.

[8] S. Krämer, R.R. Fuierer, C.B. Gorman, Chemical Reviews, 103 (2003) 4367-4418.

[9] M. Ludwig, C. Kranz, W. Schuhmann, H.E. Gaub, Review of Scientific Instruments, 66 (1995) 2857-2860.

[10] M.A. Alpuche-Aviles, D.O. Wipf, Analytical Chemistry, 73 (2001) 4873-4881.

[11] C. Gabrielli, F. Huet, M. Keddam, P. Rousseau, V. Vivier, Journal of Physical Chemistry B, 108 (2004) 11620-11626.

[12] T. Yasukawa, T. Kaya, T. Matsue, Analytical Chemistry, 71 (1999) 4637-4641.

[13] J.V. Macpherson, P.R. Unwin, Analytical Chemistry, 72 (2000) 276-285.

[14] A. Kueng, C. Kranz, A. Lugstein, E. Bertagnolli, B. Mizaikoff, Angewandte Chemie - International Edition, 42 (2003) 3238-3240.

[15] A. Kueng, C. Kranz, B. Mizaikoff, A. Lugstein, E. Bertagnolli, Applied Physics Letters, 82 (2003) 1592-1594.

[16] D.O. Wipf, A.J. Bard, D.E. Tallman, Analytical Chemistry, 65 (1993) 1373-1377.

[17] K. McKelvey, M.A. Edwards, P.R. Unwin, Analytical Chemistry, 82 (2010) 6334-6337.

[18] Y. Takahashi, A.I. Shevchuk, P. Novak, B. Babakinejad, J. Macpherson, P.R. Unwin, H. Shiku, J. Gorelik, D. Klenerman, Y.E. Korchev, T. Matsue, Proceedings of the National Academy of Sciences of the United States of America, 109 (2012) 11540-11545.

[19] B. Ballesteros Katemann, A. Schulte, W. Schuhmann, Chemistry - A European Journal, 9 (2003) 2025-2033.

[20] Y. Lee, Z. Ding, A.J. Bard, Analytical Chemistry, 74 (2002) 3634-3643.

[21] U.M. Tefashe, G. Wittstock, Comptes Rendus Chimie, 16 (2013) 7-14.

[22] A. Schulte, M. Nebel, W. Schuhmann, Single Live Cell Topography and Activity Imaging with the Shear-force-based Constant-distance Scanning Electrochemical Microscope, (2012) 237-254.

[23] Y. Takahashi, H. Shiku, T. Murata, T. Yasukawa, T. Matsue, Analytical Chemistry, 81 (2009) 9674-9681.

[24] M. Etienne, B. Layoussifi, T. Giornelli, D. Jacquet, Electrochemistry Communications, 15 (2012) 70-73.

[25] M. Etienne, A. Schulte, S. Mann, G. Jordan, I.D. Dietzel, W. Schuhmann, Analytical Chemistry, 76 (2004) 3682-3688.

[26] A. Hengstenberg, C. Kranz, W. Schuhmann, Chemistry - A European Journal, 6 (2000) 1547-1554.

[27] B. Ballesteros Katemann, A. Schulte, W. Schuhmann, Electroanalysis, 16 (2004) 60-65.

[28] M. Nebel, K. Eckhard, T. Erichsen, A. Schulte, W. Schuhmann, Analytical Chemistry, 82 (2010) 7842-7848.

[29] K. Borgwarth, D.G. Ebling, J. Heinze, Berichte der Bunsengesellschaft/Physical Chemistry Chemical Physics, 98 (1994) 1317-1321.

[30] M. Etienne, S. Lhenry, R. Cornut, C. Lefrou, Electrochimica Acta, 88 (2013) 877-884.

[31] A.J. Bard, M.V. Mirkin, Taylor & Francis, 2001, p.51.

[32] M. Etienne, E.C. Anderson, S.R. Evans, W. Schuhmann, I. Fritsch, Analytical Chemistry, 78 (2006) 7317-7324.

[33] B.B. Katemann, W. Schuhmann, Electroanalysis, 14 (2002) 22-28.

[34] Y. Shao, M.V. Mirkin, G. Fish, S. Kokotov, D. Palanker, A. Lewis, Analytical Chemistry, 69 (1997) 1627-1634.

[35] M.A. Mezour, M. Morin, J. Mauzeroll, Analytical Chemistry, 83 (2011) 2378-2382.

[36] C.G. Zoski, Handbook of electrochemistry, Elsevier Science Limited, 2007, pp.220-232.

[37] R. Cornut, C. Lefrou, Journal of Electroanalytical Chemistry, 608 (2007) 59-66.

[38] C. Lefrou, Journal of Electroanalytical Chemistry, 592 (2006) 103-112.

[39] C. Lefrou, R. Cornut, ChemPhysChem, 11 (2010) 547-556.

[40] A.J. Bard, L.R. Faulkner, Electrochemical Methods: Fundamentals and Applications, 2 (1980) p. 171.

[41] R. Cornut, C. Lefrou, Journal of Electroanalytical Chemistry, 604 (2007) 91-100.

[42] L.P. Bauermann, W. Schuhmann, A. Schulte, Physical Chemistry Chemical Physics, 6 (2004) 4003-4008.

CHAPTER 4: ANODIC STRIPPING VOLTAMMETRY AT NANOELECTRODES: TRAPPING OF MANGANESE (II) BY CROWN ETHERS

The detection of metal species, specifically manganese ions in battery electrolyte solutions, is of particular interest as Mn^{2+} dissolution has been determined to be associated with the decrease in capacity of lithium manganese oxide battery with charge/discharge cycling. Mercury hemispherical nanoelectrodes are capable of detecting low concentrations of heavy metals when used with the analytical method of ASV. The standard platinum nanoelectrode presented in the previous chapter can be easily modified by electrochemically depositing mercury on the disk surface to create a hemispherical Hg nanoelectrode. Hg-based ASV functions by allowing the specific ionic species (for instance Mn^{2+} in this case) to form an amalgam with the mercury hemisphere in the reductive scan. Subsequently performing the oxidation of the species results in a peak that is proportional to the concentration of the specific ion in solution.

Chapter 4 focuses on developing the use of these Hg / Pt nanoelectrodes in the study of battery materials. The Hg-based ASV technique developed in this chapter has been used to evaluate the efficiency of a methodology developed by our industrial partner to effectively mitigate the negative effects of manganese dissolution. More precisely, the methodology involves the use of polymeric chelating crown ethers as separator coatings to sequester Mn^{2+}. This decreases its ability to migrate to the negative electrode and form a passivation layer, resulting in an improved capacity retention of manganese containing LIBs.

The work presented in this chapter was originally published and is adapted with permission from:

Danis L., Gateman S.M., Snowden M.E., Halalay I., Howe J., Mauzeroll, J., *Anodic Stripping Voltammetry at Nanoelectrodes: Trapping of* Mn^{2+} *by Crown Ethers*. Electrochimica Acta. 2015, 162, 169-175. Copyright © 2015, Elsevier

4.1. ABSTRACT

The work presented here describes the development and characterization of platinum-mercury hemispherical nanoelectrodes for the spatially resolved quantitative detection of manganese cations. The electrochemical probes were made by electrodeposition of metallic mercury from a mercuric ion solution onto Pt/quartz laser-pulled concentric disk nanoelectrodes (with disk radii ranging from 3 to 500 nm). The nanoelectrodes were characterized by steady-state voltammetry, scanning electrochemical microscopy, environmental scanning electron microscopy, energy-dispersive X-ray spectroscopy and calibrated with respect to the concentration of Mn^{2+} ions using anodic stripping voltammetry. The fully characterized probes were employed for the quantitative detection of Mn^{2+}. The technique has been used to evaluate the impact of a novel approach for mitigating the undesirable consequences of manganese dissolution in Li-ion batteries.

4.2. INTRODUCTION

Over the past 20 years, miniaturization of electrochemical probes has progressed from micron to submicron sizes, leading to the introduction of nanoscale electrodes suitable for SECM studies.[1-4] Different probe geometries have been developed and characterized, including co-planar disk,[5] recessed disk,[6] and hemispherical. Multi-functional probes have also been developed [7] and the functionalization of nano-electrodes by electro-deposition has been demonstrated. An example of these includes the formation of nanometer scale hemispheres of mercury.[8, 9]

Both macro- and micro-scale mercury electrodes have been used extensively in fundamental electrochemistry and analytical applications. Fundamental studies employed mercury electrodes for double layer capacitance investigations.[10, 11] Analytical applications focused mainly on the detection of low concentrations of heavy metals via stripping voltammetry.[12] In stripping voltammetry with a mercury electrode, a reduction potential is applied to form an amalgam with metal ions from the solution, before an oxidative sweep is applied. The metals within the amalgam are ionised during the oxidative sweep, giving rise to peaks characteristic of the metals, with peak areas corresponding to their amounts.[13] Historical drawbacks of stripping voltammetry include the time required for amalgam formation and the capacitive background signal associated with fast scan techniques. A nanoscale mercury electrode provides the advantages of increased mass transport, reduced amalgam formation time, and significantly reduced capacitive effects, due to its significantly smaller surface area compared to microelectrodes.

Detection of manganese ions in non-aqueous electrolyte solutions for LIBs is of growing interest, due to the wide use of manganese containing positive electrode materials. Among this latter class of materials, $Li_xMn_2O_4$ is of particular interest due to its low cost, good rate capability and low toxicity. $Li_xMn_2O_4$ has a theoretical specific capacity of 148 mAh g^{-1}, similar to that of $LiCoO_2$ (140 mAh g^{-1}). However, $Li_xMn_2O_4$, with two charge/discharge plateaus at 3.95 and 4.15 V (*vs.* Li^+/Li), has a higher average potential than $LiCoO_2$, which has charge/discharge plateaus of 3.0 and 4.2 V (*vs.* Li^+/Li)).[14, 15] Despite these advantages, $Li_xMn_2O_4$ exhibits poor capacity retention during cycling and storage, compared with $LiCoO_2$, particularly at elevated temperatures (>35 ºC). This limits its widespread commercial use, especially for large-scale automotive applications. Proposed mechanisms for the capacity-fade include the Jahn-Teller lattice distortion caused by Mn^{3+} (d^4) ions,[16] the oxidation of solution species on the electrode surface, and the dissolution of Mn^{2+} into the electrolyte[17-19] via the charge disproportionation reaction,[20]

$$2\mathrm{Mn}^{3+} \rightarrow \mathrm{Mn}^{2+} + \mathrm{Mn}^{4+} \tag{4.1}$$

Which is exacerbated by the presence of hydrogen fluoride (HF) in the electrolyte solution.[21, 22] The manganese cations then electro-migrate to the negative electrode, where they lead to electrolyte reduction and film growth which result in reduced power performance, reversible capacity, and a shortened LIB life. Capacity fade is particularly high with graphite negative electrodes, one of the most widely used materials in commercial LIBs. Several methods (mainly anion and cation substitutions [23] in the $Li_xMn_2O_4$ lattice and coatings on electrode surfaces [24, 25]) have been developed over the past two decades for mitigating manganese dissolution and its consequences, but none is 100 % effective. Therefore it is necessary to devise alternative and complementary technological approaches for solving this problem. A novel approach to mitigating the consequences of manganese dissolution in LIBs proposes the use of cation trapping agents (in particular crown ethers) tethered to polymers placed in the inter-electrode space, to sequester manganese cations and prevent their migration to the negative electrode. It was shown that separators coated with polymeric 18-crown-6 (18C6) or aza-15-crown-5 (A15C5) can both reduce the capacity fade rate and the amount of manganese deposited on the negative electrode during the high temperature (50 ºC or 60 ºC) cycling of $Li_xMn_2O_4$–graphite cells by as much as factors of 2x and 2.5x, respectively, compared with baseline cells containing uncoated separators.[26, 27]

An improved understanding of the mechanism of Mn dissolution should provide insights for increasing the efficiency of methods which aim to block the dissolution pathway or to mitigate the consequences of manganese dissolution. Different characterization techniques have been used to quantify dissolved manganese, including energy dispersive x-ray spectroscopy (EDS or EDX) and inductivity coupled plasma atomic emission spectroscopy (ICP-AES).[28] EDS has been used to examine graphite electrodes (anodes) for surface manganese after the polarization of the $Li_xMn_2O_4$ electrode to 4.5 V at C/50.[29] These techniques revealed pronounced amounts of manganese located on the graphite electrode (anode), indicating significant Mn dissolution from the cathode. These analysis methods can accurately quantify the presence of manganese, but they are performed as *ex-situ* post-mortem studies. Furthermore, recent X-ray near-edge spectroscopy (XANES) data indicate an average oxidation state of +3.2 to +3.4 for manganese cations in the electrolyte solution from $Li_xMn_2O_4$-graphite cells cycled at high temperatures. This result calls into question the relevance of the dissolution mechanism shown in eqn. (1) for understanding Mn dissolution in LIBs.[29] However, the XANES measurements were also performed *ex-situ*, albeit on wet cell components, immediately after cell disassembly. Development of methodologies for real time *in-situ* measurements on battery materials is therefore necessary to exclude any data adulteration by sample handling artifacts and should lead to new insights into reaction mechanisms.

We present herein the development and characterization of mercury capped nanoelectrodes for the quantitative detection of manganese ions. Spherical mercury caps were electroplated onto Pt nanoelectrodes. The presence of mercury on the tip of the probe was confirmed by electron microscopy and elemental analysis. The geometry of the cap was determined by steady state electrochemical measurements and confirmed by a comparison of experimental and simulated negative feedback approach curves. The ASV procedure was optimised and shown to enable the quantitative detection of Mn^{2+} ions at concentrations ranging from nano- to micro-molar. The measured manganese trapping site occupancy in polymeric A15C5 was close to 100 %.

4.3. EXPERIMENTAL

4.3.1. FABRICATION PLATINUM NANOELECTRODES AND DEPOSITION OF MERCURY

The platinum disk nanoelectrodes were produced by laser-pulling (P-2000, Sutter Instrument Company, USA) a 25 µm diameter Pt wire (99.99 % purity; hard temper; Goodfellow, England) into a quartz glass capillary (L: 10 cm; O.D.:1.0 mm; I.D.:0.50 mm; Sutter Instrument, USA), under vacuum.[2, 5] After fabrication, all nanoelectrodes were polished, in order to expose the metal surface, using a commercial variable speed polisher (Tegrapol 23, Struers, Canada) and washed with acetone. The Hg/Pt hemispherical nanoelectrodes were obtained by electrodeposition from a 10 mM $Hg_2(NO_3)_2$ (Acros Organics, New Jersey, USA) solution in 0.1 M KNO_3 acidified to 0.5 % with HNO_3. Deposition of Hg was performed at a potential of -500 mV in a three electrode setup using a chloride free Hg/Hg_2SO_4 (Sat. K_2SO_4) (REF 601, Radiometer Analytical, Burlington, USA) reference electrode and a platinum wire (99.99 +% purity; 0.5 mm diameter; Goodfellow, England) counter electrode.[8, 9, 30, 31] All electrochemical solutions were de-aerated with Ar (> 99.998 %, Praxair) and maintained under an argon blanket for the duration of the experiments. Electrochemical measurements were performed with an ElProScan 3 system (ELP 3), using Potmaster software (version v2x66) and an ElProScan Controller ESC 3 equipped with a SF unit, (SFU 3, HEKA Elektronik, Germany).

4.3.2. CHARACTERIZATION OF MERCURY / PLATINUM NANOELECTRODE PROBES

The radius of the Pt electroactive surface (r_t), and the quality of platinum-glass seal were evaluated using cyclic voltammetry (CV) in an aqueous solution of 1 mM Ruhex (Sigma Aldrich, Oakville, Canada) ($D = 6.0 \times 10^{-6} cm^2 s^{-1}$) and 0.1 M potassium nitrate KNO_3 (Sigma Aldrich, Oakville, Canada). The potential was swept linearly from -300 to -900 mV at a scan rate of 5 mV s^{-1} prior to the Hg electrodeposition. The radius of the quartz, r_g, was determined from the negative feedback approach curves over an insulating CTFE plastic puck. The approach curves were recorded at an approach speed of 0.5 µm s^{-1}. All potentials were recorded relative to a Hg/Hg_2SO_4 (Sat. K_2SO_4) reference electrode using a Pt wire counter electrode unless mentioned otherwise.

The Hg/Hg_2SO_4 (Sat. K_2SO_4) reference was used in order to avoid possible leakage of the chloride ions from more standard reference electrodes such as SCE or Ag/AgCl, and its potential, as well as reactions with manganese species. To determine whether the Pt disk was completely covered by the Hg hemisphere, as well as Pt_2Hg intermetallic, the proton reduction overpotential was investigated using linear sweep voltammetry from 0 to -2.0 V *vs.* an in-house chlorinated silver wire quasi-reference electrode in a degassed 0.1 M KNO_3 solution. Scanning electron microscopy and energy dispersive X-ray spectroscopy (EDS) were performed using a Hitachi S-3500 variable pressure SEM (VPSEM) equipped with an Oxford solid state detector (SSD) at 20 kV and air at 100 Pa pressure. During the EDS analysis, the electrode was secured to an aluminum sample stub with carbon paste or copper tape. Manganese solutions were prepared through dilution of a stock solution containing 10 mM manganese(II) nitrate hydrate salt (99.99 % Sigma-Aldrich, St. Louis, USA) and 0.1 M KNO_3 by additions of 0.1 M KNO_3 solution. Mn concentrations were confirmed by inductively coupled plasma atomic emission spectroscopy (ICP-AES) using an iCAP 600 series ICP-AES spectrometer (Thermo Scientific) calibrated with manganese acetate in 4 % HNO_3 standard solutions (PlasmaCal). ASV was performed in a three-electrode system, with the Pt-Hg electrode as working electrode, Hg/Hg_2SO_4 as reference electrode, and a Pt wire as counter electrode.

4.4.1. MERCURY DEPOSITION DISCUSSION

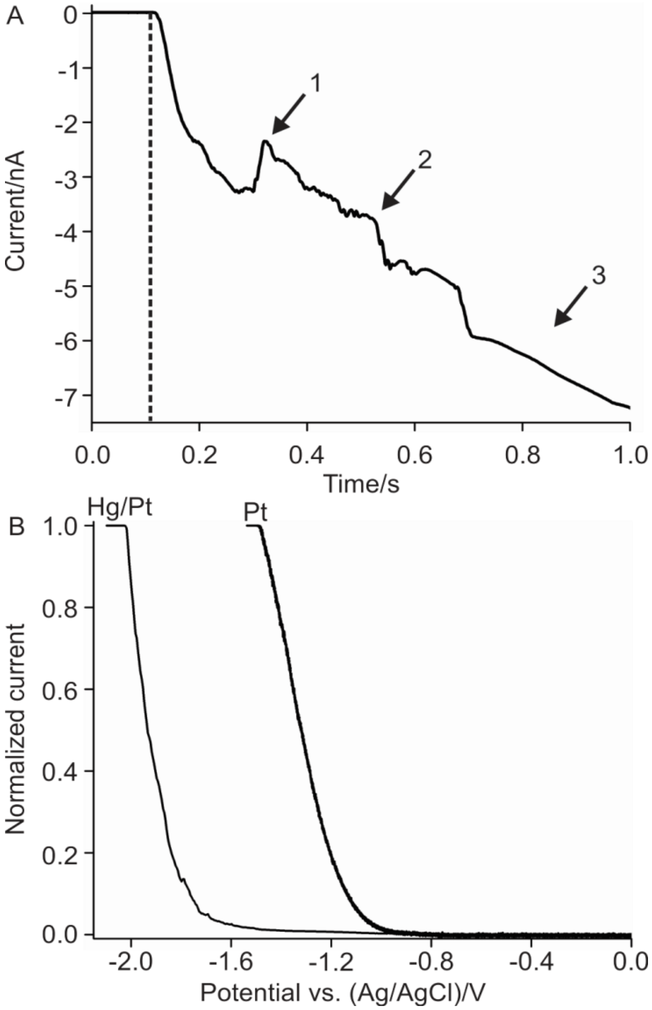

Figure 4.1. (A) Hg deposition curve where a potential of 0 V was held for 0.15 s before a potential step of -0.5 V vs. Hg/Hg_2SO_4 (Sat. K_2SO_4) was applied for a duration of 1.25 s. The change from 0 V to the applied potential is represented by the dotted line at 0.15 s. Stage 1 represents the thin layer Pt_2Hg formation, stage 2 represents the nucleation of Hg, and stage 3 the nuclei coalescence and growth of the spherical cap. (B) Linear sweep voltammetry data obtained at a scan rate of 10 mV s^{-1} for the bare Pt electrode (Pt) and the Pt electrode after deposition of Hg (Hg/Pt); both performed in deaerated 0.1 M KNO_3. Note also that the data shown in (A) and (B) were recorded with different nanoelectrodes.

The current versus time plot shown in Figure 4.1.A was obtained by allowing the open circuit potential to stabilize for 0.15 s before stepping the potential to -500 mV *vs.* Hg/Hg_2SO_4 (Sat. K_2SO_4), as shown on the figure by the dotted line. (The data was recorded with a Pt nano-electrode having r_T = 207 nm and r_g = 4.1 µm.) As reported previously, 3 stages occur during the electrodeposition of the Hg spherical cap.[30] Immediately after stepping the potential to -500 mV *vs.* Hg/Hg_2SO_4 (Sat. K_2SO_4), a smooth increase in absolute value in current can be seen, due to the formation of a thin Pt_2Hg layer (stage 1). The fluctuations in the current response between $0.2 < t < 0.7$ s on the deposition curve indicate the nucleation of Hg on the electrode surface (stage 2). These nuclei coalesce at ~0.7 s, followed by the growth of the spherical cap, as indicated by the final smooth increase in absolute value of the current (stage 3). Similarly, the rapid occurrence of multiple nucleation sites at similar deposition potentials of the mercury on Pt nanoelectrodes has been reported previously.[8] After fabrication the Hg/Pt nanoelectrodes are stored in degassed KNO_3. The complete coverage of the Pt surface was observed using linear sweep voltammetry in deaerated 0.1 M KNO_3 solution. Figure 4.1.B shows that the proton reduction occurs at -1.4 V for the Hg spherical cap electrode, compared to -0.8 V for the bare Pt nanoelectrode. The shift in the reduction potential proves that the Pt electrode is completely covered by the Hg cap.

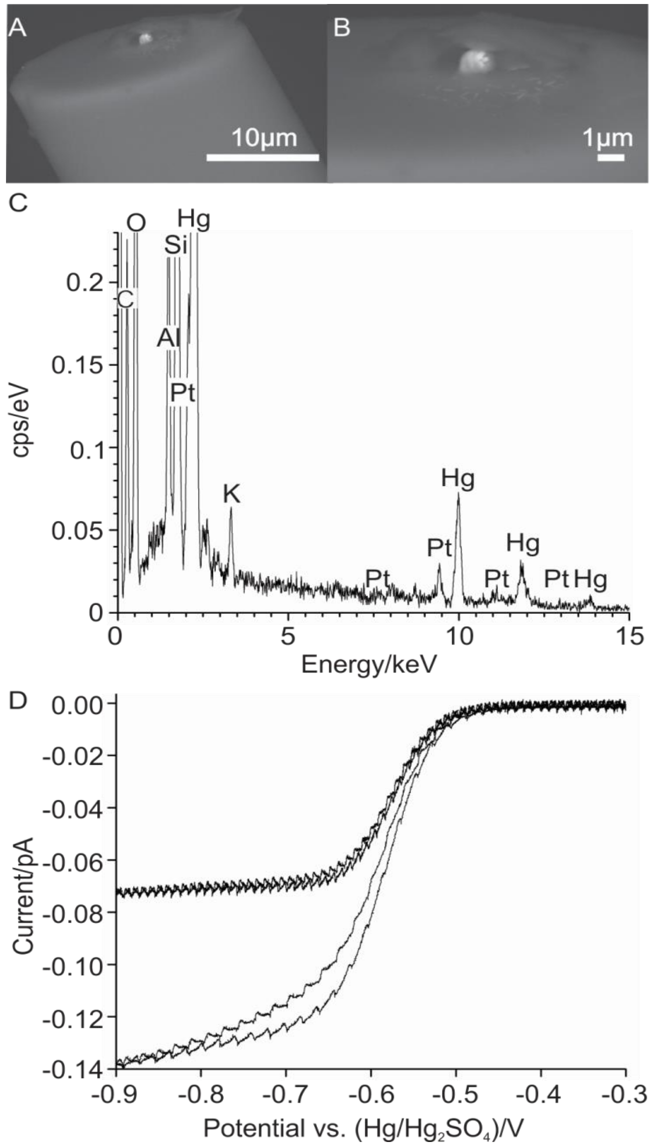

Figure 4.2. Nanoelectrode characterization: (A) ESEM side view image of the top of an Hg/Pt nanoelectrode; (B) ESEM zoomed image of the same Hg hemispherical cap. (C) EDS data for the Hg/Pt nanoelectrode displays strong signals for Hg and Pt, proving the presence of the mercury hemispherical cap over the platinum disk nanoelectrode. (D) Voltammetric behavior of a nanoelectrode Pt and Hg/Pt hemispherical nanoelectrode in 1 mM Ruhex in 0.1 M KNO_3. Note that the data in panels (A), (B), and (C) were obtained for the same electrode and the data in (D) were recorded with a different Hg/Pt nanoelectrode.

The r_T and r_g dimensions of the Pt nanoelectrodes were determined by CVs and approach curves in negative feedback modes prior to Hg deposition, as described previously. Subsequent to the deposition of the mercury onto the Pt nanoelectrode, all Hg/Pt nanoelectrodes were characterized by environmental scanning electron microscopy (ESEM) imaging and by the analysis of the I_{ss} using finite element modelling (*vide infra*). Figures 4.2.A and B show SEM images of a Pt nanoelectrode after deposition of Hg. A well-defined spherical cap can be observed on the Pt electrode. The radius of the mercury hemisphere is about 500 nm, which falls into the range for the radius of the pulled Pt wire. SEM and EDS were performed at a pressure of 100 Pa (in air), to make the rate of evaporation of mercury negligible on the time scale of the measurements. Therefore, the SEM images reflect the true microstructure of the mercury capped nanoelectrodes. During the EDS analysis (Figure 4.2.C), the electrode was secured with carbon paste to an aluminum sample stub. This produced the Al and C signals seen in the EDS spectra. Si and O signals stem from the quartz capillary surrounding the Pt wire. Strong signals for Hg and Pt were observed, confirming the presence of the spherical mercury cap on the surface of the platinum disk nanoelectrode. The uneven area surrounding the mercury cap is due to drying effects of the solvent, hence the presence of K in the EDS spectra. A total of four set of EDS analyses have been collected on three different Hg/Pt nanoelectrodes, leading to the same conclusion.

The CVs shown in Figure 4.2.D exhibit a sigmoidal shape and achieve diffusion-limited steady-state currents for the reduction of Ruhex when a potential of -600 mV (or greater) *vs.* Hg/Hg_2SO_4 (Sat. K_2SO_4) is applied for both the Pt and Hg/Pt spherical cap electrodes. Under diffusion control, the i_{ss} is given by Equation 2.3 in Chapter 2

The Hg/Pt CVs performed in Ruhex had a steady state limiting current which was greater than predicted by Equation 2.3 for a hemispherical electrode of radius, r_T. Therefore it was necessary to simulate the spherical cap geometry using a finite element modelling method.

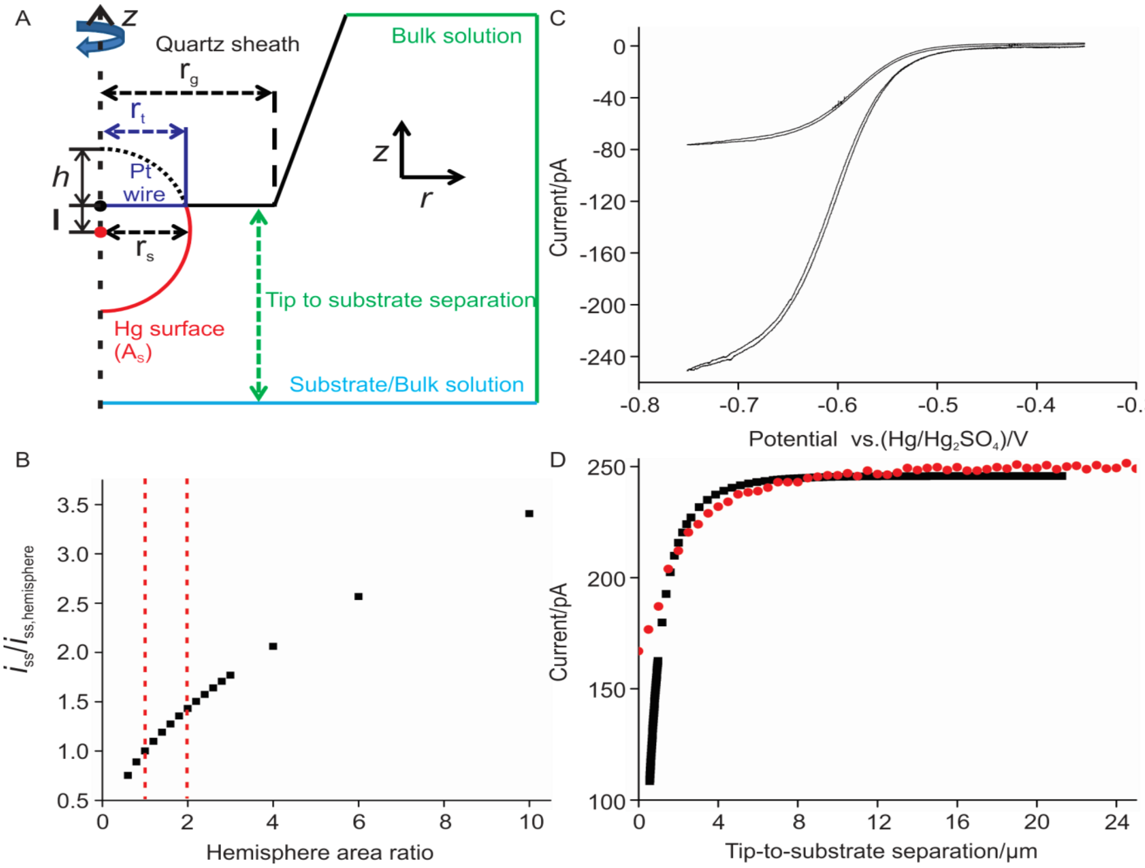

Figure 4.3. (A) Schematic of the 2D axisymmetric simulation domain of the spherical capped electrode (not to scale). The axis of rotational symmetry is represented by the vertical dotted line. Origin is represented by the dot where the axis of symmetry intercepts the plane of the platinum electrode. The angle between the edge of the quartz sheath and the axis of symmetry was set at 7 degrees to match SEM images of the fabricated UMEs. The side wall then extends to a height which is at least 100x greater than the r_g. Therefore the position that the pipet touches the domain boundary will be r_g + (tan(7) * domain height). (B) Simulated data of the hemisphere area ratio with respect to the normalised steady state current. The dotted lines represent the typical experimental range for hemisphere area ratios obtained with this deposition method, using a Pt disk electrode of r_T = 25 nm in a solution with where c^* = 1.0 mM and D = 6.0 X 10^{-6} cm^2 s^{-1}. (C) Experimental CVs for a Pt UME of r_T = 207 nm before and after deposition of a Hg spherical cap in 1.1 mM Ruhex solution. (D) Experimental (red circle dotted line) and simulated (black square dotted line) negative feedback approach curves for a Hg spherical cap UME of r_t = 207 nm, R_g = 4.1 µm, r_s = 319 nm and the z component of **l** = -243 nm in 1.1 mM Ruhex solution.

Finite element simulations of the nanoelectrode with a spherical cap were performed using a commercial finite element method (FEM) modeling package (Comsol Multiphysics 4.4, Comsol AB). According to standard good practice for finite element simulations, the mesh was sufficiently fine that further refinement provided no significant change in the flux at the electrode surface. The simulation domain is outlined in Figure 4.3.A, and represents the electrolyte solution. We assume a 2D-axisymmetric geometry around the z-axis of the nanoelectrode (dotted vertical line Figure 4.3.A) with the radial co-ordinate defined as r. The mercury spherical cap completely covers the Pt electrode, and contacts the insulating sheath at the point $r = r_{\mathrm{T}}$. The spherical cap radius (r_{s}), and the vector from the origin to the center of the spherical cap (**l**), were determined by simultaneously solving Equations (4.2) and (4.3) for the bounds defined in (4.4),

$$r_{\mathrm{s}} = \frac{r_T^2 + h^2}{2h} \tag{4.2}$$

$$A_{\mathrm{s}} = \pi(r_{\mathrm{T}}^2 + h^2) \tag{4.3}$$

$$0 < h < 2r_{\mathrm{s}} \tag{4.4}$$

where h is the height of the segment and A_{s} is the surface area of the spherical cap (Figure 4.3.A), derived from the steady state limiting current (*vide infra*). The starting point of **l** was the origin (black dot Figure 4.3.A), and the z component was derived from h and r_{s} using Equation (4.5):

$$\mathbf{l} = (0, h - r_{\mathrm{s}}) \tag{4.5}$$

The radius of the insulating quartz sheath is r_{g}. The bulk domain boundaries were sufficiently far from the electrode, so that they did not affect the results of the steady state simulations. Steady state mass transport (*i.e.*, $\partial c/\partial t = 0$ everywhere within the simulation domain) was assumed to occur only by diffusion, as described by Equation (4.6),

$$D\nabla^2 c = 0 \tag{4.6}$$

where D and c are the diffusion coefficient and the concentration of the electrochemical mediator, respectively. Fick's second law of diffusion describes how the concentration gradient at the electrode surface changes with time. The steady state condition is met when the change in the concentration gradient with respect to time is zero. The time at which the steady state condition is met is independent of the diffusion coefficient and concentration, rather it is determined by the electrode geometry.

The following boundary conditions are used for the reaction of the mediator at the surface of the spherical cap. We assume that the reaction is complete and instantaneous. When under mass transport controlled reduction or oxidation, the concentration of the mediator at the surface is always equal to 0. To facilitate the calculation of the concentration gradient at the spherical cap, the concentration has been set to 0 at the electrode surface, so that at zero distance from the electrode

$$c = 0 \tag{4.7}$$

and for the bulk domain at large ("infinite") distance from the electrode

$$c = c^* \tag{4.8}$$

with c^* the bulk concentration of the electrochemical mediator. The boundary condition given in Equation 4.7 was used only for constant potential measurements, as the surface concentration constantly changes in potentiodynamic techniques, making the boundary condition invalid.

The boundary condition for the insulating electrode sheath along the axis of symmetry from the apex of the spherical cap to the substrate surface, and on the substrate surface are defined by zero electroactive species flux at their surface,

$$\mathbf{n}.\mathbf{N} = 0 \tag{4.9}$$

where **n** and **N** were the normal unit vector and flux vector ($j = -D\nabla^2 c$) respectively. The i_{ss} was calculated with Equation (4.10),

$$i_{ss} = \int_0^L 2\pi r n F \mathbf{n}.\mathbf{N}\, dr \tag{4.10}$$

The limits for the integral, 0 and L, represent the point of contact of the spherical cap with the insulating sheath (*i.e.* at $r = r_t$), and the length of the arc to the intercept of the z axis.

4.4.4. INFLUENCE OF SPHERICAL CAP SIZE ON THE STEADY-STATE CURRENT

Simulations were performed to determine the bulk steady-state current for different sizes of spherical caps on a nanoelectrode with r_t = 25 nm and r_g = 250 nm, assuming a solution with concentration c^* = 1 mM and $D = 6.0 \times 10^{-6}$ cm^2 s^{-1} for the relevant ionic species. Figure 4.3.B displays the change in the normalized i_{ss} as a function of the electrode's normalized surface area. The current was normalized through division by the simulated current for a hemisphere electrode (*i.e., for* $r_s = r_T$), and the hemispherical cap surface area (A_s) was normalized through its division by the surface area of a hemispherical cap, referred to as "*hemisphere area ratio*". (Note that surface area of the hemispherical cap does not include the spherical base of the mercury in contact with the platinum electrode.) The dotted line indicates the experimental working range for hemisphere area ratios obtained with this deposition method, which ranged from 1 to 2. Note that as the hemispherical cap surface area increases, r_s and **l** change while r_t remains constant. Table 1 summarizes the values of these parameters, for improved clarity.

Figure 4.3.B shows that the i_{ss} increases as the hemisphere area ratio increases. The current increases non-linearly with surface area, because the insulating sheath causes hindered diffusion to the spherical cap for hemisphere area fractions greater than 1. These data provide a calibration curve to determine hemisphere area ratio, hence the quantity A_s of the spherical cap, based on the measured i_{ss} and the theoretical steady-state current for a hemispherical electrode of radius r_T (Equation 2.3, where $k = 2\pi$). r_s and l can be calculated by solving Equations (4.2), (4.3) and (4.4), thus providing a complete geometrical description of the mercury cap electrode.

Table 4.1. *Summary of Simulation Parameters and Steady-State Current Results Used in Figure 4.3.B.* For an electrode with a Pt disk electrode of r_t = 25 nm in a solution with where c^* = 1.0 mM and $D = 6.0 \times 10^{-6}$ cm^2 s^{-1}. HAR = Hemisphere area ratio.

HAR	**r_s (nm)**	**L (z component) (nm)**	**i_{ss} (pA)**	**$i_{ss}/i_{ss,hemisphere}$**
0.6	33.5	22.4	7.1	0.75
0.8	25.8	6.5	8.4	0.89
1	25	0	9.5	1

HAR	r_s (nm)	L (z component) (nm)	i_{ss} (pA)	$i_{ss}/i_{ss,hemisphere}$
1.2	25.3	-4.2	10.4	1.10
1.4	26.1	-7.5	11.3	1.19
1.6	27.0	-10.1	12.1	1.27
1.8	27.9	-12.4	12.9	1.35
2	28.9	-14.4	13.6	1.43
2.2	29.8	-16.3	14.3	1.50
2.4	30.8	-18.0	14.9	1.57
2.6	31.7	-19.5	15.6	1.64
2.8	32.6	-21.0	16.2	1.71
3	33.5	-22.4	16.8	1.77
4	37.8	-28.3	19.6	2.06
6	45.2	-37.7	24.4	2.57
10	57.4	-51.6	32.3	3.41

4.4.5. ANALYSIS OF EXPERIMENTAL DATA BY SIMULATION

To validate the size and geometry of the mercury spherical cap, we compared the steady-state limiting current and approach curves for experimental and simulated data. For the experimental data set shown in Figure 4.2.D the radius of the Pt electrode was calculated to be 207 nm using the i_{ss} of 74 pA using Equation 2.3, and from an approach curve analysis with r_g = 4.1 µm. Equation 2.3 predicted a steady-state current of 116 pA for a hemispherical electrode. The measured current response for the Hg capped electrode was 244 pA, which corresponds to an A_s value of 4.2. By solving Equations (4.2 to 4.4) we derived r_s = 319 nm and **l** = -243 nm. The simulation of the bulk current for these parameters yield a steady-state current of 244 pA, in excellent agreement with the experimental value.

Experimental and simulated approach curves towards an insulator surface are shown in Figure 4.3.D. The current response at a hemispherical electrode approaching an insulating substrate has been reported previously[33, 34]. As the electrodes reported herein are larger than a hemisphere, it was necessary to simulate the spherical cap approach curves (*vide supra*). For the experimental approach curve the spherical capped electrode was held at a potential of -0.8 V *vs.* Hg/Hg_2SO_4 (sat. K_2SO_4) to ensure the complete reduction of Ruhex(III) to Ruhex(II), and was approached towards the substrate surface at a speed of 0.5 µm s^{-1}. The simulation assumes that a steady-state diffusion controlled current has been reached at each z position.

A decrease in the magnitude of the steady-state current is observed as the spherical cap electrode approaches the insulating surface. We see a good agreement between the simulated and experimental data obtained for $z > 1$ µm. We attribute the deviation of the experimental and simulated data at shorter distances to the effect of substrate tilt on the approach, as the apex of the mercury was approximately 400 nm above the surface and the insulating sheath radius was 4.1 µm. Note that the tip-to-substrate separation was measured from the plane of the Pt UME/glass sheath to the substrate surface (Figure 4.3.A). Hence, these data support the combined experimental and simulated techniques for characterising the geometry of the spherical cap electrode.

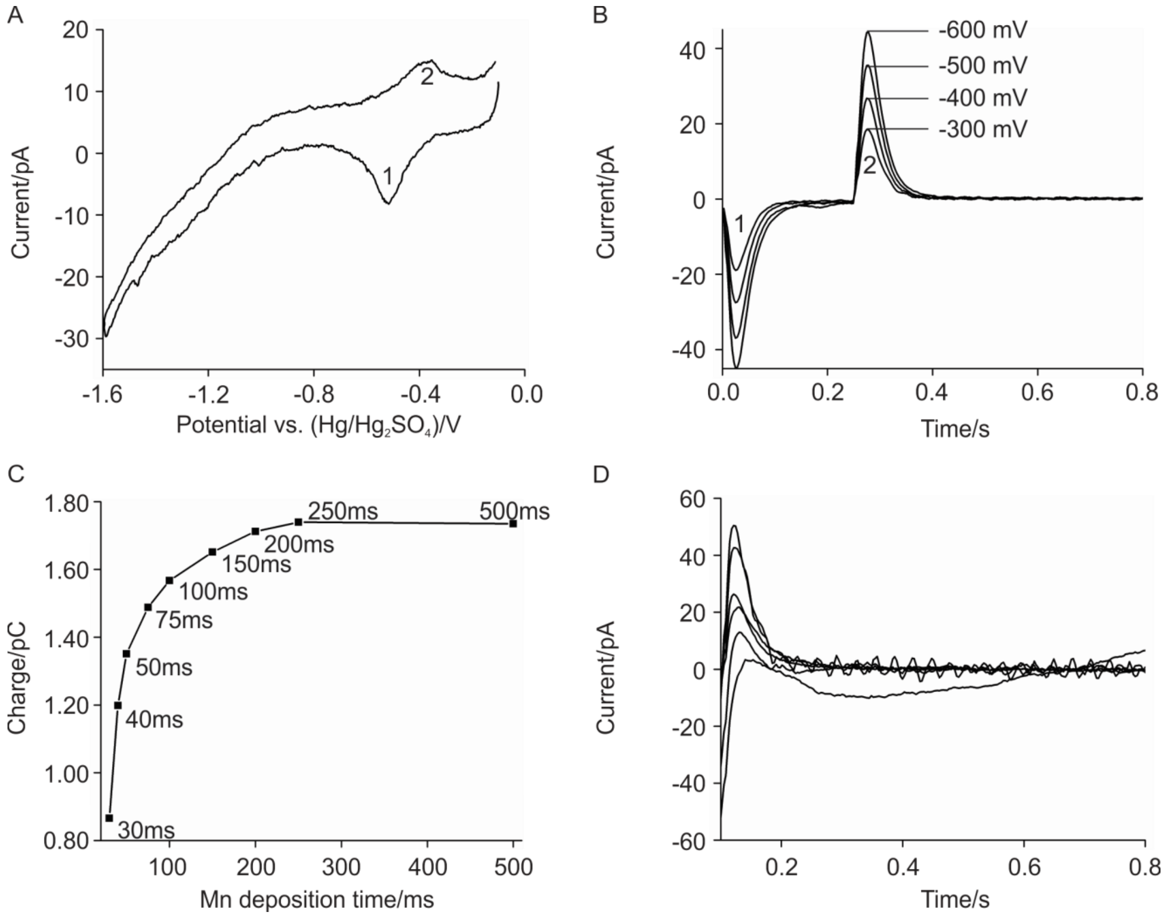

Figure 4.4. (A) CV for 10 µM manganese(II) nitrate solution. (B) Current *vs*. time plots for a 10 µM manganese(II) nitrate solution at different deposition potentials. (C) Charge *vs*. deposition time for the same 10 µM manganese(II) nitrate solution. (D) Successive additions of polymeric A15C5 ether to the 1 µM manganese(II) nitrate leads to corresponding decreases in peak currents and peak areas, i.e., decreased amounts of free Mn^{2+} cations in the solution. (D) shows the results from successive additions of a suspension of 10 mg 3 % cross-linked divinylbenzene vinylbenzyl-A15C5 or P(3% DVB-97% VBz-A15C5) in 0.1 M aqueous KNO_3 solution (to provide successive cumulative volumes of 10, 20, 30, 40 and 140 µL) added to 50.00 mL of a deoxygenated 1 µM manganese(II) nitrate solution.

The voltammetric behavior of Mn^{2+} was evaluated in a 10 µM manganese(II) nitrate in 0.1 M KNO_3 solution (Figure 4.4.A), to evaluate the amalgam formation potential (-500 mV) and the stripping potential (-350 mV) marked, respectively, with 1 and 2 in Figure 4.4. (A). The measurements were performed in 0.1 M KNO_3, in order to ensure that the two peaks in the CV were due to the oxidation and reduction of manganese, and not caused by background processes. (Appendix C Figure C.1 displays an overlay of 10 CVs show good reproducibility between the cycles.) Figure 4.4.B displays the effect of the deposition potential on the stripping response. The amplitude of the peak currents increases as the potential is stepped from -200 mV to -300, -400, -500 and -600 mV and held for 250 ms intervals. The stripping step was performed by stepping the potential back to -200 mV. As the deposition potential was made more negative, the charge of stripping peak increases.

Optimization of the deposition time was performed by integrating the charge in peak 2 for different deposition times in the 1 μM manganese(II) nitrate solution, as shown Figure 4.4.C. For deposition times shorter than 250 ms an increase in measured charge is observed for an increased deposition time, but the increase is non-linear. For deposition times greater than 250 ms there is no observable increase in stripping charge, because the mercury spherical cap becomes saturated with manganese at this particular concentration (see raw data in Figure C.3.A). Figure C.3.B and D in the Appendix C report the data obtained for the same probe in a 5 μM solution. In this case, the deposition time for saturation is smaller (100 ms) than for the 1 μM concentration.

We opted to use a potential step for the stripping process because the shape of the stripping peak in ASV is dependent upon scan rate. By using a potential step we use the rise time of the potentiostat to provide the maximum possible scan rate. Potential *vs.* time plots for the different deposition times are shown in Appendix C Figure C.4, recorded at the optimal deposition potential of -600 mV. During the stripping step, the rise time of the equipment provided a scan rate equivalent to *ca.* 5.5 V s^{-1}. This provided the highest available scan rate, hence the best signal to noise for the system.

These data indicate that the optimal deposition potential in a 1 μM manganese(II) nitrate solution is -600 mV for 100 ms deposition times. (Appendix C Figure C.2.B displays the results for the Hg(Mn) amalgam formation (peak 1) and Figure C.2.C shows the release of the Mn (peak 2); the plating to stripping charge ratio had a mean value of 1.08 ± 0.04 (standard deviation) for 12 successive plating-stripping cycles. This suggests that all the Mn deposited into the amalgam is removed during the stripping step.

Figure 4.4.D shows the results from successive additions of a suspension of 10 mg 3 % cross-linked divinylbenzene vinylbenzyl-A15C5 or P(3 % DVB-97 % VBz-A15C5) in 0.1 M aqueous KNO_3 solution (to provide successive cumulative volumes of 10, 20, 30, 40 and 140 μL) added to

50.00 mL of a deoxygenated 1 μM manganese(II) nitrate solution. The largest charge was recorded for the manganese solution before the addition of the crowns. The amount of Mn^{2+} detected decreased upon successive additions of polymeric azacrowns, due to the sequestration of Mn^{2+} cations. The diminution of the signal continued until the amount of azacrowns was sufficient to capture all the Mn^{2+} cations initially present in the solution. The choice of A15C5 was motivated by it performance in industrial testing of $LiMnO_4$–graphite batteries, compared to 18C6 or 14C4. The improved trapping efficiency of A15C5 compared to 18C6 or 14C4 in a Li-ion battery environment is due to the existence of a large permanent dipole moment in the former case, compared to its absence in the latter ones. Furthermore, it is well-established that (in the absence of an electric field) the dominant factor for effective trapping is a matching between the ion radius and the radius of the macrocyle cavity. For instance, 15C5 has a cavity radius of 0.86 – 0.92 Å [35] and entraps Mn^{2+} with a radius of 83 Å. [36]

4.5. CONCLUSIONS

We have reported a successful method for the fabrication of Hg/Pt nanoelectrodes using electrodeposition from a mercuric inorganic solution onto laser-pulled Pt/quartz disc nanoelectrode. Full coverage of the platinum by the mercury hemisphere cap was confirmed. The radii of the mercury hemisphere cap electrodes were determined by cyclic voltammetry and were between 6 and 500 nm, with a hemispherical area ratio ranging from 1 to 2. The electrochemical behavior of the spherical cap has been evaluated by steady-state voltammetry and approach curves over an insulating substrate. The data were analyzed by FEM modelling, to fully characterize the geometry of the spherical cap. The presence of the spherical cap was identified by ESEM images, with EDS confirming the presence of Hg on the probe. Preliminary detection of Mn^{2+} was achieved. Optimization of the deposition potential (-600 mV) and time (100 ms) for manganese detection was performed. The feasibility of using the developed Hg/Pt nanoelectrode for Mn^{2+} detection was demonstrated by measuring the decrease in the signal for Mn^{2+} upon successive additions of manganese trapping polymeric A15C5. The developed procedure creates the opportunity of using the probe as an SECM tip for the localized detection of manganese and other transition metal cations.

[1] M.W. Verbrugge, B.J. Koch, Journal of the Electrochemical Society, 141 (1994) 3053-3059.

[2] B.B. Katemann, W. Schuhmann, Electroanalysis, 14 (2002) 22-28.

[3] M.A. Mezour, M. Morin, J. Mauzeroll, Analytical Chemistry, 83 (2011) 2378-2382.

[4] Y. Li, D. Bergman, B. Zhang, Analytical Chemistry, 81 (2009) 5496-5502.

[5] L. Danis, M.E. Snowden, U.M. Tefashe, C.N. Heinemann, J. Mauzeroll, Electrochimica Acta, 136 (2014) 121-129.

[6] R.A. Lazenby, K. McKelvey, M. Peruffo, M. Baghdadi, P.R. Unwin, Journal of Solid State Electrochemistry, 17 (2013) 2979-2987.

[7] B.P. Nadappuram, K. McKelvey, R. Al Botros, A.W. Colburn, P.R. Unwin, Analytical Chemistry, 85 (2013) 8070-8074.

[8] J. Velmurugan, J.M. Noël, M.V. Mirkin, Chemical Science, 5 (2013) 189-194.

[9] J. Velmurugan, M.V. Mirkin, ChemPhysChem, 11 (2010) 3011-3017.

[10] D.C. Grahame, Journal of the American Chemical Society, 79 (1957) 2093-2098.

[11] S. Amokrane, J.P. Badiali, Journal of Electroanalytical Chemistry, 266 (1989) 21-35.

[12] T.M. Florence, Journal of Electroanalytical Chemistry, 27 (1970) 273-281.

[13] C.M.G. van den Berg, Analytica Chimica Acta, 250 (1991) 265-276.

[14] H.W. Chan, J.G. Duh, S.R. Sheen, Journal of Power Sources, 115 (2003) 110-118.

[15] X.C. Tang, B.Y. Huang, Y.H. He, Transactions of Nonferrous Metals Society of China (English Edition), 16 (2006) 438-444.

[16] Y.K. Sun, Y.S. Jeon, H.J. Lee, Electrochemical and Solid-State Letters, 3 (2000) 7-9.

[17] M. Wohlfahrt-Mehrens, C. Vogler, J. Garche, Journal of Power Sources, 127 (2004) 58-64.

[18] A. Du Pasquier, A. Blyr, P. Courjal, D. Larcher, G. Amatucci, B. Gérand, J.M. Tarascon, Journal of the Electrochemical Society, 146 (1999) 428-436.

[19] Y. Xia, Y. Zhou, M. Yoshio, Journal of the Electrochemical Society, 144 (1997) 2593-2600.

[20] M.M. Thackeray, Progress in Solid State Chemistry, 25 (1997) 1-71.

[21] Y. Kim, J. Lim, S. Kang, International Journal of Quantum Chemistry, 113 (2013) 148-154.

[22] T.F. Yi, Y.R. Zhu, X.D. Zhu, J. Shu, C.B. Yue, A.N. Zhou, Ionics, 15 (2009) 779-784.

[23] W. Choi, A. Manthiram, Journal of the Electrochemical Society, 153 (2006) A1760-A1764.

[24] C. Li, H.P. Zhang, L.J. Fu, H. Liu, Y.P. Wu, E. Rahm, R. Holze, H.Q. Wu, Electrochimica Acta, 51 (2006) 3872-3883.

[25] X. Meng, X.Q. Yang, X. Sun, Advanced Materials, 24 (2012) 3589-3615.

[26] B. Ziv, N. Levy, V. Borgel, Z. Li, M.D. Levi, D. Aurbach, A.D. Pauric, G.R. Goward, T.J. Fuller, M.P. Balogh, I.C. Halalay, Journal of the Electrochemical Society, 161 (2014) A1213-A1217.

[27] Z. Li, A.D. Pauric, G.R. Goward, T.J. Fuller, J.M. Ziegelbauer, M.P. Balogh, I.C. Halalay, Journal of Power Sources, (2014).

[28] C.S. Kim, S.H. Kwon, J.W. Yoon, Journal of Alloys and Compounds, 586 (2014) 574-580.

[29] D. Aurbach, M.D. Levi, K. Gamulski, B. Markovsky, G. Salitra, E. Levi, U. Heider, L. Heider, R. Oesten, Journal of Power Sources, 81-82 (1999) 472-479.

[30] J. Mauzeroll, E.A. Hueske, A.J. Bard, Analytical Chemistry, 75 (2003) 3880-3889.

[31] D. Rudolph, S. Neuhuber, C. Kranz, M. Taillefert, B. Mizaikoff, Analyst, 129 (2004) 443-448.

[32] S. Daniele, I. Ciani, D. Battistel, Analytical Chemistry, 80 (2008) 253-259.

[33] Y. Selzer, D. Mandler, Analytical Chemistry, 72 (2000) 2383-2390.

[34] G. Lindsey, S. Abercrombie, G. Denuault, S. Daniele, E. De Faveri, Analytical Chemistry, 79 (2007) 2952-2956.

[35] J.D. Lamb, R.M. Izatt, C.S. Swain, J.J. Christensen, Journal of the American Chemical Society, 102 (1980) 475-479.

[36] R.D. Shannon, Acta Crystallographica., 32 (1976) 751-767.

CHAPTER 5: DETECTION OF MANGANESE IONS IN A WATER AND OXYGEN-FREE ENVIRONMENT USING MERCURY-AMALGAM NANOELECTRODES FOR APPLICATION IN LI-ION BATTERIES

In recent years, LIB characterization has become a hot topic in the field of SECM. As it gained importance, SPM specialists faced the challenge of the air-sensitive nature of these materials. Progress in SECM has rendered its use in an argon-filled glovebox to address fundamental questions relative to LIB technology development. As mentioned in Chapter 1, the SECM system in a glove box has so far been used to investigate lithium transport, electronic properties, leaching and topography, as well as the formation and electrochemical properties of SEI and defect formation on SEI.

Hg-based ASV for the detection of metal ion dissolution in aqueous solution has been investigated in Chapter 4. Chapter 5 focuses on operating this technique for the detection of Mn^{2+} in non-aqueous conditions (LIB electrolyte) in a water and oxygen free environment (a glovebox filled with argon O_2 and H_2O below 1 ppm). The technique to produce Hg/Pt nanoelectrodes presented in Chapter 4 has been adapted in order to produce and characterize them directly inside the glovebox. This step is of importance because, considering the fragile nature of the nano-sized Hg hemisphere and the Hg vapor pressure, passing the probe in the vacuum chamber of the glovebox could potentially be detrimental to the probe. Reducing the vacuum time or the number of purging cycles in order to guarantee the integrity of the probe could be harmful to the inert atmosphere of the glovebox. Therefore, being able to fabricate and characterize them in the glovebox is valuable. Chapter 5 presents the preliminary data obtained, where the Hg-based ASV has been used to investigate the prospective use of polymeric A15C5 as a chelating agent to capture Mn^{2+} in LIBs.

5.1. ABSTRACT

The work presented here describes the fabrication and characterization of mercury-capped platinum nanoelectrodes in an oxygen and water-free environment. The nanoelectrodes were employed as manganese (Mn) amperometric detectors in order to determine the ability of Mn specific chelating agents to capture the cations in concentrated manganese solutions in propylene carbonate (PC) $LiClO_4$, a typical a non-aqueous electrolyte for Li-ion batteries (LIBs). The Hg/Pt nanoelectrodes were fabricated by electrodeposition from a mercuric ion solution onto Pt/quartz laser-pulled disk nanoelectrodes. Steady-state voltammetry was used for nanoelectrode characterization.

5.2. INTRODUCTION

Manganese-rich oxides such as lithium manganese oxide *spinel* $Li_xMn_2O_4$ (LMO) is a promising positive electrode material for high-power LIBs. LMO is known for its low cost, thermal safety, low toxicity, good rate performance, and high theoretical specific capacity (148 mAh g^{-1}), comparable to $LiCoO_2$ (140 mAh g^{-1}). In comparison with $LiCoO_2$, LMO has a higher average potential. LMO has two charge / discharge plateaus at 3.95 and 4.15 V (*vs.* Li^+/Li).[1, 2] However, the commercialization of LMO is hindered due to severe capacity fading and increase in cell resistance.[3]

This poor capacity retention has been mainly attributed to the leaching of Mn cations from the *spinel* into the electrolyte, induced by the hydrogen fluoride (HF) present in the electrolyte,[4, 5] following the charge disproportion reaction Equation 4.1 presented in Chapter 4:[6]

Not only is Mn leaching from the *spinel* detrimental to the battery performance because of the loss of active material, but furthermore, past a certain concentration threshold of dissolved Mn cations, it is also known to have an impact on the negative electrode performance. Mn cations are known to electro-migrate to the negative electrode where the reduction of Mn to its metallic form occurs at the surface. This leads to electrolyte decomposition and film growth, causing capacity fading, reduced power performance and overall reduction in LIB life.

Recent advances to alleviate the negative consequences of Mn cation dissolution in LIBs led to the use of crown ethers, which are well-known for binding favourably to specific metals, and can be tethered to polymers coated on battery separators to chelate manganese (Figure 5.1.). This technique prevents the Mn ions from electro-migrating from the positive to the negative electrode.[7, 8]

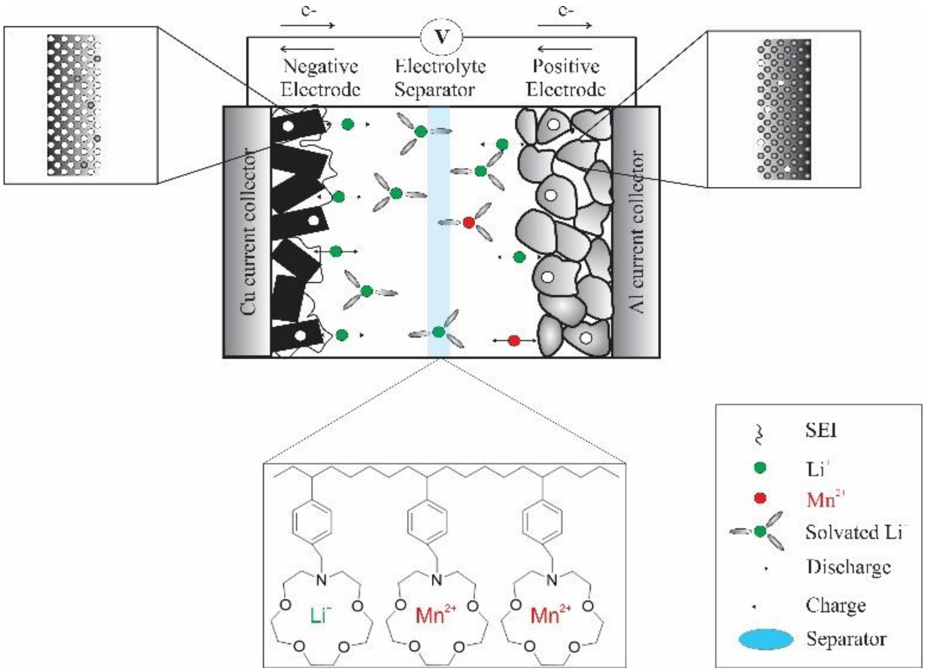

Figure 5.1. Schematic representation of polymeric A15C5 tethered to a battery separator chelating Mn^{2+}

Standard LIB characterization techniques are performed *ex-situ* post cell disassembly, and therefore have the potential risk of data alterations due to the air sensitive nature of these materials. This creates a need for a real time *in-situ* and *in-operando* technique on battery materials.

In this chapter we investigate the use of ASV performed with Hg/Pt nanoelectrodes to give new insight into the capacity fading mechanism of $Li_xMn_2O_4$ and on the efficiency of the proposed method to counteract the manganese dissolution. We previously described a Hg-based ASV experiment that has the potential to perform quantitative *in-situ* detection of manganese ions. However, until now the experiment was still performed as a proof-of-concept in aqueous solutions. In an aqueous environment, the polymeric A15C5 performed extremely well with respect to sequestering Mn^{2+} where the measured trapping site occupancy was close to 100% (Figure 5.2.).

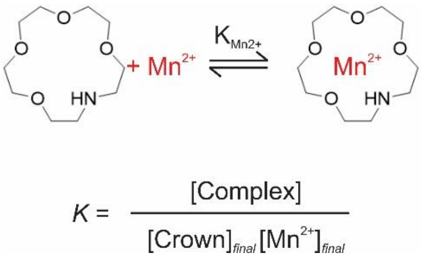

Figure 5.2. Schematic of A15C5 binding favorably to Mn^{2+}. The binding affinity is mostly dependent on the diameter of metal and the cavity diameter of the crown ether, but is also dependent on the presence or absence of a dipole moment

The superior trapping efficiency of A15C5 was attributed to the presence of a large permanent dipole.[9] In the absence of an electric field, the leading cause for effective chelating is a correspondence between the ion diameter and the diameter of the crown ether cavity. For instance, as seen in Table 5.1, A15C5 has a cavity diameter of 1.7-2.2 Å[10] and chelates Mn^{2+} with a diameter of 1.66 Å.[11]

Table 5.1. - *Comparison Between Effective Ionic Diameters and Crown Ether Cavity Diameters*

Metal	Li^{+}	Mn^{2+}	Mn^{3+}	Mn^{4+}
Diameter (Å)	1.56	1.66	1.29	1.06
Crown ether	12-crown-4	15-crown-5	1-aza-15-crown-5	18-crown-6
Cavity Diameter (Å)	1.2-1.5	1.7-2.2	1.7-2.2	2.6-3.2

Recent studies have shown that it is very likely that Mn^{2+}, Mn^{3+} and Mn^{4+} coexist in the electrolyte solution after charge-discharge cycling. In contradiction to what is normally believed, they have demonstrated that the average oxidation state of manganese cations present in electrolyte solutions could be closer to +3 than +2. A15C5 crown ether has been studied in a lithium-containing environment using NMR through the ^{7}Li nucleus chemical shift to evaluate its relative binding affinities to Mn^{2+} and Mn^{3+}. They have shown that Mn^{2+} has an equilibrium constant more than 100x greater than Li^+. However, they have shown a decreased affinity for the Mn^{3+} to polymeric A15C5 relative to lithium.[12]

Recent advances in SECM have now allowed its use in a water and oxygen-free environment provided by a glovebox [13-23] or analogous setup. This process will allow one to perform characterization of LIBs materials measurements in a more realistic setup (*i.e.* a water and oxygen free environment, in real battery electrolyte).

Herein we report the development of mercury-capped platinum nanoelectrodes for the quantitative detection of manganese ions. The hemispherical mercury caps were electroplated onto Pt nanoelectrodes in a 0.2 M $LiClO_4$/ PC solution directly inside the glovebox. The Hg/Pt nanoelectrodes were characterized by steady state electrochemical measurements. ASV, was used to detect dissolved manganese ions in battery electrolyte. Furthermore, the technique was employed to obtain promising preliminary data on the capture of manganese by the crown ethers in a battery-like environment.

5.3. EXPERIMENTAL

5.3.1 MATERIALS AND REAGENTS

The platinum wires (0.01 mm and 0.025 mm diameter; purity: 99.99 %; temper: hard) were acquired from Goodfellow (U.K.). The quartz glass capillaries (L: 10 cm; O.D.:1.0 mm; I.D.:0.50 mm) and borosilicate capillaries (L.: 75 mm; O.D.:2.0 mm; I.D.:1.16 mm) were purchased from Sutter Instruments (U.S.A). The abrasive polishing disks (4000 grit) and alumina powder (0.05, 0.1, 0.3, 1.0 μm particle diameter) were bought from Struers (Mississauga, Canada). The electrically conductive silver epoxy (EPO-TEK H20E) and gold connector pins were purchased from Epoxy Technology (U.S.A) and Heka (U.S.A) respectively. Argon (>99.998 %) used to create an oxygen and water-free environment inside of the glovebox was purchased from Praxair.

Methyl viologen dichloride hydrate (MV), propylene carbonate (PC), lithium perchlorate anhydrous, ferrocenemethanol, mercury (II) chloride, manganese (II) chloride and manganese (III) fluoride were purchased from Sigma Aldrich (Oakville, Canada). The 3 % cross-linked divinylbenzene vinylbenzyl-A15C5 (3 % DVB-97 % VBz-A15C5) was synthesized in-house at GM R&D.

5.3.2. APPARATUS

The platinum disk nanoelectrodes were fabricated using a P-2000 laser-based micropipette puller system (Sutter Instruments, U.S.A) and a vacuum pump (Edwards RV8, Edwards, Canada). The platinum surface was exposed and polished using a Tegrapol 23 variable speed polisher (Struers, Canada). All scanning electrochemical measurements were performed using an Electrochemical Probe Scanner ELP1 (HEKA Elektronik, Germany) in a two electrode setup. All potentials were recorded relative to a Li/Li^+ reference electrode, unless specified otherwise. All oxygen sensitive experiments were performed under an argon atmosphere inside of a LABstar glovebox with a MB-10-G gas purifier (mBRAUN, U.S.A).

5.3.3. FABRICATION OF PLATINUM NANOELECTRODES AND DEPOSITION OF MERCURY UNDER INERT ATMOSPHERE

The platinum disk nanoelectrodes were produced using a pre-establish laser-pulled technique.[24] After fabrication, the nanoelectrodes were introduced inside the glove box. Similar to previously reported, the Hg/Pt hemispherical nanoelectrodes were obtained by electrodeposition from a 10 mM $HgCl_2$ solution in 0.2 M $LiClO_4$/ PC. The electrochemical deposition of Hg was performed at a potential of 2.7 V *vs.* Li/Li^+ until the current reached $\pi/2$ (~1.57) times the initial current of the disk nanoelectrode.

5.3.4. ELECTROCHEMICAL MEASUREMENTS

The size of the electroactive surface and the electrochemical behavior of the nanoelectrodes were characterized by cyclic voltammetry. A 1 mM methyl viologen (MV^{2+}) redox couple solution in 0.2 M $LiClO_4$/ PC was used for both Pt and Hg/Pt nanoelectrode measurements. For cyclic voltammetry (CV) using MV^{2+}, the potential was varied linearly from 1.8 V to 3 V *vs.* Li/Li^+ using a scan rate of 10 mV s^{-1}. The diffusion coefficient of MV^{2+} in 0.2 M $LiClO_4$/ PC was determined by CV using well characterized 25 μm microelectrodes with controlled geometry. The microelectrodes used to characterized MV^{2+} were produce using a pre-established technique.[25]

5.4. RESULTS AND DISCUSSION

5.4.1. PLATINUM DISK ULTRAMICROELECTRODE CHARACTERIZATION

In the initial stage of this project presented in Chapter 4, the nanoelectrodes were produced in a deaerated aqueous solution and were characterized by steady-state voltammetry, ESEM and EDS. Due to the sensitivity of the samples, the experiment was relocated into a glovebox where only steady-state voltammetry could be utilized for characterization. Several options were considered for use as a redox mediator for this characterization. They were evaluated by their ability to be inserted into a glove box, electrochemical properties, solubility in PC and stability. After testing cobalt (III) sepulchrate trichloride, Ruhex and methyl viologen, methyl viologen was chosen considering its solubility in PC and electrochemical properties.

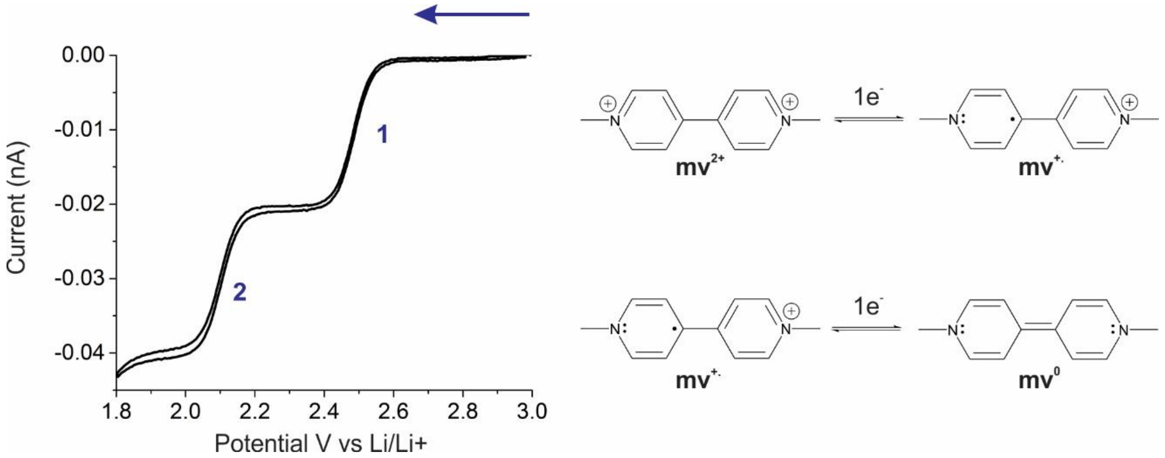

Figure 5.3. Characterization of disk Pt nanoelectrodes. Experimental CV for a Pt UME (r_t = 215 nm), performed using 1 mM MV^{2+} in 0.2 M $LiClO_4$/ PC at 10 mV s^{-1}. The second recorded cycle is shown. The arrow indicates the scanning direction.

The reduction of MV^{2+} is a two-step one electron fully reversible electrochemical process as shown in Figure 5.3 and described by Equations 5.1 and 5.2

$$\mathrm{MV^{2+} + e^- \leftrightarrow MV^+} \qquad \mathrm{E = 2.5\ V}\ \mathit{vs.}\ \mathrm{Li/Li^+} \tag{5.1}$$

$$\mathrm{MV^{+} + e^- \leftrightarrow MV} \qquad \mathrm{E = 2.1\ V}\ \mathit{vs.}\ \mathrm{Li/Li^+} \tag{5.2}$$

The CV displayed in Figure 5.3 exhibits a double sigmoidal shape and achieves a first diffusion-limited steady-state current for the reduction of MV^{2+} to MV^+ when a potential of between 2.5 to 2.1 V *vs.* Li/Li^+ is applied. The second diffusion-limited steady-state current for the reduction of MV^+ to MV^0 is achieved when a potential of 2.1 (or more negative) V *vs.* Li/Li^+ is applied for both Pt and Hg/Pt nanoelectrodes. Under diffusion control, the i_{ss} is given Equation 2.3 in Chapter 2. Where in this case, k is a geometric constant (Disk: k = 4; Hemispherical: k = 2π), n is the number of electrons involved in the reaction (1 per step), D is the diffusion coefficient of the redox species extracted from the experimental data and Equation 2.3 ($D_{MV^{2+}}$ = 2.28 x 10^{-6} cm^2 s^{-1}), and F, r_T, and c^* are the as presented in Chapter 2.

5.4.2. MERCURY / PLATINUM HEMISPHERICAL ULTRAMICROELECTRODE CHARACTERIZATION

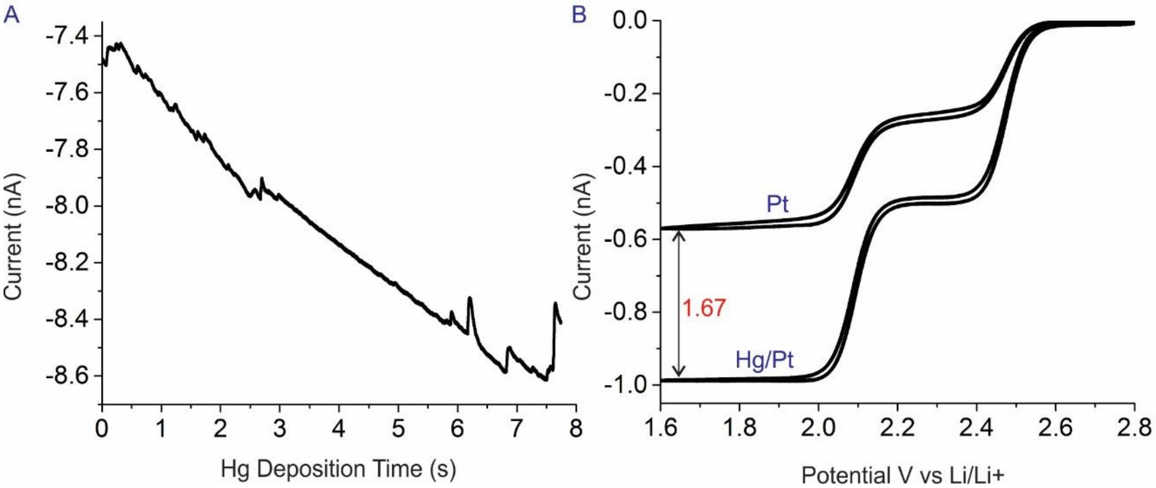

Figure 5.4. (A) Current response from Hg deposition onto the Pt nanoelectrode and growth of the spherical cap, where a potential of 2.7 V *vs.* Li/Li^+ was held for 8 s. (B) Experimental voltammetric behavior of a Pt nanoelectrode (r_T = 2.71 μm) before and after deposition of a Hg spherical cap in 1 mM MV^{2+} in 0.2 M $LiClO_4$ at a scan rate of 10 mV s^{-1}.

Hg spherical caps were grown onto disk nanoelectrodes using electrochemically-controlled deposition (Figure 5.4.A). Similar to the deposition in aqueous media, the deposition in PC occurs in three different stages. In the first stage, a thin layer Pt_2Hg forms. In the second stage, Hg nucleates, followed by the third stage where the nuclei coalesce and the spherical cap grows. Figure 5.4.B displays the electrochemical behavior resulting from the change in geometry from disk to and hemisphere. According to Equation 2.3, the change in geometry results in a steady-state increase of π/2 ($i_{ss,\ hemisphere}$ / $i_{ss,\ disk}$ = 2π/4 = 1.57).

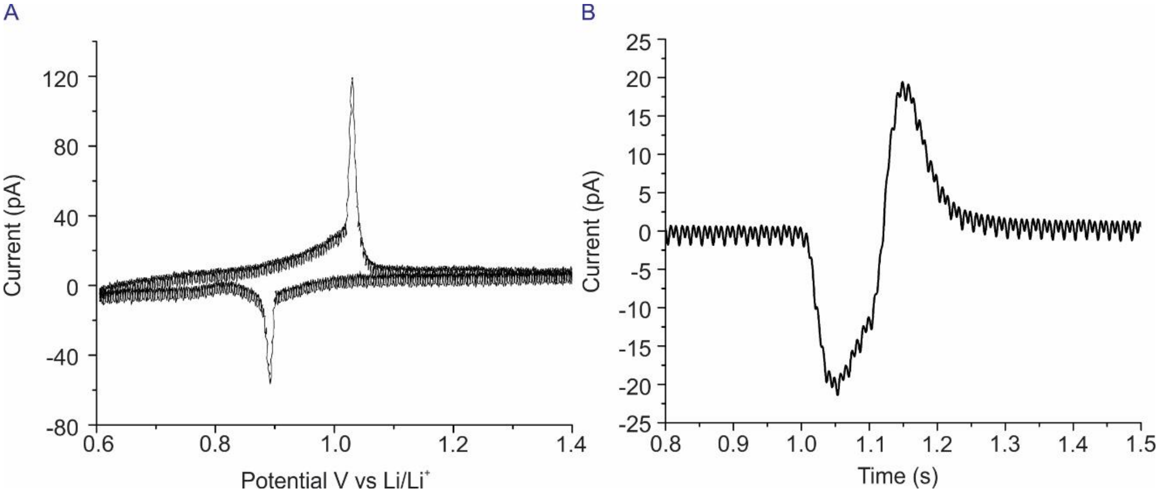

Figure 5.5. (A) Experimental voltammetric behavior of a nanoelectrode after deposition of a Hg spherical cap in 476.8 μM Mn^{2+} in 0.2 M $LiClO_4$ at a scan rate of 250 mV s^{-1}. (B) Experimental anodic stripping voltammetry behavior in the same solution. The deposition time was set as 100 ms and the stripping time to 1s.

The voltammetric behavior of Mn^{2+} was assessed in a 476.8 μM manganese (II) chloride in 0.2 M $LiClO_4$/ PC solution, in order to evaluate both the potential at which the amalgam forms 0.9V and the stripping potential 1.03 V *vs.* Li/Li^+, which can be seen in Figure 5.5.A. To ensure that the two peaks in the CV are exclusively attributed to the manganese oxidation and reduction, and not caused by any background processes, CVs were recorded in the 0.2 M $LiClO_4$/ PC electrolyte solution. The CV displays no significant signal in the Mn^{2+} potential region. Another CV was recorded in MV^{2+} after Mn^{2+} measurements and background measurements. This CV displayed the same i_{ss} as was seen in Figure 5.4.B, demonstrating that the mercury spherical cap was still intact and that the Hg depletion potential was not reached during the course of these experiments.

Figure 5.5.B display the experimental anodic stripping voltammetry behavior in the same solution. The deposition time was set as 100 ms and the stripping time to 1 s. Figure 5.6 displays the optimization of the experimental anodic stripping voltammetry behavior. The deposition time was increased from 10 to 100 ms, and the stripping time was set to a constant value of 1 s. Figure 5.6A displays the expected clear increase in current with deposition time. At deposition times above 125 ms distortion from saturation was observed, therefore an optimal deposition time 100 ms was used

in supplementary studies presented in Figure 5.7. Experimental conditions such as the solution concentration and the deposition time of Mn should be controlled to maintain linearity with increased loading of manganese. The occurrence of saturation, linked to the solubility limit of Mn in Hg, is of concern in ASV to avoid distortion from saturation. Figure 5.6.B displays the integrated deposition peak *vs.* the manganese deposition time in its linear response region (10 to 100 ms) $R^2 = 0.9798$. Figure 5.6.C shows the integrated stripping peak *vs.* the manganese deposition time in its linear response region $R^2 = 0.9670$. The average deposition to stripping charge to charge ratio was calculated to be 1.07 ± 0.24.

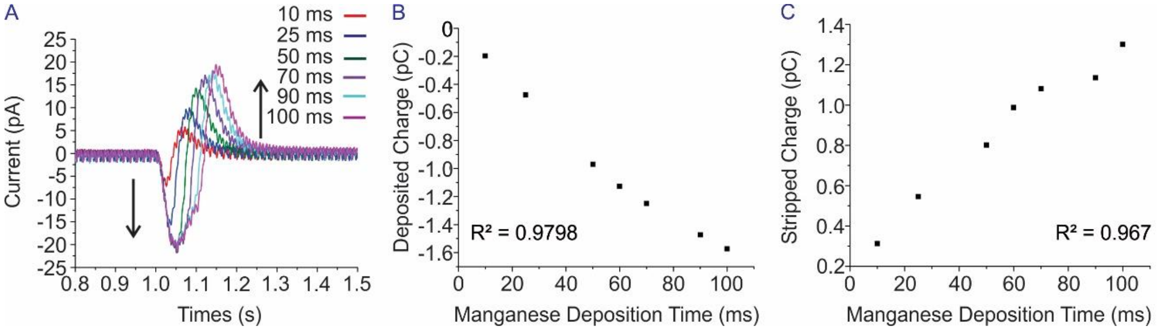

Figure 5.6. (A) Optimization of the experimental anodic stripping voltammetry behavior. The deposition time was increased from 10 ms to 100 ms and the stripping time stayed constant at 1 s. (B) Integrated deposition peak *vs.* the manganese deposition time in its linear response region $R^2 = 0.9798$. (C) Integrated stripping peak *vs.* the manganese deposition time in its linear response region $R^2 = 0.9670$. The average deposition to stripping charge to charge ratio is 1.07 ± 0.24.

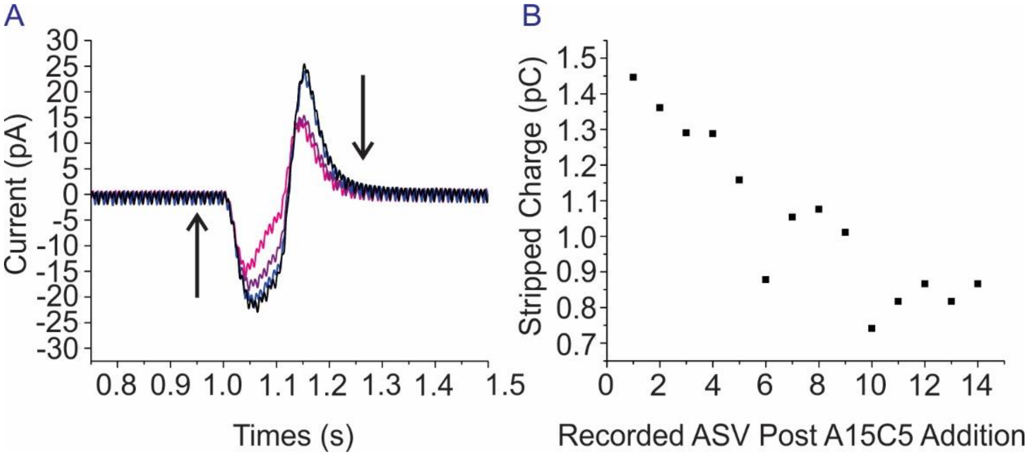

Figure 5.7. (A) Experimental Mn^{2+} ASV behavior after addition of 0.0143 g of A15C15 to a 476.8 μM Mn^{2+} in 0.2 M $LiClO_4$ in PC solution. The deposition time was 100 ms and the stripping time was 1 s. A clear decreasing trend can be observed over time (B) Integrated stripping peak *vs.* consecutive scan number $R^2 = 0.6751$. The average deposition to stripping charge to charge ratio is 1.28 ± 0.41. No confidence interval has been calculated as this is a preliminary single measurement.

Recent studies have revealed a clear improvement in capacity retention of batteries when trapping agents such as crown ethers are placed in the interelectrode space. Usually, these chelating agents are coated on or integrated in the separator. In this study we used free polymeric A15C5, which are known to be insoluble in propylene carbonate, in a static Mn^{2+} PC $LiClO_4$ solution. Figure 5.7 displays the experimental AVS with the optimized conditions from the previous section (deposition time 100 ms and stripping time 1 s) and shows the behavior of the Mn^{2+} solution post addition of 0.0143 g of A15C15 to 25ml of 476.8 μM Mn^{2+} in 0.2 M $LiClO_4$ in PC. The inhomogeneous suspension of crown ethers had differently sized agglomerates. This means that the ease of access for Mn^{2+} to the macrocycles was uncertain, and so the trapping efficiency was therefore not evaluated. Although the result presented in Figure 5.7.A and B are preliminary at this time, a clear trend is demonstrated in which we observed that the availability of Mn^{2+} is decreasing as it is being trapped with time by the macrocycle. As a result we detected a decrease in the area under the stripping peak.

5.5. CONCLUSIONS

In summary, the previous chapters focused on the fabrication and characterization of mercury-capped platinum nanoelectrodes in an oxygen and water-free environment. The nanoelectrodes were employed as Mn amperometric detectors to investigate the trapping effectiveness of polymeric A15C5 in PC $LiClO_4$ to capture Mn^{2+}. A clear decrease in the accessibility of the manganese cations was observed, which is attributed to the Mn^{2+} being chelated by the polymeric A15C5.

In an effort to improve the real world application and quantitative aspect of the experiment, future work will lead to the development of a specially designed flow device. This will flow manganese solution through the coated separators with a known pressure, simulating a real battery environment. This Hg-based ASV technique, combined with the sensitivity of the nano-sized probes and the SF-SECM mapping, will provide a localized quantitative evaluation of the trapping site occupancy, trapping efficiency and the release of manganese cations of these crown ethers.

In light of the recent XANES experiments performed by our industrial partner and one of our collaborating groups, which suggested that Mn^{3+} and Mn^{4+} are likely to be present with Mn^{2+} in the electrolyte solution after cell cycling, the efficiency of the crowns towards these oxidation states of manganese should also be determined. Another avenue for the technique would be to evaluate the competitive ion effect of all oxidation states of manganese and Li^+.

5.6. ACKNOWLEDGEMENTS

This work was financially supported by General Motors and the Natural Sciences and Engineering Research Council of Canada (CRSNG). The authors thank Michael Edward Snowden for the conception of the SECM integrated in a glovebox. We also acknowledge the members of Pr. Mauzeroll’s group at McGill University and the members of Pr. Schougaard’s group at UQAM for helpful discussions and contributions in this research project.

[1] H.W. Chan, J.G. Duh, S.R. Sheen, Journal of Power Sources, 115 (2003) 110-118.

[2] X.C. Tang, B.Y. Huang, Y.H. He, Transactions of Nonferrous Metals Society of China (English Edition), 16 (2006) 438-444.

[3] G.G. Amatucci, C.N. Schmutz, A. Blyr, C. Sigala, A.S. Gozdz, D. Larcher, J.M. Tarascon, Journal of Power Sources, 69 (1997) 11-25.

[4] Y. Kim, J. Lim, S. Kang, International Journal of Quantum Chemistry, 113 (2013) 148-154.

[5] T.F. Yi, Y.R. Zhu, X.D. Zhu, J. Shu, C.B. Yue, A.N. Zhou, Ionics, 15 (2009) 779-784.

[6] M.M. Thackeray, Progress in Solid State Chemistry, 25 (1997) 1-71.

[7] Z. Li, A.D. Pauric, G.R. Goward, T.J. Fuller, J.M. Ziegelbauer, M.P. Balogh, I.C. Halalay, Journal of Power Sources, 272 (2014) 1134-1141.

[8] B. Ziv, N. Levy, V. Borgel, Z. Li, M.D. Levi, D. Aurbach, A.D. Pauric, G.R. Goward, T.J. Fuller, M.P. Balogh, I.C. Halalay, Journal of the Electrochemical Society, 161 (2014) A1213-A1217.

[9] L. Danis, S.M. Gateman, M.E. Snowden, I.C. Halalay, J.Y. Howe, J. Mauzeroll, Electrochimica Acta, 162 (2015) 169-175.

[10] J.D. Lamb, R.M. Izatt, C.S. Swain, J.J. Christensen, Journal of the American Chemical Society, 102 (1980) 475-479.

[11] R.D. Shannon, Acta Crystallogr., 32 (1976) 751-767.

[12] A.D. Pauric, S. Jin, T.J. Fuller, M.P. Balogh, I.C. Halalay, G.R. Goward, Journal of Physical Chemistry C, 120 (2016) 3677-3683.

[13] Z.J. Barton, J. Rodríguez-López, Analytical Chemistry, 86 (2014) 10660-10667.

[14] G. Zampardi, E. Ventosa, F. La Mantia, W. Schuhmann, Electroanalysis, 27 (2015) 1017-1025.

[15] G. Zampardi, E. Ventosa, F. La Mantia, W. Schuhmann, Chemical Communications, 49 (2013) 9347-9349.

[16] G.A. Snook, T.D. Huynh, A.F. Hollenkamp, A.S. Best, Journal of Electroanalytical Chemistry, 687 (2012) 30-34.

[17] H. Bülter, F. Peters, J. Schwenzel, G. Wittstock, Journal of the Electrochemical Society, 163 (2016) A27-A34.

[18] G. Zampardi, F. La Mantia, W. Schuhmann, RSC Advances, 5 (2015) 31166-31171.

[19] G. Zampardi, F. La Mantia, W. Schuhmann, Electrochemistry Communications, 58 (2015) 1-5.

[20] J. Hui, M. Burgess, J. Zhang, J. Rodríguez-López, ACS Nano, 10 (2016) 4248-4257.

[21] H. Bülter, F. Peters, J. Schwenzel, G. Wittstock, Journal of the Electrochemical Society, 162 (2015) A7024-A7036.

[22] H. Bülter, P. Schwager, D. Fenske, G. Wittstock, Electrochimica Acta, 199 (2016) 366-379.

[23] H. Bülter, F. Peters, J. Schwenzel, G. Wittstock, Angewandte Chemie International Edition, 53 (2014) 10531-10535.

[24] L. Danis, M.E. Snowden, U.M. Tefashe, C.N. Heinemann, J. Mauzeroll, Electrochimica Acta, 136 (2014) 121-129.

[25] L. Danis, D. Polcari, A. Kwan, S.M. Gateman, J. Mauzeroll, Analytical Chemistry, 87 (2015) 2565-2569.

CHAPTER 6. SUMMARY, CONCLUSION AND SUGGESTIONS FOR FUTURE DIRECTIONS

This thesis is aimed at investigating SPM-based methods to provide nanoscale *in-situ* and *in-operendo* information to further our understanding of LIB electroactive components (i.e. fundamental mechanisms, processes and degradation). The previous chapters aimed at developing new electrochemical tools for the characterization and quantitative detection of Mn^{2+} cations leaching from positive electrode material, and for the evaluation of Mn^{2+} chelating agents. A summary of the work presented in all chapters of this thesis is discussed *vide infra* with suggestions for future directions for each chapter and strategies that could potentially improve the use of SECM for the field of LIBs.

Chapter 1 explored the potential of SPM-based methods to address the evolving need for characterization of LIBs. In this chapter, the LIB was dissected by component (i.e. positive electrode, negative electrode and SEI). For each of these constituent parts, this chapter put emphasis on SPM based-methods that have applications and prospective applications to further our understanding of LIB nanoscale electrochemical functionalities, degradation and aging mechanisms. Due to space limitations in the selected journal, Chapter 1 focused only on the electroactive components of the LIB. However, SPM based-methods have also been successfully applied to characterize separators as well as solid polymer electrolytes (SPE). For example, *ex-situ* AFM is a key technique for the detailed morphological characterization (i.e. apparent pore size, porosity, specific surface area, structure and roughness) of new types of membrane or modified separator. Morphological characterization at the nanoscale is of special interest for the LIBs community, as tuning the porous structure of composite separators could have a significant impact in facilitating the electrolyte wettability and ionic conductivity, and decreasing the thermal shrinkage, all of which has the potential to improve the cell performance.[1-3] The surface morphology of SPE films is also routinely investigated by *ex-situ* AFM to gain information about the membrane porosity,[4,5] thickness,[6] roughness,[4-6] or to obtain the difference in hardness in polymer segments at the nano-scale. [7] The characterization of the porosity of SPEs is of significance as the presence of a greater porosity in SPEs is associated with an increase in ionic conductivity. Improving the interfacial contact and adhesion energy is a prime concern when considering SPE, predominantly because of the volume variation in cathode material during Li (de-) insertion.[8] Surface roughness and morphology have an impact on the adhesion between the electrolyte and the electrode material: the more rough a surface, the better the adhesion will be due to the increase in interfacial contact area. [9] AFM can also been used to probe the distribution of ceramic particle filler added to the polymer electrolyte to increase the conductivity and mechanical stability, which are always prime preoccupations of the LIB community.[5] Moreover, SPEs are often composed of polymer with different domains, regions or segments of different hardness and degree of crystallinity, which all have an impact on ionic conductivity.[5] AFM can be used to image and confirm these microphase-separated morphologies.[10] In conclusion, SPM based-methods can improve our understanding of electroactive components (i.e. the positive and negative electrodes), the SEI but also non-electroactive components (i.e. the separator and SPEs).

Chapter 2 presented a new fabrication process for the production of UMEs. More specifically, we developed a simple, low cost, fast, and reproducible production technique for disk UMEs with controlled geometry. The UMEs are made up of a wire or filament of noble metal (i.e. gold, platinum or silver) or carbon sealed inside a glass capillary with a highly reproducible geometry. The ratio of the insulating sheath to the electroactive core of the UMEs was between 2.5 and 3.6 with 90 % yield. The UMEs can be used as voltammetric, potentiometric and amperometric micrometer size sensors for analytical measurements, and can fit most SECM platforms. Moreover, the fabricated disk UMEs can be used as a geometrically controlled platform to develop other UME geometries. For example, the UMEs have been used as a backbone for the production of hemispherical and disk Hg UMEs as well as Ag/AgCl micro-reference electrodes. The technique described in Chapter 2 to produce the Hg hemispherical UME is used again in Chapter 4 with nano-size electrodes for the preparation of the manganese amperometric sensor. [11]

Future directions for this chapter include developing an automated process to manufacture microelectrodes. The manufacturing process presented in Chapter 2 was developed for small batch production by a single skilled operator. Optimization of the fabrication process will increase the throughput and reduce skilled labor time, leading to a decrease in production costs. Currently, the insertion of the electroactive wire into the capillary is a bottle neck in the process. Therefore, it will be useful to develop a robot to automate this step. Developing this prototype will draw on our knowledge base with precision motor controls, as used in SECM, and computational scripting to automatically sequence the key steps.

Chapter 3 presented the optimization of the SECM technique for the intended LIB application. The resolution in SECM is primarily dependent on the radius of the UME and the tip to substrate distance. Therefore, Chapter 3 explores the use of the laser-pulling technique to produce electrodes. In comparison with the technique presented in Chapter 2, which gave an electroactive core in the micrometer range, the technique presented in Chapter 3 produced active electrode radii of 3 to 190 nm with a typical ratio of insulator to conductor ranging from 5 to 25. Moreover, the electrodes produced using this technique possess long flexible tapers that provide excellent SF sensitivity. Chapter 3 also aimed at optimizing constant distance imaging of SECM by optimizing the shear force sensitivity. This systematic study of shear force lead to the determination of parameters to achieve the highest sensitivity, and therefore optimized the control over distance to the substrate. It also provided us with a technique to select the shear force sensitive frequencies. In this chapter we also demonstrated the ability of the nanoelectrodes to perform simultaneous topographic and electrochemical measurements.[12]

Future directions for this chapter include investigating the relation between the shear force and the nature of the substrate surface (soft substrates may be deformed under the influence of the force interactions), the viscosity, and temperature. LIB electrolyte solutions usually being made up of an organic media such, as propylene carbonate, ethylene carbonate dimethyl, diethyl, and ethyl-methyl carbonates, and a lithium salt such as $LiPF_{6,}$ a systematic study of shear force in high viscosity media would be required to clearly demonstrate the functionality of these probes for SF-SECM measurements in the field of LIBs.

Chapter 4. In this chapter, we have reported a successful method for the fabrication of Hg/Pt hemispherical nanoelectrodes using electrodeposition from a mercuric inorganic solution onto laser-pulled Pt/quartz discs. This methodology draws from techniques introduced in the previous chapters, namely probe fabrication in Chapter 3 and the deposition technique in Chapter 2. The nanoelectrodes were used as manganese amperometric probes to investigate Mn^{2+} dissolution from spinel $LiMn_2O_4$ positive electrode material. The quantitative detection of Mn^{2+} cations is of particular interest, as the dissolution of Mn^{2+} has been identified as the leading factor for the decrease in capacity associated with the cycling of this positive electrode material. The fully characterized probes were calibrated with respect to the concentration of Mn^{2+} ions using anodic stripping voltammetry. The technique has been used to evaluate the impact of using chelating agent for alleviating the detrimental consequences of Mn^{2+} dissolution in LIBs. The efficiency of the chelating agent was demonstrated by measuring the decrease in the signal for Mn^{2+} upon consecutive additions of Mn^{2+} chelating polymeric azacrown ethers.[13]

Chapter 4 described the efficiency polymeric azacrown ethers dissolved in aqueous media under static conditions. Chapter 4 is a preamble to Chapter 5 in which, due to the sensitivity of the samples, the experiment was relocated into a glovebox. **Chapter 5** draws from the knowledge acquired in Chapters 2, 3 and 4, and describes the fabrication and characterization of mercury-capped platinum nanoelectrodes in an oxygen and water-free environment. The nanoelectrodes were employed as manganese amperometric detectors to gain information on the capture efficiency of A15C5 in propylene carbonate in $LiPF_6$. The Hg/Pt nanoelectrodes were fabricated by electrodeposition from a mercuric ion solution onto Pt/quartz laser-pulled disk nanoelectrodes. Chapter 5 displaying results acquired in battery electrolyte to provide a more realistic understanding of the efficiency of the chelating macrocycles for the intended application.

A future direction for Chapter 4 and 5 includes using the developed probe as an SECM tip for the localized detection of manganese and other transition metal cations. As mentioned in Chapter 4, the crown ethers are intended to be coated on a commercial polyolefin battery separator (as represented in the schematic Figure 5.1). Mapping these separator using the technique describe in Chapter 2 could potentially indicate regions where there is failure in the coating. In order to have a more realistic battery environment, another avenue would be to design a device that allows consistent flow of solution in order to carry out experiments *in-situ*. The flow cell (Figure 6.1.) would allow the manipulation of the manganese solutions with a known pressure to pass through the uncoated and coated separators while mimicking a real battery environment. This experiment would allow one to determine the rate of capture of the chelating agents and establish the efficiency of the crown ethers to sequester Mn^{2+} cations.

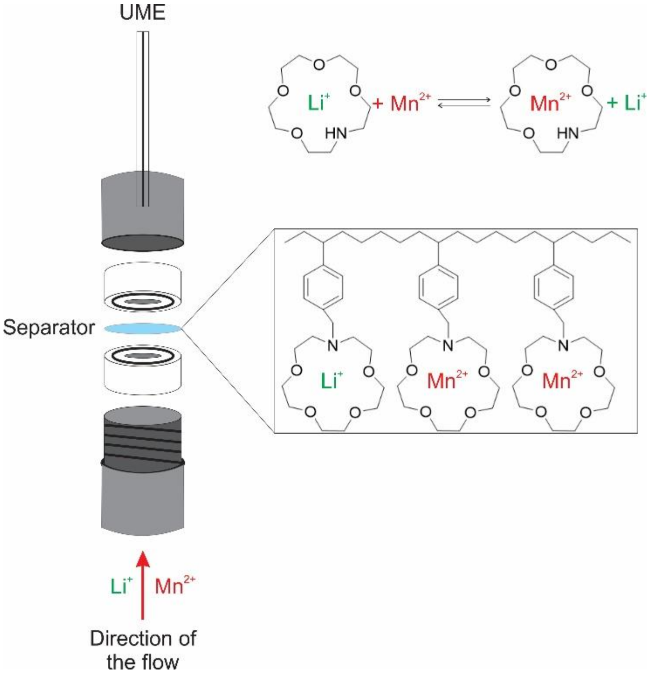

Figure 6.1. A schematic diagram of the tailored flow cell displaying the manganese dissolution problem and the polymeric A15C5 coated on the separator, chelating Mn^{2+}.

The previous chapters focused on the trapping efficiency of the crowns for Mn^{2+}. However, as mentioned in Chapters 4 and 5, contrary to what is commonly accepted, recent XANES studies have demonstrated that the average oxidation state of manganese cations present in electrolyte solutions from $Li_xMn_2O_4$-graphite cells cycled at high temperatures could be closer to +3 than +2. In fact, these experiments yield in an average ranging from +3.2 to +3.4 for the electrolyte-filled separator, from +3.1 to +3.2 for the $Li_xMn_2O_4$ positive electrode, and from +2.8 to +3.0 for the graphite negative electrode. Therefore, it is very likely that Mn^{2+}, Mn^{3+} and Mn^{4+} coexist in the electrolyte solution after charge-discharge cycling, suggesting that +2 is small fraction of the Mn present outside of the positive electrode.[14] Then again, these experiments were performed *ex-situ* post cell disassembly, strengthening the need for the development of analytical tools for *in-situ* measurements on LIBS to exclude any data corruption by sample handling artifacts.

Although the use of A15C5 has been proven sucessfull to substrantially improve the capacity retention of $Li_xMn_2O_4$-graphite cells and decrease in Mn deposition on the graphite negative electrode, research on more effective chelating agents is relevant even more in the light of the conflicting oxidation state data obtained by XANES. Several factors impact the trapping efficiency including, as previously mentioned, the size of the cavity of the crown ether, the presence or absence of dipole moment and also characteristic of their polymeric forms such as type of backbone, morphology, length of linker, amount of cross-linking, etc.[15] Further studies would be required in order to select the most effective chelating agent and optimize the trapping efficiency, and to reduce the negative consequences associated with Mn dissolution.

In summary, the work presented in this thesis joins the continuing effort to build new analytical tools that, used in conjunction with other classical materials characterization methods used in the field, will help to obtain a comprehensive understanding of LIBs fundamental mechanisms, processes and degradation.

[1] J.-R. Lee, J.-H. Won, J.H. Kim, K.J. Kim, S.-Y. Lee, Journal of Power Sources, 216 (2012) 42-47.

[2] J.-H. Park, W. Park, J.H. Kim, D. Ryoo, H.S. Kim, Y.U. Jeong, D.-W. Kim, S.-Y. Lee, Journal of Power Sources, 196 (2011) 7035-7038.

[3] J. HunáKim, Journal of Materials Chemistry, 21 (2011) 8192-8198.

[4] M. Ulaganathan, S.S. Pethaiah, S. Rajendran, Materials Chemistry and Physics, 129 (2011) 471-476.

[5] M. Ulaganathan, R. Nithya, S. Rajendran, S. Raghu, Solid State Ionics, 218 (2012) 7-12.

[6] B. Reeja-Jayan, N. Chen, J. Lau, J.A. Kattirtzi, P. Moni, A. Liu, I.G. Miller, R. Kayser, A.P. Willard, B. Dunn, Macromolecules, 48 (2015) 5222-5229.

[7] J.-C. Daigle, A. Vijh, P. Hovington, C. Gagnon, J. Hamel-Pâquet, S. Verreault, N. Turcotte, D. Clément, A. Guerfi, K. Zaghib, Journal of Power Sources, 279 (2015) 372-383.

[8] X. Su, T. Zhang, X. Liang, H. Gao, B.W. Sheldon, Acta Materialia, 98 (2015) 175-181.

[9] P. Raghavan, X. Zhao, J. Manuel, C. Shin, M.-Y. Heo, J.-H. Ahn, H.-S. Ryu, H.-J. Ahn, J.-P. Noh, G.-B. Cho, Materials Research Bulletin, 45 (2010) 362-366.

[10] C. Jangu, A.M. Savage, Z. Zhang, A.R. Schultz, L.A. Madsen, F.L. Beyer, T.E. Long, Macromolecules, 48 (2015) 4520-4528.

[11] L. Danis, D. Polcari, A. Kwan, S.M. Gateman, J. Mauzeroll, Analytical Chemistry, 87 (2015) 2565-2569.

[12] L. Danis, M.E. Snowden, U.M. Tefashe, C.N. Heinemann, J. Mauzeroll, Electrochimica Acta, 136 (2014) 121-129.

[13] L. Danis, S.M. Gateman, M.E. Snowden, I. Halalay , J. Howe, J. Mauzeroll, Electrochimica Acta,162 (2015) 169-175.

[14] Z. Li, A.D. Pauric, G.R. Goward, T.J. Fuller, J.M. Ziegelbauer, M.P. Balogh, I.C. Halalay, Journal of Power Sources, (2014).

[15] A.D. Pauric, S. Jin, T.J. Fuller, M.P. Balogh, I.C. Halalay, G.R. Goward, Journal of Physical Chemistry C, 120 (2016) 3677-3683.

APPENDIX A: FABRICATION OF CARBON, GOLD, PLATINUM, SILVER AND MERCURY ULTRAMICROELECTRODES WITH CONTROLLED GEOMETRY

A.1. *COMMERCIALLY AVAILABLE DISK ULTRAMICROELECTRODES*

Table A.1. *Commercially Available Disk Ultramicroelectrodes*

Commercial Source	Electroactive Surface Diameter (µm)	RG
Princeton Applied Research	10, 15, 25 (Pt)	10
BASi	10 (Au, Pt)	350
	11 (C)	318
	25 (Ag, Au, Pt)	140
CH Instruments, Inc.	12.5, 25 (Au) 10, 25 (Pt)	10
Metrohm Autolab B.V	10 (Au, Pt)	400
	20 (Pt)	200
	25 (Ag, Au, Pt)	160
Thomas Recording GmbH	10 (Pt)	10
Uniscan Instruments	10, 15, 25 (Pt)	10
Heka Electronik	4.7 (C) 10, 25 (Pt)	2–3

APPENDIX B: DEVELOPMENT OF NANO-DISC ELECTRODES FOR APPLICATION AS SHEAR FORCE SENSITIVE ELECTROCHEMICAL PROBES

B.1. DETERMINATION OF THE SHEAR FORCE DISTANCE-DEPENDENT FREQUENCIES AND PHASE BEHAVIOR

Supplementary information Figure B.1 has been constructed from the same set of data as for the main text figure 3.4. Figure B.1.A is the difference spectrum from the first approach to determine tip-to-substrate separation sensitive frequencies (Figure 3.4.A) and was constructed by subtracting the amplitude of the spectrum recorded on surface from the spectrum recorded above surface. Figure B.1.B was obtained by the subtraction of the amplitude of the spectrum recorded in liquid and from the spectrum recorded in air to exemplify the second method to determine tip-to-substrate separation SF sensitive frequencies (Figure 3.4.B). The arrows marked with an X in the Figure B.1.B designate frequencies at which a false positive occurs, an absent amplifying SF sensitive frequency is also emphasized. Figure B.1.C is an enlargement of the SF sensitive peak at 417.5 kHz (Figure 3.4.C) and its corresponding phase behavior from third approach to determine tip-to-substrate separation SF sensitive frequencies. We can observe a very steep decrease in the phase from 180 to 0 degree making this frequency a SF sensitive frequency. The maximum of the amplitude corresponds to the middle of this phase shift (*i.e.* 90 degrees). Figure B.1.D show an enlargement of the frequency spectrum and phase reported in (Figure 3.4.C) for the non-sensitive peak at 360 kHz the amplitude peak does not occur at 50 % of the severe change in phase.

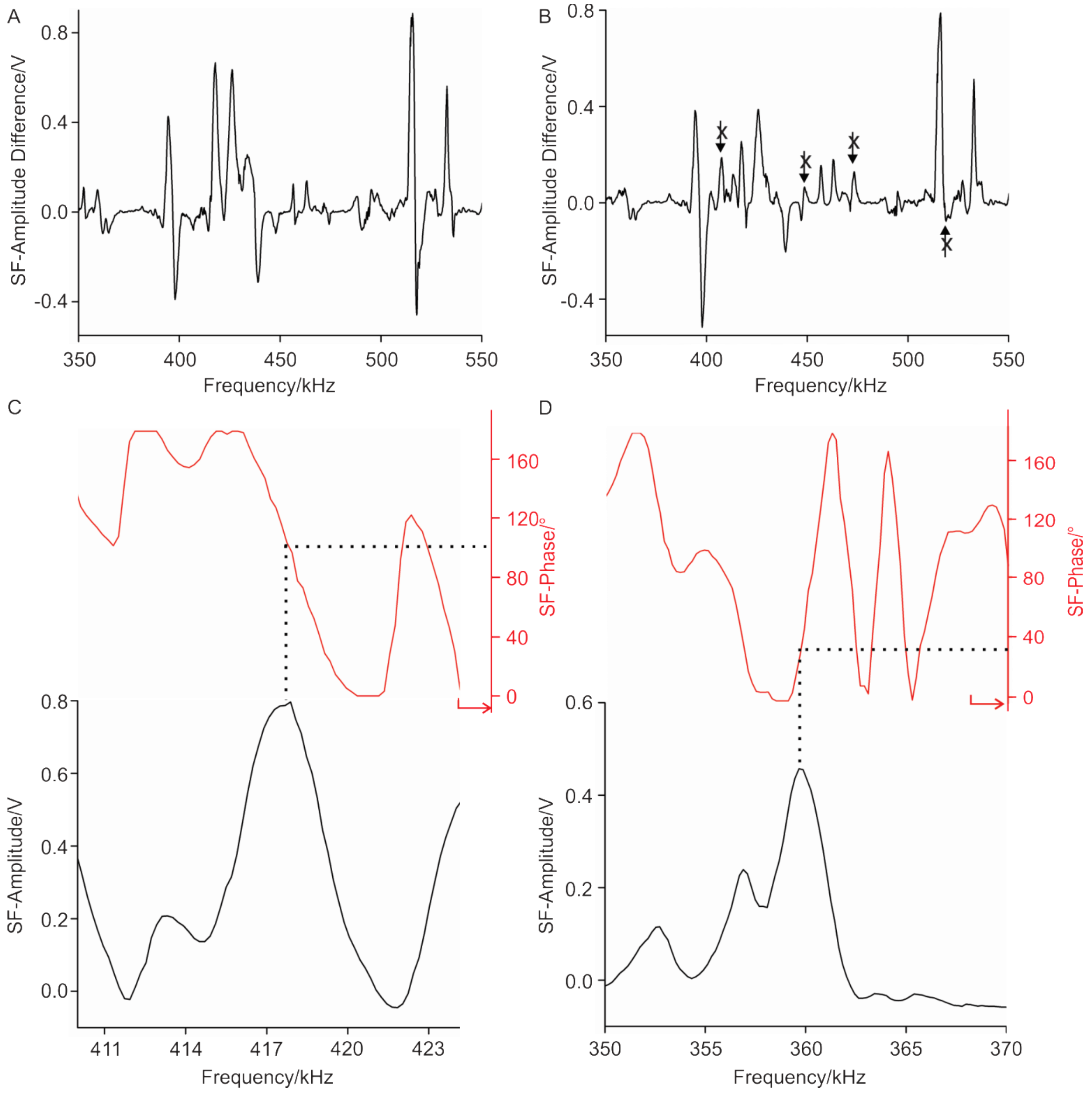

Figure B.1. (A) Difference spectrum constructed by subtracting the amplitude of the spectrum recorded on surface from the spectrum recorded above the surface. (B) Difference spectrum obtained by the subtraction the amplitude of the spectrum recorded in liquid above surface from the spectrum recorded above surface of the liquid. The arrows marked with an X represent false positives (no corresponding peak in B.1.A). (C) Enlargement of the shear force sensitive peak at 417.5 kHz and its corresponding phase behavior. (D) Enlargement of the non-shear force sensitive peak at 360 kHz. To allow direct comparison all data within this figure and figure 3 of the main text employ the same nanoelectrode and piezo assembly.

B.2. REPRODUCIBILITY OVER MULTIPLE SHEAR FORCE APPROACH CURVES

Multiple SF approach curves were performed to show that the nanoelectrode tip was not damaged during the approach curve measurements. The stability of the electrochemical response upon 15 consecutive SF approaches was demonstrated by cyclic voltammetry (Figure B.2.A). A nanoelectrode with r_T = 46 nm, was employed in a solution containing 1 mmol dm^{-3} FcMeOH in 0.1 mol dm^{-3} KCl, with an approach speed of 0.1 µm s^{-1}. The I_{ss} and wave shape from the CV recorded with a tip-to-substrate separation greater than 10 µm remained unchanged. Furthermore, the SF amplitude and approach curve remained unchanged clearly demonstrating stability and reproducibility of the electrochemical response and SF response upon successive approaches. For more information please refer to the characteristic measurement of a shear force calibration curve (pull back curve) section of the main text.

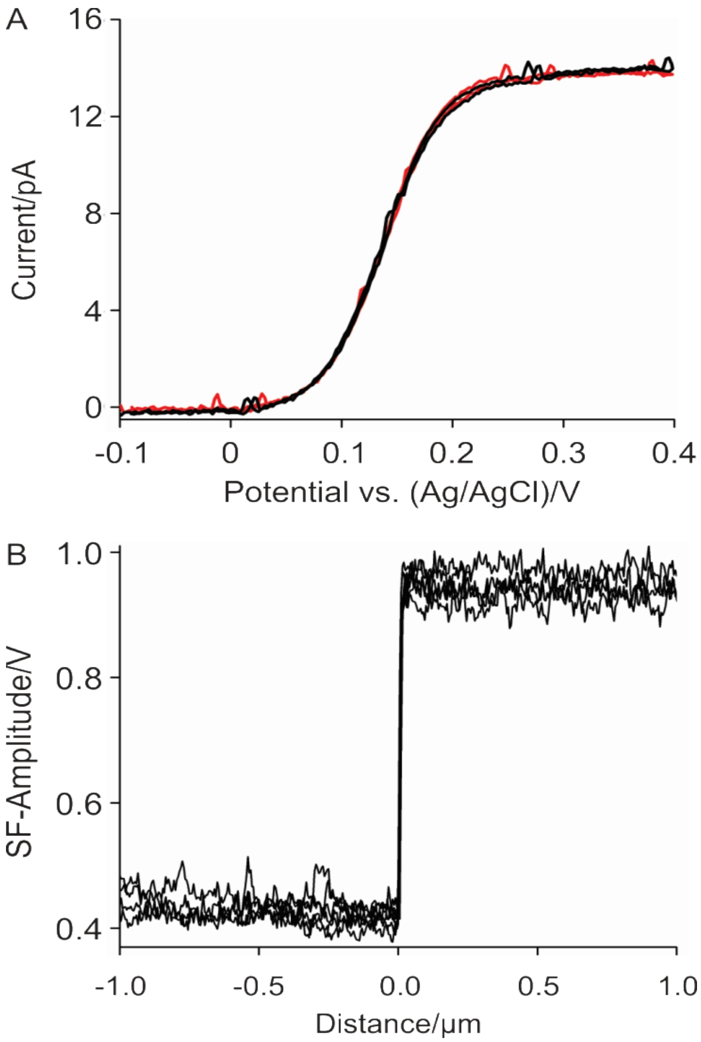

Figure B.2. Reproducibility data for multiple approach curves preformed with the same probe geometry demonstrating that the nanoelectrode tip was not damaged during the approach curve measurements. (A) The CV (red) solid line was recorded before and (black) solid line was recorded after 15 successive approaches curves the I_{ss} and wave shape do not change demonstrating stability of the electrochemical response upon successive approaches. (B) SF approach curve data recorded during the 15 SF approach curves. The SF signal does not change with successive approach curve measurements.

B.3. EXPERIMENTAL FACTORS THAT INFLUENCE SHEAR FORCE SENSITIVITY: APPLIED OSCILLATION AMPLITUDE

Figure B.3. emphasizes the influence of the applied oscillation amplitude on the SF response. (Figure B.3.A, B and C) shows the increase in SF amplitude magnitude with respect to the increase of stimulation amplitude from 40.0 mV to 100 mV, from 100 mV to 1.00 V and from 1.00 V to 10.0 V respectively for the same experimental data reported in figure 3.5.D of the main text . (Figure B.3.D) shows the influence of the varying the applied oscillation amplitude on SF calibration curve. The difference in receiver amplitude was linearly dependent with the applied dither amplitude (Figure B.3.E and F). Figure B.3.E displays SF total response with respect to the stimulation amplitude for stimulation amplitude from 100 mV to 9.00 V and figure B.3.F shows the SF total response and Q_F with respect to the stimulation amplitude, for stimulation amplitudes from 100 mV to 900 mV. For more information please refer to the experimental factors that influence shear force sensitivity section of the main text.

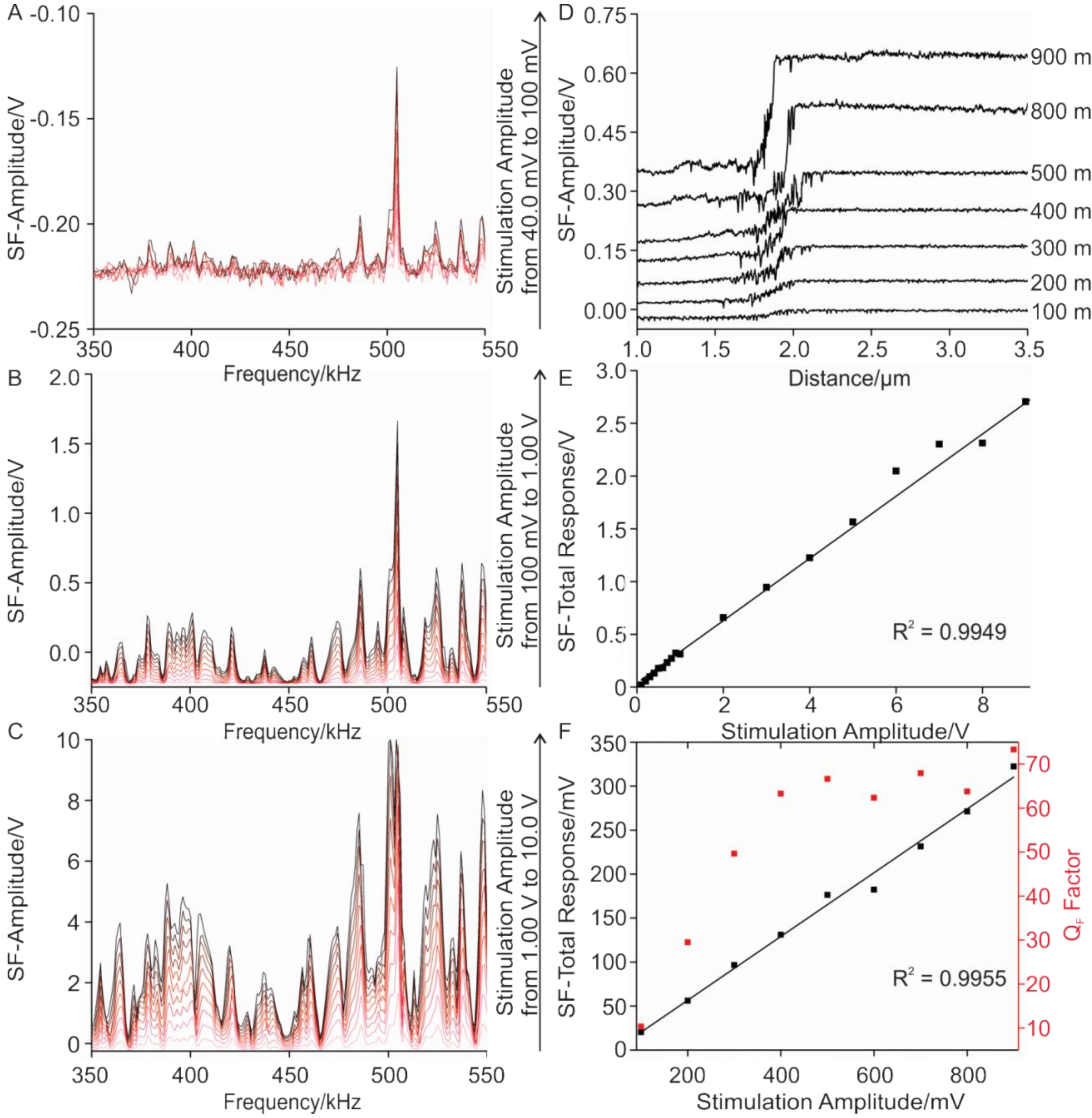

Figure B.3. (A) The increase in SF amplitude magnitude with respect to the increase of stimulation amplitude 40.0 mV to 100 mV. (B) The increase in SF amplitude magnitude with respect to the increase of stimulation amplitude 100 mV to 1.00 V. (C) The increase in SF amplitude magnitude with respect to the increase of stimulation amplitude 1.00 V to 10.0 V. (D) SF calibration curve with respect to the increase of stimulation amplitude. (E) SF total response (V) with respect to the stimulation amplitude for stimulation amplitudes from 100 mV to 9.00 V. (F) SF total response and Q_F with respect to the stimulation amplitude for stimulation amplitude from 100 mV to 900 mV.

B.4. EXPERIMENTAL FACTORS THAT INFLUENCE SHEAR FORCE SENSITIVITY: ANGLE BETWEEN THE STIMULATION AND RECEIVER PIEZOELECTRIC PLATES

Figure B.4. is complementary to figure 3.6. of the main text and shows the influence of varying the angle between the stimulation and receiver on the sensitive frequencies. (Figure B.4.) has been performed with the same probe and experimental conditions reported for figure 3.6. In (Figure B.4.) the (black) solid line is a spectra recorded above surface and the (red) solid line is a spectra recorded on surface with the angle between the dither and receiver of 0 ° or parallel (Figure B.4.A.), 90 ° (Figure B.4.B.), 45 ° (Figure B.4.C.), 180 ° (Figure B.4.D.), 70 ° (Figure B.4.E.), and 20 ° (Figure B.4.F.). For more information please refer to the experimental factors that influence shear force sensitivity section of the main text.

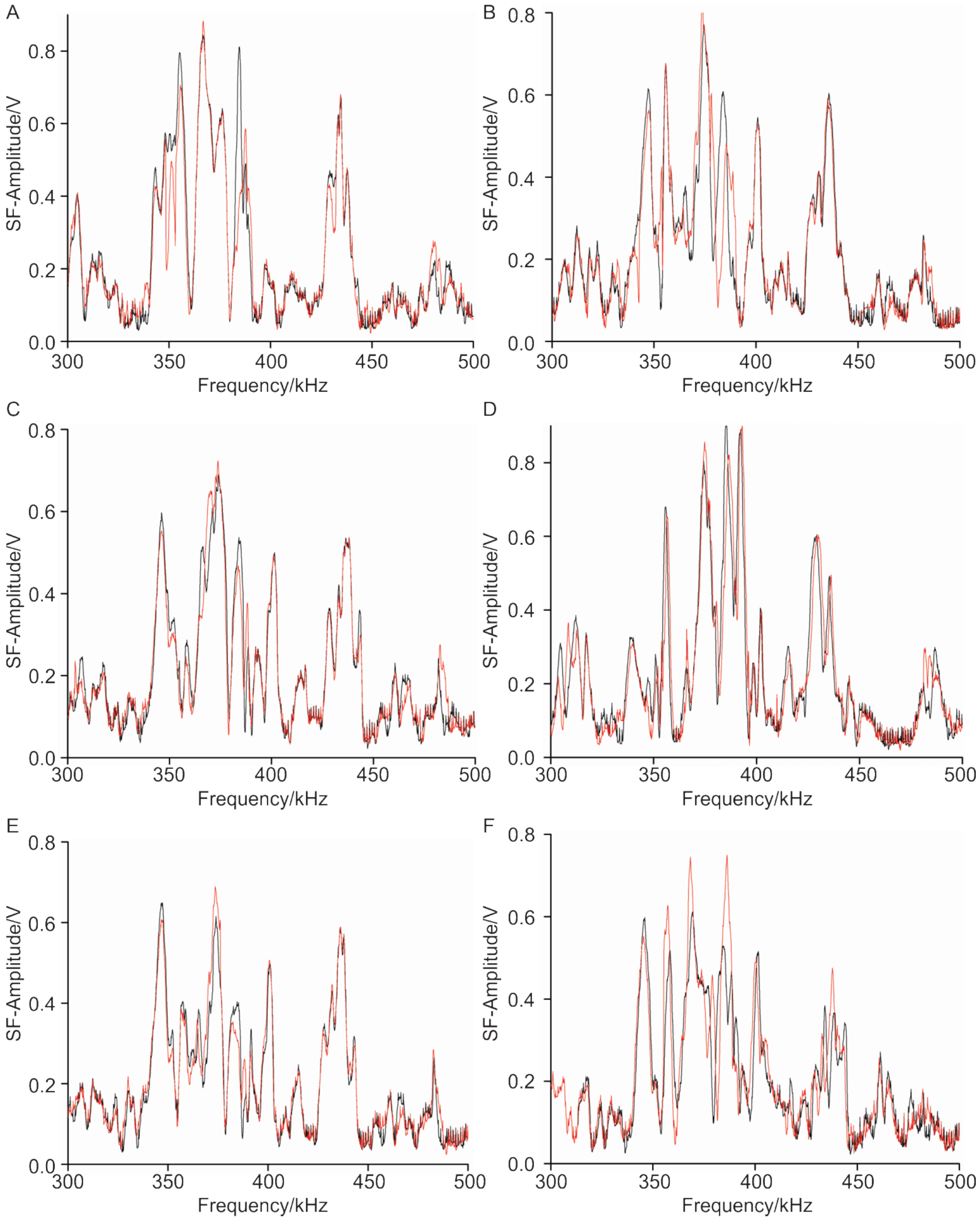

Figure B.4. The influence of varying the angle between the stimulation and receiver on the sensitive frequencies the (black) solid line is a spectra recorded above surface and the (red) solid line is a spectra recorded on surface with an angle between the dither and receiver (A) 0 ° or parallel (B) 90 ° (C) 45 ° (D) 180 ° (E) 70 ° (F) 20 °.

APPENDIX C: MANGANESE DETECTION

C.1. REPRODUCIBILITY OF THE MANGANESE DETECTION

Successive CVs were performed in a 10 μM manganese(II) nitrate aqueous solution at a scan rate of 250 mV s^{-1}, to determine the stability and reproducibility of the electrochemical response for manganese detection. Ten consecutives scans were performed and displayed the reproducibility shown in Figure C.1. Mercury capped nanoelectrodes were stable for up to 7 days when stored in 0.1 M KNO_3 solution.

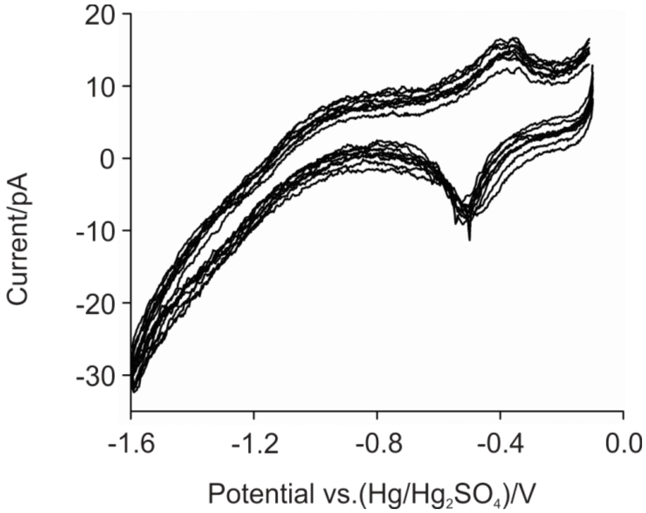

Figure C.1. 10 consecutive CVs in a 10 μM manganese(II) nitrate aqueous solution at a scan rate of 250 mV s^{-1}.

Figure C.2.A. displays the effect of deposition potential on the plating/stripping response. The curves were generated by successively stepping the potential was from -200 to -300, -400, -500 and -600 mV for a duration of 250 ms, then back to -200 mV for 550 ms during each plating/stripping cycle. Figure C.2.B. shows the integrated deposition peak area (marked “1”) *vs.* the deposition potential in its linear response region (with $R^2 = 0.9907$). Figure C.2.C shows the similar data for the stripping peak, with $R^2 = 0.9994$. The ratio of the charge in peak 2 to that in peak 1 was 1.08, indicating reversible and reproducible manganese stripping.

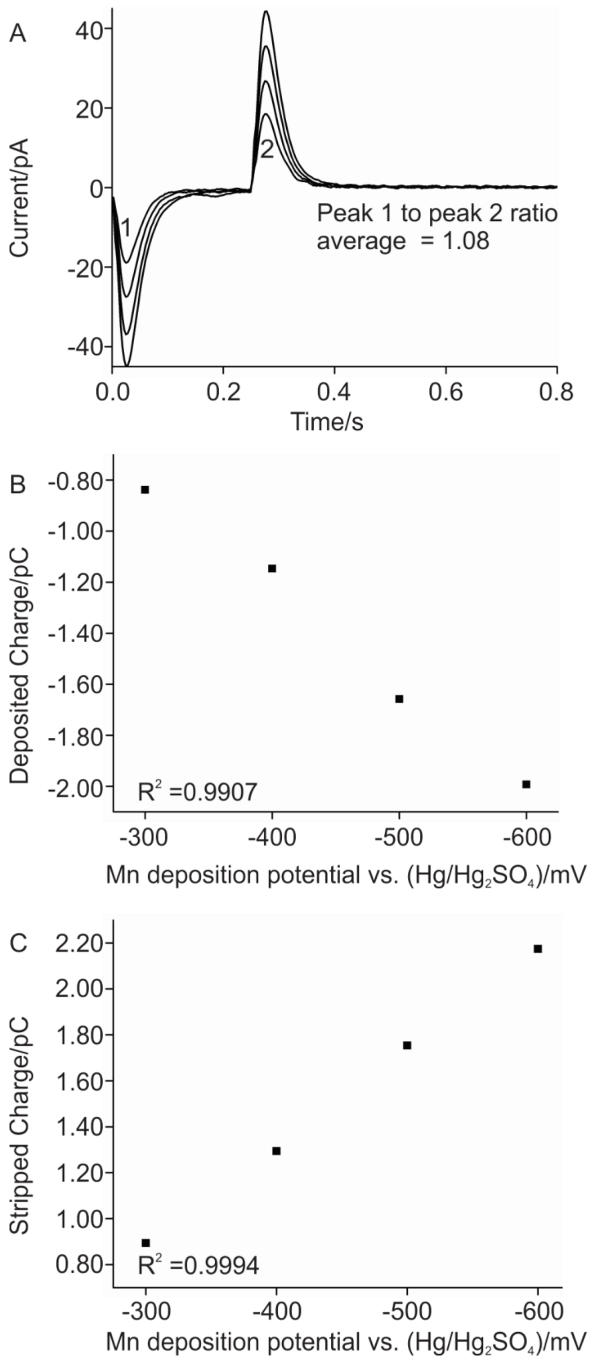

Figure C.2. (A) Effect of deposition potential on the stripping response. The potential was stepped from -200 to -300, -400, -500 and -600 mV for a duration of 250 ms. (B) Integrated deposition peak (peak 1 in panel (A)) *vs.* the manganese deposition potential in its linear response region ($R^2 = 0.9907$). (C) Integrated stripping peak (peak 2 in panel (A)) *vs.* applied potential in its linear response region ($R^2 = 0.999$). The average deposition to stripping charge to charge ratio is 1.08 ± (0.04).

Figure C.3 displays the optimization procedure for the manganese deposition time. Figure C.3.A and Figure C.3.B show the raw data for the stripping results in 1 µM and 5 µM manganese (II) nitrate aqueous solutions, respectively. The charge underneath peak 2 for different deposition times in 1µM manganese (II) nitrate solution is shown in Figure C.3.C. and for 5µM manganese (II) nitrate solution in Figure C.3.D. Figure C.3.A. and Figure C.3.C. indicate that there is an increase in the measured charge with the increased deposition time for deposition times shorter than 250 ms for the 1 µM solution and shorter than 95 ms for the 5 µM solution; however, the increase in charge with deposition is non-linear. In contrast, there is no increase in the stripping charge for deposition times greater than 250 ms (1 µM solution) and 100 ms (5 µM solution), here due to the saturation of mercury spherical cap with manganese. As can be seen, saturation of the mercury cap is reached faster at higher Mn concentrations. Based on these data we selected a deposition time of 100 ms for subsequent deposition/stripping measurements.

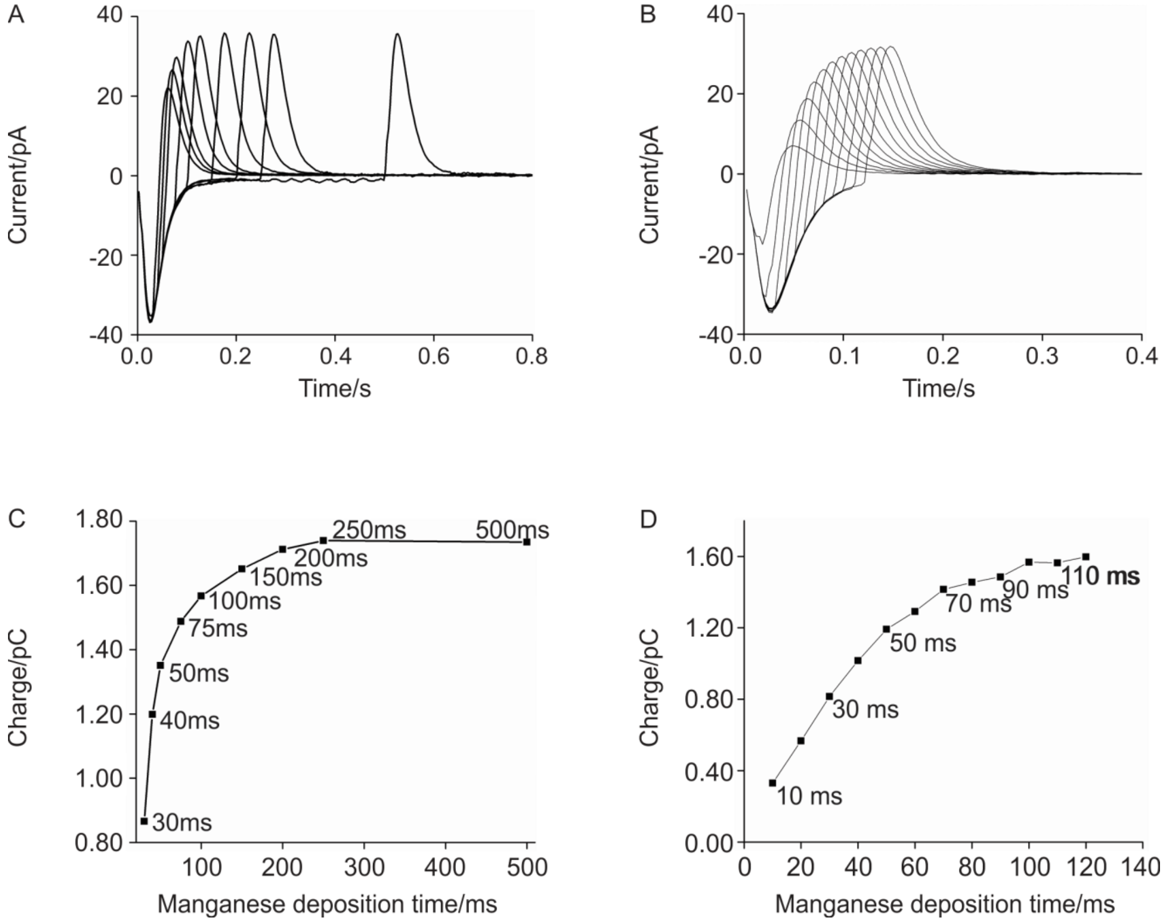

Figure C.3. (A) Current *vs.* time data for a 1.0 μM manganese(II) nitrate aqueous solution for deposition times ranging from 30 to 500 ms. (B) Current *vs.* time data for a 5.0 μM manganese (II) nitrate aqueous solution with deposition times ranging from 10 to 110 ms. (C) Deposited charge *vs.* manganese deposition time for the 1.0 μM manganese (II) nitrate solution as in (A). (D) Deposited charge *vs.* manganese deposition time for the 5.0 μM manganese (II) nitrate solution as in (D).

Figure C.4. shows the potential *vs.* time response for the stripping measurements with potential steps from -200 mV to -600 mV held for 30 ms, 40 ms, 50 ms, 75 ms, 100 ms, 150 ms, 200 ms, 250 ms and 500 ms durations, then stepped to -200 mV. The potential-time plot shows a reproducible potential rise for the first step, and a symmetric decrease with time for the second step (i.e. with identical slopes at a given potential during both the current decrease and increase). From these plots we determined the potential scan rate to be *ca*. 5.5 V s^{-1}.

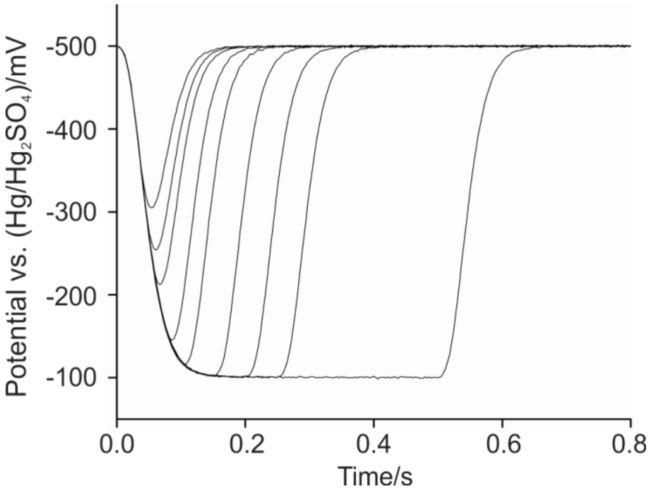

Figure C.4. Potential *vs.* time plots of the stripping experiment for a potential step from -200 mV to -600 mV. Potential holds with durations of 30, 40, 50, 75, 100, 150, 200, 250 and 500 ms are shown, followed by a potential step to -200 mV.